International Journal of

Mathematics

and Physics

The International Journal of Mathematics and Physics is a peer-reviewed international journal covering all branches of mathematics and physics. The Journal welcomes papers on modern problems of mathematics and physics, in particular, Applied Mathematics, Algebra, Mathematical Analysis, Differential Equations, Mechanics, Informatics, Mathematical Modeling, Applied Physics, Radio Physics, Thermophysics, Nuclear Physics, Nanotechnology, and etc.

EDITORIAL

The most significant scientific achievements are attained through joint efforts of different sciences, mathematics and physics are among them. Therefore, publication of the Journal, which shows results of current investigations in the field of mathematics and physics, will allow wider exhibition of scientific problems, tasks and discoveries. One of the basic goals of the Journal is to promote extensive exchange of information between scientists from all over the world. We propose publishing service for original papers and materials of Mathematical and Physical Conferences (by selection) held in different countries and in the Republic of Kazakhstan. Creation of the special International Journal of Mathematics and Physics is of great importance because a vast amount of scientists is willing to publish their articles and it will help to widen the geography of future dissemination. We will also be glad to publish papers of scientists from all the continents.

The Journal will publish experimental and theoretical investigations on Mathematics, Physical Technology and Physics. Among the subject emphasized are modern problems of Applied Mathematics, Algebra, Mathematical Analysis, Differential Equations, Mechanics, Informatics, Mathematical Modeling, Astronomy, Space Research, Theoretical Physics, Plasma Physics, Chemical Physics, Radio Physics, Thermophysics, Nuclear Physics, Nanotechnology, etc.

The Journal is issued on the base of al-Farabi Kazakh National University. Leading scientists from different countries of the world agreed to join the Editorial Board of the Journal. The Journal is published twice a year by al-Farabi Kazakh National University. We hope to receive papers from many laboratories, which are interested in applications of the scientific principles of mathematics and physics and are carrying out researches on such subjects as production of new materials or technological problems.

Chouhaïd Souissi[1,*] , Asma Omar[1,2], Mohamed Hbaib[1]

[1]University of Sfax, Rte El Matar, Sfax, Tunisia
[2]Sabratha University, Sabratha, Libya
*e-mail: chouhaid.souissi@fss.usf.tn

Influence of additive white noise forcing on solutions of mixed nls equations

Abstract. In this paper, the influence of an additive white noise forcing term on the numerical solution for a class of deterministic nonlinear one-dimensional Schrödinger equations with mixed concave convex was studied, sub-super nonlinearities, that is, the stationary states and the blowing-up solutions. Such a perturbation occurs when the size of the noise, described by the real-value parameter ε is positive. The size of the noise is controlled by the parameter $\varepsilon > 0$. We also proved that as ε approaches zero, the solution of the perturbed problem converges to the unique trajectory of the deterministic equation, which is the solitary wave. The stochastic model appears to be more realistic, and one can observe, for small values of ε, a similar evolution phenomena about the solution as that given by the deterministic case. However, an explosion of the solution and a blow-up phenomena can be noted as ε becomes bigger.
Key words: Nonlinear Schrödinger equation, Mixed nonlinearity, Blow-up phenomena, Finite difference scheme, White noise, Solvability.

1. Introduction

In this work, we are interested in the study of the one-dimensional stochastic nonlinear Schrödinger (NLS) equation with both subcritical and supercritical power nonlinearities in the presence of an additive noise. The resulting equation is a random perturbation of the dynamical system of the following form

$$\begin{cases} iu_t + u_{xx} + g_\alpha(u) + f_\varepsilon(u) = 0, t \geq 0, L_2 \geq x \geq L_1, \\ \\ u(0,x) = u_0(x), L_1 \leq x \leq L_2, \\ \\ u_x(t,L_1) = u_x(t,L_2) = 0, t \geq 0, \end{cases} \quad (1)$$

where $u = u(t,x)$ is a complex-valued function defined for $t \geq 0$ and $x \in \mathbb{R}$, α is a positive real parameter, L_1 and L_2 are reals such that $L_1 < L_2$, u_t is the derivative of u with respect to the time t and u_{xx} is its second derivative wiht respect to the position x. The function g_α is defined by

$$g_\alpha(u) = |u|^{p-1}u + \alpha|u|^{q-1}u.$$

The term $f_\varepsilon(u)$ includes the stochastic contribution. In our case, we are concerned with an additive noise. This means that it will be considered to be real-valued, Gaussian, white in time and either white or correlated in space. As an immediate consequence, the noise does not depend on the solution. The size of the noise is controlled by the parameter $\varepsilon > 0$.

The deterministic equation occurs as a basic model in many areas of physics, hydrodynamics, plasma physics, nonlinear optics, molecular biology. It describes the propagation of waves in media with both nonlinear and dispersive responses. It took the interest of some researchers like Ben Mabrouk et al. [3], Bratsos [4], Keraani [12] and Sulem and Sulem [15]. It is an idealized model and does not take into account many aspects such as in-homogeneities, high

order terms, thermal fluctuations and external forces, which may be modeled as random excitations like it was the case in the works of Cheung and Mosincat [5], Falkovich et al. [9], Farlano et al. [10] and Oh et al. [13].

Here, we particularly treat the influence of a noise acting as a potential on the behavior of the deterministic solution. Such effects on solitary waves have already been studied for the NLS equation and for also for the Korteweg-de-Vries equation (see, for example, Printems [14]). This kind of noise has been considered by Garnier in [11], where the paths were smooth functions and the nonlinearity was subcritical. In the case of a white noise, this type of model has been introduced in the context of crystals by Bang et al. [1]. It is expected that such a noise has a strong influence on the solutions which blow-up. It may delay or even prevent the formation of a singularity. It has been shown in [6], by Debussche and Di Menza, via numerical simulations, that this is the case for a very irregular noise: for a space-time white noise. However, in the supercritical case and for a noise which is correlated in space but non degenerate, it has been observed, on the contrary, that any solution seems to blow-up in a finite time. We recall that in the deterministic case, only a restricted class of solutions blow-up.

The case of an additive noise has been considered in [7] by De Bouard and Debussche. It has been proved that for any initial data, blow-up occurs in the sense that, for arbitrary $t > 0$, the probability that the solution blows up before the time t is strictly positive. Thus, the noise strongly influences this blow-up phenomenon. In the present paper, the result is in perfect agreement with the numerical simulations. It represents, between others, a generalization of the results established by Ben Mabrouk et al. in [3] and by Debussche and Di Menza in [6].

The paper is organized as follows: In Section 2, we give a precise mathematical definition of the additive white noise and transform the continuous problem (1) to a discrete algebraic one. Then, we study the solvability of the difference scheme. The next section is devoted to the convergence of this scheme. Some numerical implementations are given in section 5 to validate the scheme. The paper is ended by a recapitulative conclusion.

2. Discretization of the stochastic Schrödinger equation

In this section, we start by giving a mathematical definition for an additive white noise. We follow the approach taken by Debussche and DiMenza in [6]. We consider a probability space $(\Omega, \mathcal{F}, P)$, endowed with a filtration $\left(\mathcal{F}(t)\right)_{t \geq 0}$. We also consider a cylindrical Wiener process $\left(W(t)\right)_{t \geq 0}$ on $L^2(\mathbb{R})$, which is adapted to this filtration. Then, we have

$$W(t, x, w) = \sum_{i=0}^{\infty} \beta_i(t, w) e_i(x),$$

where $(e_i)_{i \in \mathbb{N}}$ is an orthogonal basis of $L^2(\mathbb{R})$ and $(\beta_i)_{i \in \mathbb{N}}$ a sequence of independent real valued Brownian motions on $\mathbb{R}^+$, associated to $\left(\mathcal{F}(t)\right)_{t \geq 0}$. The white noise is the time derivative of W. This makes that the stochastic forcing term will be written in the following form

$$f_\varepsilon(u) = \varepsilon \dot{\chi} = \frac{\partial W}{\partial t}.$$

More details and generalizations of these notations can be found in [] and the references therein. Taking in account these notations, we then rewrite the first equation in (1) as follows

$$iu_t + u_{xx} + g_\alpha(u) = \varepsilon \dot{\chi}, t \geq 0, L_2 \geq x \geq L_1$$

Now, we are in position to establish the finite difference scheme corresponding to the problem (1). We consider a time step $l = \Delta t$ and denote the time discretization by

$$t^k = kl = \text{k}(t^{k+1} - t^k).$$

We fix an integer M and consider, a space step

$$h = \Delta x = \frac{L_2 - L_1}{M + 1}.$$

Then, we subdivide the interval $[L_1, L_2]$ into subintervals $[x_m, x_{m+1}]$, where

$$x_m = L_0 + mh, m \in \{0, \ldots, M+1\}$$

This allows to consider the space grid

$$\Omega_h = \{x_m = L_0 + mh, m \in \{0, \ldots, M+1\}\},$$

We, also, consider the space W_h of functions defined on Ω_h, and vanishing at zero. It is endowed with the inner product, defined for any given vectors

$$U = (U_0, U_1, \ldots, U_{M+1})^t \text{ and } V = (V_0, V_1, \ldots, V_{M+1})^t$$

of $\mathbb{R}^{M+2}$, by

$$< U, V >_h = h \sum_{m=0}^{M+1} U_m V_m,$$

and the associated L^2-norm

$$||U||_{h,2} = (U, U)_h^{1/2} = \left(h \sum_{M=0}^{M+1} U_m \right)^{1/2}.$$

We denote by u_m^k the approximation of $u(t^k, x_m)$ and by U_m^k the numerical solution. We introduce the following notations

$$\delta_m^k U = \frac{U_m^{k+1} - U_m^{k-1}}{2l},$$

$$\Delta_m^k U = \frac{U_{m+1}^k - 2U_m^k + U_{m-1}^k}{h^2},$$

$$(U_t)_m^k = \lambda \delta_{m-1}^k U + (1 - 2\lambda)\delta_m^k U + \lambda \delta_{m+1}^k U,$$

$$(U_x)_m^k = \frac{U_{m+1}^k - U_{m-1}^k}{2h},$$

$$(U_{xx})_m^k = \mu \Delta_m^{k+1} U + (1 - 2\mu)\Delta_m^k U + \mu \Delta_m^{k-1} U.$$

We then discretize the problem (1) as follows

$$i(U_t)_m^k + (U_{xx})_m^k + g_\alpha(U_m^k) =$$

$$= \varepsilon f_m^{k+\frac{1}{2}}, \text{ m = 0, ..., M+1.}$$

Since we treat an additive noise, we have

$$f_m^{k+\frac{1}{2}} = \frac{1}{l\sqrt{h}}\left(\beta_m(t_{k+1}) - \beta_m(t_k)\right),$$

$$\text{m = 1, ..., M,}$$

$$f_0^{k+\frac{1}{2}} = \frac{\sqrt{2}}{l\sqrt{h}}\left(\beta_0(t_{k+1}) - \beta_0(t_k)\right),$$

$$f_{M+1}^{k+\frac{1}{2}} = \frac{\sqrt{2}}{l\sqrt{h}}\left(\beta_M(t_{k+1}) - \beta_M(t_k)\right).$$

Moreover, as the random variables

$$\frac{1}{l}\left(\beta_m(t_{k+1}) - \beta_m(t_k)\right), \text{k} \geq 0, \text{ m = 0, ..., M+1}$$

are independent with normal law $\mathcal{N}$ (0,1), we can choose the

$$\left(\chi_m^{k+\frac{1}{2}}\right), \text{k} \geq 0, \text{ m = 0, ..., M+1}$$

to be a sequence of independent random variables with normal law $\mathcal{N}$ (0, 1). The numerical problem is considered under the initial data

$$\begin{cases} U_m^0 = u(0, x_m) = u_0(x_m), 0 \leq m \leq M+1, \\ U_m^1 = U_m^0 + il\left(u_0''(x_m) + g_\alpha(u_0(x_m))\right), 0 \leq m \leq M+1, \\ U_1^k = U_0^k \text{ and } U_M^k = U_{M+1}^k, k \geq 0. \end{cases} \quad (2)$$

We consider the approximation

$$h_\alpha(U_m^k) = (v_1 U_m^k + (1 - v_1)U_m^{k-1})\tilde{h}_\alpha, \\ v_1 \in [0,1],$$

where

$$\tilde{h}_\alpha = \max_{0 \leq m \leq M+1}\{|U_m^0|^{p-1} + \alpha |U_m^0|^{q-1}\}.$$

Next, we denote by σ the report

$$\sigma = \frac{l}{h^2}$$

and take the following notations,

$$a_1 = 2\mu\sigma + i\lambda,$$

$$a_2 = -4\mu\sigma + (1 - 2\lambda)i,$$

$$b_1 = -2\sigma(1 - 2\mu),$$

$$b_2 = 4\sigma(1 - 2\mu) - 2v_1 l \, \tilde{h}_\alpha,$$

$$c_1 = -2\mu\sigma + i\lambda,$$

$$c_2 = 4\mu\sigma + i(1 - 2\lambda) - 2(1 - v_1) l \, \tilde{h}_\alpha,$$

This leads, for $1 \le m \le M$, to

$$a_1(U_{m-1}^{k+1} + U_{m+1}^{k+1}) + a_2 U_m^{k+1} =$$

$$= b_1 (U_{m-1}^k + U_{m+1}^k) + b_2 U_m^k +$$

$$+c_1(U_{m-1}^{k-1} + U_{m+1}^{k-1}) + c_2 U_m^{k-1} + \varepsilon f_m^{k+\frac{1}{2}} \quad (3)$$

The boundary conditions are expressed as follows

$$(a_1 + a_2) U_0^{k+1} + a_1 U_1^{k+1} =$$

$$= (b_1 + b_2) U_0^k + b_1 U_1^k +$$

$$+(c_1 + c_2) U_0^{k-1} + c_1 U_1^{k-1} + \varepsilon f_0^{k+\frac{1}{2}} \quad (4)$$

and

$$a_1 U_{M-1}^{k+1} + (a_1 + a_2) U_M^{k+1} =$$

$$= b_1 U_{M-1}^{k+1} + (b_1 + b_2) U_M^{k+1} +$$

$$+c_1 U_{M-1}^{k+1} + (c_1 + c_2) U_M^{k+1} + \varepsilon f_{M+1}^{k+\frac{1}{2}}. \quad (5)$$

3. Solvability of the difference scheme

To prove the solvability of the dufference scheme, we need to write the problem (3)-(5) in its matrix form, i.e.,

$$AU^{k+1} = BU^k + CU^{k-1} + F, \quad (6)$$

where A is the $(N + 2)^2$-matrix defined as follows

$$A = \begin{pmatrix} a_1 + a_2 & a_1 & 0 & \cdots & \cdots & 0 \\ a_1 & a_2 & a_1 & & \ddots & \vdots \\ 0 & \ddots & \ddots & & \ddots & \vdots \\ \vdots & \ddots & \ddots & \ddots & \ddots & 0 \\ \vdots & \ddots & & a_1 & a_2 & a_1 \\ 0 & \cdots & \cdots & 0 & a_1 & a_1 + a_2 \end{pmatrix}.$$

B is also an $(M + 2)^2$-matrix. It is obtained by replacing a_1 and a_2 respectively by b_1 and b_2 in the matrix A. Similarly, C is the $(M + 2)^2$-matrix obtained by replacing respectively a_1 and a_2 by b_1 and b_2 in A. Finally, the matrix F represents the white noise vector. It is expressed as follows

$$F = \begin{pmatrix} f_0^{k+\frac{1}{2}} \\ \vdots \\ f_m^{k+\frac{1}{2}} \\ \vdots \\ f_{N+1}^{k+\frac{1}{2}} \end{pmatrix}.$$

The solvability of the difference scheme (3)-(5) is related to the determinant of the matrix A. This is based on a result developed by El-Mikkawy and Karawia in [8] and treating the invertibility of a general tri-diagonal matrix. We recall the basic result in what follows,

Lemma 1 *[8] Consider the following real matrix A,*

$$E = \begin{pmatrix} d_1 & y_1 & 0 & \cdots & \cdots & 0 \\ z_2 & d_2 & y_2 & \ddots & \ddots & \vdots \\ 0 & \ddots & \ddots & & \ddots & \vdots \\ & & \vdots & \ddots & \ddots & \ddots & 0 \\ \vdots & \ddots & \ddots & z_{M-1} & d_{M-1} & y_{M-1} \\ 0 & \cdots & \cdots & 0 & z_M & d_M \end{pmatrix}$$

and define the real vector

$$\tau = (\tau_0, \tau_1, \dots, \tau_n)^t$$

as follows

$$\tau_j = \begin{cases} 1 & if \ j = 0, \\ d_1 & if \ j = 1, \\ d_j \tau_{j-1} - z_j y_{j-1} \tau_{j-2} & if \ j = 2, 3, \dots, n. \end{cases} \quad (7)$$

Then, there holds

$$Det(E) = \tau_n.$$

Now, we are in position to state the main result of this section.

Theorem 1 *The difference scheme (3)-(5) is uniquely solvable.*

Proof Denote by $Det_{M+2}(A)$ the determinant of the matrix A. Then, we have the following recursive equation

$$Det_{M+2}(A) -$$
$$-(a_1 + a_2)\,Det_{M+1}(A) + a_1^2\,Det_N(A) = 0.$$

Thanks to Lemma 1, we deduce $Det_{M+2}(A)$ in three cases.

<u>First case:</u> $\mu = 0$ and $\lambda = \frac{1}{3}$: Standard computations yield,

$$Det_{M+2}(A) = (M+3)\left(\frac{i}{3}\right)^{M+2} \neq 0.$$

<u>Second case:</u> $\mu = 0$ and $\lambda \neq \frac{1}{3}$. We denote by

$$\delta = \sqrt{1 - 2\lambda - 3\lambda^2},$$

$$X_1 = \frac{i}{2}(1 - \lambda + \delta),$$

$$X_2 = \frac{i}{2}(1 - \lambda - \delta),$$

$$C_1 = -\frac{1-\lambda}{\delta} + \frac{iX_2(-2 + 5\lambda - 2\lambda^2)}{\delta\lambda^2},$$

$$C_2 = -\frac{1-\lambda}{\delta} + \frac{iX_1(-2 + 5\lambda - 2\lambda^2)}{\delta\lambda^2}.$$

Then, we have

$$Det_{M+2}(A) = C_1 X_1^{M+2} + C_2 X_2^{M+2} \neq 0 \quad (8)$$

<u>Third case:</u> $\mu \neq 0$. We consider the following complex values,

$$\delta = \sqrt{(a_1 + a_2)^2 - 4a_1^2},$$

$$X_1 = \frac{1}{2}(a_1 + a_2 + \delta),$$

$$X_2 = \frac{1}{2}(a_1 + a_2 - \delta).$$

Computations similar to the second case lead also to the equation (8).

It follows that the system (3)-(5) is uniquely solvable.

4. Convergence of the difference scheme

The main result of this section can be stated as follows,

Theorem 2 *Suppose that $l = o(h^2)$, is small enough. Then, the difference scheme (3)-(5) is convergent.*

Proof We set,

$$X = e^{i\psi} \text{ and } Z = e^{i\theta},$$

$$\theta \in \mathbb{R}, \psi \in \mathbb{C},$$

and write

$$U_m^k = e^{ik\psi}e^{im\theta} = X^k Z^m,$$

$$k \geq 0, m = 0, \ldots, M+1.$$

By replacing, first in (3), we obtain, for $k \geq 1$ and $1 \leq m \leq M$,

$$A_m(Z)X^{k+1} + B_m(Z)X^k +$$
$$+C_m(Z)X^{k-1} - \varepsilon f_m^{k+\frac{1}{2}} = 0, \quad (8)$$

where

$$\begin{cases} A_m(Z) = \left[(2\mu\sigma + i\lambda)(1 + Z^2) + \left(-4\mu\sigma + i(1 - 2\lambda)\right)Z\right]Z^{m-1}, \\[2mm] B_m(Z) = \left[-2\sigma(1 - 2\mu)(1 + Z^2) + \left(4\sigma(1 - 2\mu) - 2vl\tilde{h}_\alpha\right)Z\right]Z^{m-1}, \\[2mm] C_m(Z) = \left[(-2\mu\sigma + i\lambda)(1 + Z^2) + \left(4\mu\sigma + i(1 - 2\lambda) - 2(1 - v_1)l\tilde{h}_\alpha\right)Z\right]Z^{m-1}. \end{cases}$$

Then, replacing in (4), we obtain for k ≥ 1 and $m = 0$,

$$A_0(Z)X^{k+1} + B_0(Z)X^k + C_0(Z)X^{k-1} - \varepsilon f_0^{k+\frac{1}{2}} = 0,$$

with

$$\begin{cases} A_0(Z) = -2\mu\sigma + i(1-\lambda) + (2\mu\sigma + i\lambda)\,Z, \\[2mm] B_0(Z) = 2\sigma(1-2\mu) - 2v_1 l\tilde{h}_\alpha - 2\sigma(1-2\mu)\,Z, \\[2mm] C_0(Z) = 2\mu\sigma + i(1-\lambda) - 2(1-v_1)l\tilde{h}_\alpha + (-2\mu\sigma + i\lambda)\,Z. \end{cases}$$

Finally, replacing in (5), we obtain for k ≥ 1 and $m = M + 1$,

$$A_{M+1}(Z)X^{k+1} + B_{M+1}(Z)X^k + C_{M+1}(Z)X^{k-1} - \varepsilon f_{M+1}^{k+\frac{1}{2}} = 0,$$

where

$$\begin{cases} A_{M+1}(Z) = \left[2\mu\sigma + i\lambda + \left(-2\mu\sigma + i(1-\lambda)\right)Z\right]Z^M, \\[2mm] B_{M+1}(Z) = \left[-2\sigma(1-2\mu) + \left(2\sigma(1-2\mu) - 2v_1 l\tilde{h}_\alpha\right)Z\right]Z^M, \\[2mm] C_{M+1}(Z) = \left[-2\mu\sigma + i\lambda + \left(2\mu\sigma + i(1-\lambda) - 2(1-v_1)l\tilde{h}_\alpha\right)Z\right]Z^M. \end{cases}$$

When ψ is real, it is obvious from the equation (9) that U_m^k remains bounded. Otherwise, a sufficient condition for the convergence of the scheme is that

$$\left|e^{i\psi}\right| \leq 1. \tag{9}$$

In that case, one has

$$\left|e^{i\psi}\right| = |X| \leq \min\left\{\frac{|B_m|}{|A_m|}, 0 \leq m \leq M+1\right\}. \tag{10}$$

Taking $m = 0$, supposing that $l = o(h^2)$ and following the calculations given by Ben Mabrouk et al. in [2], the equations (9) and (10) lead to,

$$|B_0|^2 - |A_0|^2 \leq 0,$$

and the result follows.

5. Numerical implementations

We want to investigate the noise effects on stationary solutions in a concrete situation. We recall that the deterministic solutions take the following form

$$u(x,t) = \sqrt{\frac{2a}{q_s}}\exp\left(i\left(\frac{1}{2}cx - \theta t + \varphi\right) + sech\left(\sqrt{a}(x - ct) + \phi\right)\right).$$

where a, q_s, $\theta = \frac{c^2}{4} - a$, φ and ϕ are appropriate constants. It is a soliton-type disturbance which travals with speed c and with a governed amplitude.

In the treated example, the time and space partial derivative parameters are fixed to the particular case where

$$\lambda = \frac{1}{5} \ and \ \mu = \frac{1}{3}.$$

For the numerical scheme (3)-(5), the computations are done in the space domain $[L_1, L_2]$, with $L_1 = -80$ and $L_2 = 100$. The space step was $h = 1$. The considered time interval was $[0, 10]$, with a time step $l = 0.01$. The soliton parameters were fixed as follows,

$$a = 0.01, q_s = 1 \text{ and } c = 0.1$$

and the phase parameters

$$\phi = \varphi = 0.$$

For the nonlinearity, we took the values

$$q = 0.73,\ p = 1.5 \text{ and } v_1 = 0.5.$$

It was numerically proved that the asymptotic limit of the solution $u(\varepsilon)$ of the problem (1), as ε goes to 0, is in fact, the stationary wave $u(0)$, which corresponds to the the deterministic case (see Figure 1), and physically interpreted by the absence of noise.

For small amplitudes of the noise, corresponding to small values of the parameter ε, we can see that the solitary wave is not strongly perturbed and that the noise does not prevent its propagation. This is clearly expressed in Figure 2, where the values $\varepsilon = 0.1$, $\varepsilon = 0.05$ *and* $\varepsilon = 0.04$ were respectively drown in the parts (a), (b) and (c) of this figure.

However, as the noise level becomes higher, the wave is progressively destroyed. This is the subject of Figure 3, in which the values $\varepsilon = 0.1$, $\varepsilon = 0.15$

*and* $\varepsilon = 0.25$ correspond respectively to the parts (a), (b) and (c).
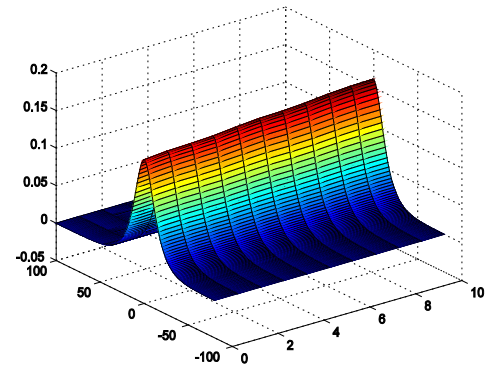
Figure 1 – Plots in the (t,x)-plane of the stationary wave corresponding to the deterministic case: $\varepsilon = 0$

Now, taking the amplitude ε of the noise greater than 0.3, it is clearly seen that the wave explodes under the influence of the additive noise. This blow-up phenomenon appears in Figure 4, (a) and (b), respectively for $\varepsilon = 0.45$ and $\varepsilon = 0.35$.

(a)

(b)

(c)
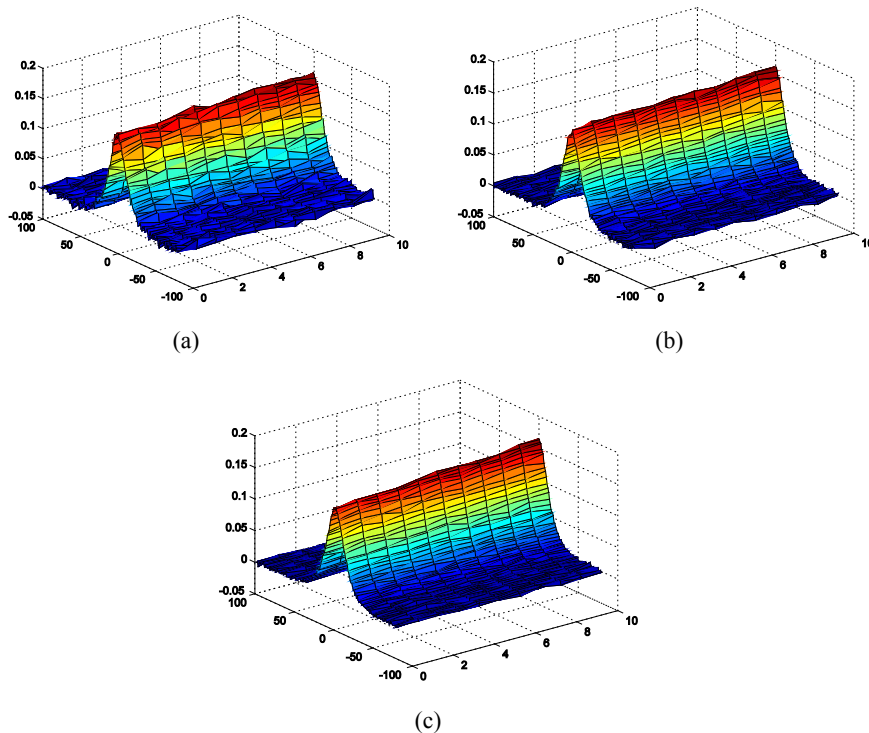
Figure 2 – Plots in the (t,x)-plane of |u| for one trajectory
for small values of the amlitude of the noise.
(a) ε = 0.1, (b) ε = 0.05, (c) ε = 0.04

(c)

(d)

(c)
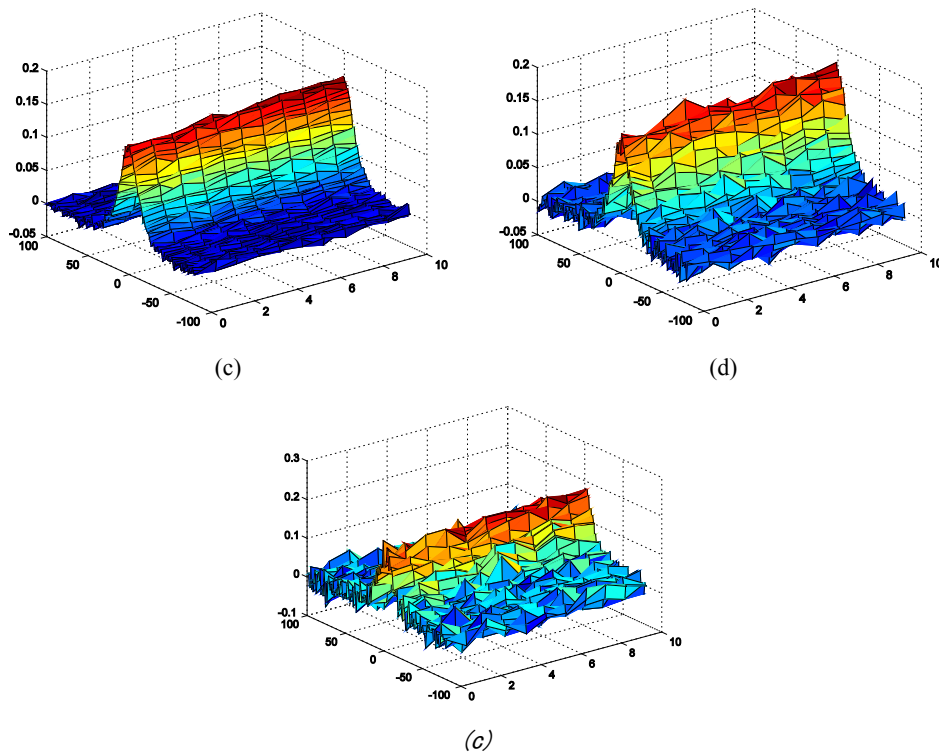
Figure 3 – Progressive destruction of the stationary wave,
plotted in the (t,x)-plane, as the amplitude of the noise becomes bigger.
(a) ε = 0.1, (b) ε = 0.15, (c) ε = 0.25

(a)

(b)
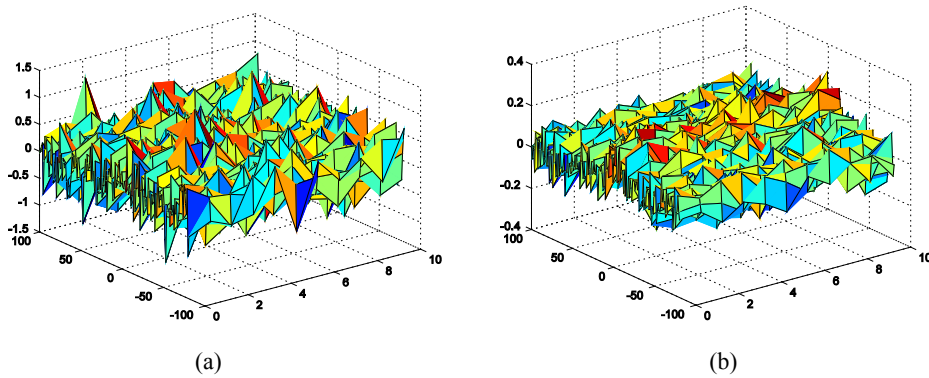
Figure 4 – Explosion of the wave, plotted in the (t,x)-plane,
under the effect of big values of the noise.
(a) ε = 0.45, (b) ε = 0.35.

6. Conclusion

It is noted that the stochastic nonlinear equation (1) can be considered as an additive white noise random perturbation of the deterministic equation, defined for $\varepsilon = 0$. Such a perturbation occurs when the size of the noise, described by the real-value parameter ε, is positive. We proved that as ε approaches zero, the solution of the perturbed problem converges to the unique trajectory of the deterministic equation, which is the solitary wave. The stochastic model appears to be more realistic, and one can observe, for small values of ε, a similar evolution phenomena about the solution as that given by the deterministic case. However, an explosion of the solution and a blow-up phenomena can be noted as ε becomes bigger.

References

1. Bang, O., Christiansen, P. L., If, F., Rasmussen, K. O., Gaididei, Y. B. "Temperature effects in a nonlinear model of monoplayer Scheibe aggregates." Phys. Rev. E 49 (1994), 4627-4636.

2. Ben Mabrouk, A., Ben Mohamed M. L., Omrani, K. "Finite difference approximate solutions for a mixed sub-supelinear equation." Appl. Math. Comput. 187 (2007), no. 2, 1007-1016.

3. Ben Mabrouk, A., Bezia, A., Souissi, C. "Numerical approximations and asymptotic limits of some nonlinear problems." Bull. Transilv. Univ. Bras. III Math. Comput. Sci. Vol. 3 (65), No. 2 (2023), 53–70.

4. Bratsos, A. G. "A linearized finite-difference scheme for the numerical solution of the nonlinear cubic Schrödinger equation." Korean J. Comput. Appl. Math. 8 (2001), no. 3, 459-467.

5. Cheung, K., Mosincat, R. "Stochastic nonlinear Schrödinger equations on tori." *Stoch PDE: Anal Comp* **7**, (2019), 169–208.

6. Debussche A., Di Menza L., "Numerical simulation of focusing stochastic nonliner Schrödinger equations." Physica D, 162 (2002), 131-154.

7. De Bouard, A., Debussche, A. "On the effect of a noise on the solutions of the focusing supercritical nonlinear Schrödinger equation." Probab. Theory Related Fields, 123 (2002), 76-96. M R1906438.

8. El-Mikkawy, M., Karawia, A. "Inversion of general tridiagonal matrices." Appl. Math. Letters, 19 (2006), 712-720.

9. Falkovich, G. E., Kolokolov, I., Lebedev, V., Turitsyn S. K. "Statistics of soliton-bearing systems with additive noise." Phys. Rev. E, 63 (2001), 025601(R).

10. Farlano J., Oh T., Wang Y., "Stovhastic cuic nonlinear Schrödinger equation with almost space-time white noise." J. Aust. Math. Soc. 109 (2020), no. 1, 44-67. MR-4120796.

11. Garnier, J. "Asymptotic transmission of solitons through random media. SIAM J. Appl. Math. 58 (1998), 1969-1995. MR1644311.

12. Keraani, S., "On the blow-up phenomena of the critical Schrödinger equation." J. Funct. Anal. 235 (2006), 171-192.

13. T. Oh, O. Pocovnicu and Y. Wang. "On the stochastic nonlinear Schrödinger equations with non-smooth additive noise." Kyoto J. Math. 60 (2020), no. 4, 1227-1243.

14. Printems, J. "Aspects théoriques et numériques de l'équation de Korteweg-de Vries stochastique." Ph.D. de University Paris-Sud Orsay (2009).

15. Sulem, C and Sulem, P. L., "The Nonlinear Schrödinger Equation, Self-Focusing and Wave Collapse." Springer, New York (1999), MR1696311.

Information about authors:

Chouhaïd Souissi – (corresponding author), PhD Mathematics, professor of University of Sfax, (Rte El Matar, Sfax,Tunisia, e-mail: chouhaid.souissi@fss.usf.tn);

Asma Omar – researcher of University of Sfax, (Rte El Matar, Sfax, Tunisia);

Mohamed Hbaib – researcher of Sabratha University, (Sabratha, Libya).

Aslıhan Sezgin* [ID], Aleyna Ilgin [ID]

Amasya University, Turkey, Amasya
e-mail: aslihan.sezgin@amasya.edu.tr

Soft ıntersectıon almost subsemıgroups of semıgroups

Abstract. Semigroups are the building blocks of algebra as they have application in automata, coding theory, formal languages, and theoretical computer science. They are also used in the solutions of graph theory and optimization theory. For the advanced study of algebraic structures and their applications, ideals are essential. The generalization of ideals in algebraic structures is necessary for further research on algebraic structures. The main purpose of this paper is to present the notion of soft intersection almost subsemigroup of a semigroup, which is a generalization of soft intersection subsemigroup and investigate its basic properties in detail. In this context, we also obtain many striking relationships between almost subsemigroups and soft intersection almost subsemigroups concerning minimality, primeness, semiprimeness and strongly primeness.

Key words: semigroups, soft intersection, algebraic structures, almost subsemigroup of a semigroup, graph theory, optimization theory, minimality, simplicity, semi-simplicity and strong simplicity.

I. Introductıon

Semigroups are the building blocks of algebra as they have applications in automata, coding theory, formal languages, and theoretical computer science. They are also used in the solutions of graph theory and optimization theory. For the advanced study of algebraic structures and their applications, ideals are essential. The generalization of ideals in algebraic structures is necessary for further research on algebraic structures. Many mathematicians introduced different expansions of the notion of ideals in algebraic structures, demonstrating important results and characterizing algebraic structures. Grosek and Satko [1] introduced the concept of almost left, right, and two-sided ideals of semigroups for the first time in 1980. Later in 1981, Bogdanovic [2] proposed the notion of almost bi-ideals in semigroups as an extension of bi-ideals. Using the concepts of semigroup quasi-ideals and almost ideals, Wattanatripop et al. (2018) introduced the idea of almost quasi-ideals. Kaopusek et al. [4], using the concepts of almost ideals and interior ideals of semigroups, proposed the concepts of almost interior ideals and weakly almost interior ideals of semigroups and investigated their characteristics in 2020. The concepts of almost bi-interior ideals of semigroups, almost subsemigroups of semigroups, and almost bi-quasi-interior ideals of semigroups were first presented by Iampan et al. [5] in 2021,

Chinram and Nakkhasen [6] in 2022, and Gaketem [7] in 2022, respectively. In addition, various forms of fuzzification of almost ideals were studied in [3, 5-9].

To model uncertainty, Molodtsov [10] introduced the concept of soft set in 1999. Soft set is defined as a function from the parameter set E to the power set of U. Since then, scholars from a wide range of domains have become interested in soft sets. Soft set operations, which form the foundation of the theory, are examined in [11–26]. The definition of soft set and soft set operations were modified by Çağman and Enginoğlu [27]. Furthermore, Çağman et al. [28] developed the idea of soft intersection groups, which served as inspiration for a variety of soft algebraic structures. The idea of soft intersection substructures of semigroups originated with the use of soft sets in semigroups. Soft intersection subsemigroups, left (right/two-sided ideals), (generalized) bi-ideals, interior ideals, and quasi-ideals of semigroups were developed and explored by Sezer et al. [29, 30]. Sezgin and Orbay [31] characterized semisimple semigroups, duo semigroups, right(left) zero semigroups, right(left) simple semigroups, semilattice of left(right) simple semigroups, semilattice of left(right) groups, and semilattice of groups. Lately, Rao [32–35] presented a variety of new semigroup ideals, including weak-interior ideals, bi-quasi-interior ideals, bi-interior ideals, and quasi-interior ideals. Baupradist [36] established the essential semigroup ideals. A variety of algebraic

structures, including soft sets, were examined in [37–46] which can be handled as regards graph applications together with network analysis with the inspiration of divisibility of determinants as in [47].

In this study, we introduced the notion of soft intersection almost subsemigroup of a semigroup, which is a generalization of the nonnull soft intersection subsemigroup of a semigroup. We obtain that the union of soft intersection almost subsemigroups is again soft intersection almost subsemigroup; but their intersection is not. Moreover, we revealed the relation between almost subsemigrops and soft intersection almost subsemigroups of a semigroup with respect to minimality, primeness, semiprimeness, and strongly primeness.

II. PRELIMINARIES

In this paper, we give some fundamental notions related to semigroups and soft sets.

Definition 2.1. Let U be the universal set, E be the parameter set, $P(U)$ be the power set of U, and $K \subseteq E$. A soft set f_K over U is a set-valued function such that $f_K: E \rightarrow P(U)$ such that for all $x \notin K$, $f_K(x) = \emptyset$. A soft set over U can be represented by the set of ordered pairs

$$f_K = \{(x, f_K(x)): x \in E, f_K(x) \in P(U)\}$$

[10,27]. Throughout this paper, the set of all the soft sets over U is designated by $S_E(U)$.

Definition 2.2. Let $f_A \in S_E(U)$. If $f_A(x) = \emptyset$ for all $x \in E$, then f_A is called a null soft set and denoted by $\emptyset_E$. If $f_A(x) = U$ for all $x \in E$, then f_A is called an absolute soft set and denoted by U_E [27].

Definition 2.3. Let $f_A, f_B \in S_E(U)$. If for all $x \in E$, $f_A(x) \subseteq f_B(x)$, then f_A is a soft subset of f_B and denoted by $f_A \tilde{\subseteq} f_B$. If $f_A(x) = f_B(x)$ for all $x \in E$, then f_A is called soft equal to f_B and denoted by $f_A = f_B$ [27].

Definition 2.4. Let $f_A, f_B \in S_E(U)$. The union of f_A and f_B is the soft set $f_A \tilde{\cup} f_B$, where $(f_A \tilde{\cup} f_B)(x) = f_A(x) \cup f_B(x)$ for all $x \in E$. The intersection of f_A and f_B is the soft set $f_A \tilde{\cap} f_B$, where $(f_A \tilde{\cap} f_B)(x) = f_A(x) \cap f_B(x)$ for all $x \in E$ [27].

Definition 2.5. For a soft set f_A, the support of f_A is defined by

$$supp(f_A) = \{x \in A: f_A(x) \neq \emptyset\} \text{ [15]}.$$

It is obvious that a soft set with an empty support is a null soft set, otherwise the soft set is nonnull.

Note 2.6. If $f_A \tilde{\subseteq} f_B$, then $supp(f_A) \subseteq supp(f_B)$.

A semigroup S is a nonempty set with an associative binary operation. Throughout this paper, S denotes a semigroup and all the soft sets are the elements of $S_S(U)$. A nonempty subset K of S is called a subsemigroup of S if $KK \subseteq K$; and is called an almost subsemigroup (briefly almost SS) if $K^2 \cap K \neq \emptyset$ ($KK \cap K \neq \emptyset$). Let A and B be any almost subsemigoups of S such that $B \subseteq A$. If $A = B$, then A is a minimal almost subsemigroup (briefly minimal almost SS) of S. An almost subsemigroup P of S is called a prime almost subsemigroup (briefly prime almost SS) if for any almost subsemigroup A and B of S such that $AB \subseteq P$ implies that $A \subseteq P$ or $B \subseteq P$. An almost subsemigroup P of S is called a semiprime almost subsemigroup (briefly semiprime almost SS) if for any almost subsemigroup A of S such that $AA \subseteq P$ implies that $A \subseteq P$. An almost subsemigroup P of S is called a strongly prime almost subsemigroup (briefly strongly prime almost SS) if for any almost subsemigroups A and B of S such that $AB \cap BA \subseteq P$ implies that $A \subseteq P$ or $B \subseteq P$.

Definition 2.7. Let f_S and g_S be soft sets over the common universe U. Then, soft intersection product $f_S \circ g_S$ is defined by [29]

$$(f_S \circ g_S)(m) = \begin{cases} \bigcup_{m=nr} \{f_S(n) \cap g_S(r)\}, & if \ \exists n, r \in S \ such \ that \ m = nr \\ \emptyset, & otherwise \end{cases}$$

Theorem 2.8. Let $f_S, g_S, h_S \in S_S(U)$. Then,
i) $(f_S \circ g_S) \circ h_S = f_S \circ (g_S \circ h_S)$.
ii) $f_S \circ g_S \neq g_S \circ f_S$, generally.
iii) $f_S \circ (g_S \tilde{\cup} h_S) = (f_S \circ g_S) \tilde{\cup} (f_S \circ h_S)$ and $(f_S \tilde{\cup} g_S) \circ h_S = (f_S \circ h_S) \tilde{\cup} (g_S \circ h_S)$.
iv) $f_S \circ (g_S \tilde{\cap} h_S) = (f_S \circ g_S) \tilde{\cap} (f_S \circ h_S)$ and $(f_S \tilde{\cap} g_S) \circ h_S = (f_S \circ h_S) \tilde{\cap} (g_S \circ h_S)$.

v) If $f_S \tilde{\subseteq} g_S$, then $f_S \circ h_S \tilde{\subseteq} g_S \circ h_S$ and $h_S \circ f_S \tilde{\subseteq} h_S \circ g_S$.
vi) If $t_S, k_S \in S_S(U)$ such that $t_S \tilde{\subseteq} f_S$ and $k_S \tilde{\subseteq} g_S$, then $t_S \circ k_S \tilde{\subseteq} f_S \circ g_S$ [29].
Lemma 2.9. Let f_S and g_S be soft sets over U. Then, $f_S \circ f_S = \emptyset_S \Leftrightarrow f_S = \emptyset_S$.

Definition 2.10. Let A be a subset of S. We denote by S_A the soft characteristic function of A and define as

$$S_A(x) = \begin{cases} U, if\ x \in A \\ \emptyset, if\ x \in S \backslash A \end{cases}$$

The soft characteristic function of A is a soft set over U, that is, $S_A : S \longrightarrow P(U)$ [29].

Corollary 2.11. $supp(S_A) = A$.

Theorem 2.12. Let X and Y be nonempty subsets of S. Then, the following properties hold [29]:

i) $X \subseteq Y$ if and only if $S_X \widetilde{\subseteq} S_Y$

ii) $S_X \widetilde{\cap} S_Y = S_{X \cap Y}$ and $S_X \widetilde{\cup} S_Y = S_{X \cup Y}$

iii) $S_X \circ S_Y = S_{XY}$

Proof: In [29], (i) is given as if $X \subseteq Y$, then if $S_X \widetilde{\subseteq} S_Y$. Now, we also show that if $S_X \widetilde{\subseteq} S_Y$, then $X \subseteq Y$. Let $S_X \widetilde{\subseteq} S_Y$ and $x \in X$. Then, $S_X(x) = U$ and this implies that $S_Y(x) = U$ since $S_X \widetilde{\subseteq} S_Y$. Hence, $x \in Y$ and so $X \subseteq Y$. Now let $x \notin Y$. Then, $S_Y(x) = \emptyset$, and this implies that $S_X(x) = \emptyset$ since $S_X \widetilde{\subseteq} S_Y$. Hence, $x \notin X$ and so $Y' \subseteq X'$, implying that $X \subseteq Y$.

Definition 2.13. A soft set over U is called a soft intersection subsemigroup of S over U if $f_S(xy) \supseteq f_S(x) \cap f_S(y)$ for all $x, y \in S$ [29].

Here note that in [29], the definition of "soft intersection subsemigroup of S" is given as "soft intersection semigroup of S"; however in this paper, without loss of generality, we prefer to use "soft intersection subsemigroup" by the abbreviation of SI-SS [29].

Theorem 2.14. Let f_S be a soft set over U. Then, f_S is an SI-SS if and only if $f_S \circ f_S \widetilde{\subseteq} f_S$ [29].

III. Soft Intersection Almost Subsemigroups of Semigroups

Definition 3.1. Let f_S be a soft set over U. f_S is called soft intersection almost subsemigroup of S if

$$(f_S \circ f_S) \widetilde{\cap} f_S \neq \emptyset_S.$$

Hereafter, soft intersection almost subsemigroup is denoted by SI-almost SS for brevity.

Example 3.2. Let $S = \{s, n, v, j\}$ be the semigroup with the following Cayley Table.

	s	n	v	j
s	s	n	v	j
n	n	s	v	j
v	j	v	j	v
j	v	j	v	j

Let f_S, g_S, and h_S be soft sets over $U = \mathbb{N}$ as follows:

$$f_S = \{(s, \{0,1,2\}), (n, \{1,5\}), (v, \{2,4,6,8\}), (j, \{7,9\})\},$$

$$g_S = \{(s, \{3,5,7\}), (n, \{3,6,9\}), (v, \{12,13\}), (j, \{2,8\})\},$$

$$h_S = \{(s, \emptyset), (n, \{0\}), (v, \{1\}), (j, \emptyset)\}.$$

Here, f_S and g_S are SI-almost SSs. Let's show that $(f_S \circ f_S) \widetilde{\cap} f_S \neq \emptyset_S$.

$[(f_S \circ f_S) \widetilde{\cap} f_S](s) = (f_S \circ f_S)(s) \cap f_S(s) = [(f_S(s) \cap f_S(s)) \cup (f_S(n) \cap f_S(n))] \cap f_S(s) = \{0,1,2\}$

$[(f_S \circ f_S) \widetilde{\cap} f_S](n) = (f_S \circ f_S)(n) \cap f_S(n) = [(f_S(s) \cap f_S(n)) \cup (f_S(n) \cap f_S(s))] \cap f_S(n) = \{1\}$

$[(f_S \circ f_S) \widetilde{\cap} f_S](v) = (f_S \circ f_S)(v) \cap f_S(v) = [(f_S(s) \cap f_S(v)) \cup (f_S(n) \cap f_S(v)) \cup (f_S(v) \cap f_S(n)) \cup (f_S(v) \cap f_S(j)) \cup (f_S(j) \cap f_S(s)) \cup (f_S(j) \cap f_S(v))] \cap f_S(v) = \{2\}$

$[(f_S \circ f_S) \widetilde{\cap} f_S](j) = (f_S \circ f_S)(j) \cap f_S(j) = [(f_S(s) \cap f_S(j)) \cup (f_S(n) \cap f_S(j)) \cup (f_S(v) \cap f_S(s)) \cup (f_S(v) \cap f_S(v)) \cup (f_S(j) \cap f_S(n)) \cup (f_S(j) \cap f_S(j))] \cap f_S(j) = \{7,9\}$

Therefore,

$$(f_S \circ f_S) \mathbin{\tilde{\cap}} f_S = \{(\mathit{s}, \{0,1,2\}), (\mathit{n}, \{1\}), (\mathit{v}, \{2\}), (\mathit{j}, \{7,9\})\} \neq \emptyset_S.$$

It is seen that f_S is an SI-almost SS. Similarly,

$$(g_S \circ g_S) \mathbin{\tilde{\cap}} g_S = \{(\mathit{s}, \{3,5,7\}), (\mathit{n}, \{3\}), (\mathit{v}, \emptyset), (\mathit{j}, \{2,8\})\} \neq \emptyset_S.$$

That is to say, g_S is an SI-almost SS. However, h_S is not an SI-almost SS. In fact;

$$[(h_S \circ h_S) \mathbin{\tilde{\cap}} h_S](\mathit{s}) = (h_S \circ h_S)(\mathit{s}) \cap h_S(\mathit{s}) = \left[\left(h_S(\mathit{s}) \cap h_S(\mathit{s})\right) \cup \left(h_S(\mathit{n}) \cap h_S(\mathit{n})\right)\right] \cap h_S(\mathit{s}) = \emptyset$$

$$[(h_S \circ h_S) \mathbin{\tilde{\cap}} h_S](\mathit{n}) = (h_S \circ h_S)(\mathit{n}) \cap h_S(\mathit{n}) = \left[\left(h_S(\mathit{s}) \cap h_S(\mathit{n})\right) \cup \left(h_S(\mathit{n}) \cap h_S(\mathit{s})\right)\right] \cap h_S(\mathit{n}) = \emptyset$$

$$[(h_S \circ h_S) \mathbin{\tilde{\cap}} h_S](\mathit{v}) = (h_S \circ h_S)(\mathit{v}) \cap h_S(\mathit{v})$$
$$= \left(h_S(\mathit{s}) \cap h_S(\mathit{v})\right) \cup \left(h_S(\mathit{n}) \cap h_S(\mathit{v})\right) \cup \left(h_S(\mathit{v}) \cap h_S(\mathit{n})\right) \cup \left(h_S(\mathit{v}) \cap h_S(\mathit{j})\right)$$
$$\cup \left(h_S(\mathit{j}) \cap h_S(\mathit{s})\right) \cup \left(h_S(\mathit{j}) \cap h_S(\mathit{v})\right)] \cap h_S(\mathit{v}) = \emptyset$$

$$[(h_S \circ h_S) \mathbin{\tilde{\cap}} h_S](\mathit{j}) = (h_S \circ h_S)(\mathit{j}) \cap h_S(\mathit{j})$$
$$= \left[\left(h_S(\mathit{s}) \cap h_S(\mathit{j})\right) \cup \left(h_S(\mathit{n}) \cap h_S(\mathit{j})\right) \cup \left(h_S(\mathit{v}) \cap h_S(\mathit{s})\right) \cup \left(h_S(\mathit{v}) \cap h_S(\mathit{v})\right)\right.$$
$$\cup \left(h_S(\mathit{j}) \cap h_S(\mathit{n})\right) \cup \left(h_S(\mathit{j}) \cap h_S(\mathit{j})\right)] \cap h_S(\mathit{j}) = \emptyset$$

Therefore,
$$(h_S \circ h_S) \mathbin{\tilde{\cap}} h_S = \{(\mathit{s}, \emptyset), (\mathit{n}, \emptyset), (\mathit{v}, \emptyset), (\mathit{j}, \emptyset)\} = \emptyset_S.$$

It is seen that h_S is not an SI-almost SS.

Proposition 3.3. If f_S is an SI-SS such that $f_S \neq \emptyset_S$, then f_S is an SI-almost SS.

Proof: Let $f_S \neq \emptyset_S$ be an SI-SS, then, $f_S \circ f_S \mathbin{\tilde{\subseteq}} f_S$. By Lemma 2.9, since $f_S \neq \emptyset_S$ it follows that $f_S \circ f_S \neq \emptyset_S$. We need to show that

$$(f_S \circ f_S) \mathbin{\tilde{\cap}} f_S \neq \emptyset_S.$$

Since $f_S \circ f_S \mathbin{\tilde{\subseteq}} f_S$, then $(f_S \circ f_S) \mathbin{\tilde{\cap}} f_S = (f_S \circ f_S) \neq \emptyset_S$. Thus, f_S is an SI-almost SS.

Here it is obvious that $\emptyset_S$ is an SI-SS as $\emptyset_S \circ \emptyset_S \mathbin{\tilde{\subseteq}} \emptyset_S$; but it is not an SI-almost SS since $(\emptyset_S \circ \emptyset_S) \mathbin{\tilde{\cap}} \emptyset_S = \emptyset_S \mathbin{\tilde{\cap}} \emptyset_S = \emptyset_S$.

Here note that if f_S is an SI-almost SS, then f_S needs not to be an SI-SS as shown in the following example:

Example 3.4. In Example 3.2, it is shown that f_S and g_S are SI-almost SSs; however f_S and g_S are not SI-SSs. In fact,

$$(f_S \circ f_S)(\mathit{s}) = \left(f_S(\mathit{s}) \cap f_S(\mathit{s})\right) \cup \left(f_S(\mathit{n}) \cap f_S(\mathit{n})\right) =$$
$$= \{0,1,2,5\} \nsubseteq f_S(\mathit{s})$$

and so f_S is not an SI-SS. Similarly, g_S is not an SI-SS. In fact;

$$(g_S \circ g_S)(\mathit{j}) = \left[\left(g_S(\mathit{s}) \cap g_S(\mathit{j})\right)\right.$$
$$\cup \left(g_S(\mathit{n}) \cap g_S(\mathit{j})\right)$$
$$\cup \left(g_S(\mathit{v}) \cap g_S(\mathit{s})\right)$$
$$\cup \left(g_S(\mathit{v}) \cap g_S(\mathit{v})\right)$$
$$\cup \left(g_S(\mathit{j}) \cap g_S(\mathit{n})\right)$$
$$\cup \left(g_S(\mathit{j}) \cap g_S(\mathit{j})\right)]$$
$$= \{2,8,12,13\} \nsubseteq g_S(\mathit{j})$$

and so g_S is not an SI-SS.

Theorem 3.5. Let $f_S \mathbin{\tilde{\subseteq}} h_S$. If f_S is an SI-almost SS, then h_S is an SI-almost SS.

Proof: Assume that f_S is an SI-almost SS. Hence, $(f_S \circ f_S) \mathbin{\tilde{\cap}} f_S \neq \emptyset_S$. We need to show that $(h_S \circ h_S) \mathbin{\tilde{\cap}} h_S \neq \emptyset_S$. In fact,

$$(f_S \circ f_S) \mathbin{\tilde{\cap}} f_S \mathbin{\tilde{\subseteq}} (h_S \circ h_S) \mathbin{\tilde{\cap}} h_S.$$

Since $(f_S \circ f_S) \mathbin{\tilde{\cap}} f_S \neq \emptyset_S$, it is obvious that $(h_S \circ h_S) \mathbin{\tilde{\cap}} h_S \neq \emptyset_S$. This completes the proof.

Theorem 3.6. Let f_S and h_S be SI-almost SSs. Then, $f_S \mathbin{\tilde{\cup}} h_S$ is an SI-almost SS.

Proof: Since f_S is an SI-almost SS and $f_S \mathbin{\tilde{\subseteq}} f_S \mathbin{\tilde{\cup}} h_S$, $f_S \mathbin{\tilde{\cup}} h_S$ is an SI-almost SS by Theorem 3.5.

Corollary 3.7. The finite union of SI-almost SSs is an SI-almost SS.

Corollary 3.8. Let f_S or h_S be SI-almost SS. Then, $f_S \mathbin{\tilde{\cup}} h_S$ is an SI-almost SS.

Here note that if f_S and h_S are SI-almost SSs, then $f_S \mathbin{\tilde{\cap}} h_S$ needs not to be an SI-almost SS.

Example 3.9. Consider the SI-almost SSs f_S and g_S in Example 3.2. Since,

$f_S \widetilde{\cap} g_S = \{(s, \emptyset), (n, \emptyset), (v, \emptyset), (j, \emptyset)\} = \emptyset_S$
$f_S \widetilde{\cap} g_S$ is not an SI-almost SS.

Proposition 3.10. Let f_S be an idempotent soft set such that $f_S \neq \emptyset_S$. Thus, f_S is an SI-almost SS.

Proof: Assume that $f_S \neq \emptyset_S$ and f_S is an idempotent soft set. Then, $f_S \circ f_S = f_S$. We need to show that

$$(f_S \circ f_S) \widetilde{\cap} f_S \neq \emptyset_S.$$

Since $(f_S \circ f_S) \widetilde{\cap} f_S = f_S \widetilde{\cap} f_S = f_S \neq \emptyset_S$, f_S is an SI-almost SS.

Now, we give the relationship between almost SS and SI-almost SS of S.

Theorem 3.11. Let A be a subset of S. A is an almost SS if and only if S_A, the soft characteristic function of A, is an SI-almost SS, where $\emptyset \neq A \subseteq S$.

Proof: Assume that $\emptyset \neq A$ is an almost SS. Then, $AA \cap A \neq \emptyset$, so there exist $k \in S$ such that $k \in AA \cap A$. Since,

$$\big((S_A \circ S_A) \widetilde{\cap} S_A\big)(k) = (S_{AA} \widetilde{\cap} S_A)(k) =$$
$$= (S_{AA \cap A})(k) = U \neq \emptyset,$$

it follows that $(S_A \circ S_A) \widetilde{\cap} S_A \neq \emptyset_S$. Thus, S_A is an SI-almost SS.

Conversely assume that S_A is an SI-almost SS. Hence, we have $(S_A \circ S_A) \widetilde{\cap} S_A \neq \emptyset_S$. In order to show that A is an almost SS, we should prove that $A \neq \emptyset$ and $AA \cap A \neq \emptyset$. $A \neq \emptyset$ is obvious from assumption. Now,

$$\emptyset_S \neq (S_A \circ S_A) \widetilde{\cap} S_A \Rightarrow \exists k \in S \,;$$
$$\big((S_A \circ S_A) \widetilde{\cap} S_A\big)(k) \neq \emptyset$$
$$\Rightarrow \exists k \in S \,; (S_{AA} \widetilde{\cap} S_A)(k) \neq \emptyset$$
$$\Rightarrow \exists k \in S \,; (S_{AA \cap A})(k) \neq \emptyset$$
$$\Rightarrow \exists k \in S \,; (S_{AA \cap A})(k) = U$$
$$\Rightarrow k \in AA \cap A$$

Hence, $AA \cap A \neq \emptyset$. Consequently, A is an almost SS.

Lemma 3.12. Let f_S be a soft set over U. Then, $f_S \widetilde{\subseteq} S_{supp(f_S)}$.

Proof: We need to show that for all $x \in S$, $f_S(x) \widetilde{\subseteq} S_{supp(f_S)}(x)$. By definition of soft characteristic function of $supp(f_S)$;

$$S_{supp(f_S)}(x) = \begin{cases} \emptyset, x \notin supp(f_S) \\ U, x \in supp(f_S) \end{cases}$$

Let, $x \in supp(f_S)$. Then, $f_S(x) \neq \emptyset$ and so $S_{supp(f_S)}(x) = U$. Thus,

$$\emptyset \neq f_S(x) \subseteq S_{supp(f_S)}(x) = U$$

Hence, $f_S \widetilde{\subseteq} S_{supp(f_S)}$. Now assume that $x \notin supp(f_S)$. Then, $f_S(x) = \emptyset$ and so,

$$\emptyset = f_S(x) \subseteq S_{supp(f_S)}(x)$$

So, $f_S \widetilde{\subseteq} S_{supp(f_S)}$. Therefore, in all circumstances, $f_S \widetilde{\subseteq} S_{supp(f_S)}$.

Theorem 3.13. If f_S is an SI-almost SS, then $supp(f_S)$ is an almost SS.

Proof: Assume that f_S is an SI-almost SS. Thus, $(f_S \circ f_S) \widetilde{\cap} f_S \neq \emptyset_S$. In order to show that $supp(f_S)$ is an almost SS, by Theorem 3.11, it is enough to show that $S_{supp(f_S)}$ is an SI-almost SS. By Lemma 3.12,

$(f_S \circ f_S) \widetilde{\cap} f_S \widetilde{\subseteq} \big(S_{supp(f_S)} \circ S_{supp(f_S)}\big) \widetilde{\cap} S_{supp(f_S)}$

and $(f_S \circ f_S) \widetilde{\cap} f_S \neq \emptyset_S$, it implies that $\big(S_{supp(f_S)} \circ S_{supp(f_S)}\big) \widetilde{\cap} S_{supp(f_S)} \neq \emptyset_S$. Consequently, $S_{supp(f_S)}$ is an SI-almost SS and by Theorem 3.11, $supp(f_S)$ is an almost SS.

Here note that the converse of Theorem 3.13 is not true in general as shown in the following example.

Example 3.14. We know that h_S is not an SI-almost SS in Example 3.2 and it is obvious that $supp(h_S) = \{n, v\}$. Since,

$$\big[(supp(h_S))(supp(h_S))\big] \cap supp(h_S) = [\{n, v\}\{n, v\}] \cap \{n, v\}$$
$$= \{s, v, j\} \cap \{n, v\}$$
$$= \{v\} \neq \emptyset$$

$supp(h_S)$ is an almost SS; although h_S is not an SI-almost SS.

Definition 3.15. Let f_S and h_S be SI-almost SSs such that $h_S \widetilde{\subseteq} f_S$. If $supp(h_S) = supp(f_S)$, then f_S is called a minimal SI-almost SS.

Theorem 3.16. A is a minimal almost SS if and only if S_A, the soft characteristic function of A, is a minimal SI-almost SS, where $\emptyset \neq A \subseteq S$.

Proof: Assume that A is a minimal almost SS. Thus, A is an almost SS, and so S_A is an SI-almost SS

by Theorem 3.11. Let f_S be an SI-almost SS such that $f_S \widetilde{\subseteq} S_A$. By Theorem 3.13, $supp(f_S)$ is an almost SS and by Note 2.6 and Corollary 2.11,

$$supp(f_S) \subseteq supp(S_A) = A.$$

Since A is a minimal almost SS, $supp(f_S) = supp(S_A) = A$. Thus, S_A is a minimal SI-almost SS by Definition 3.15.

Conversely, let S_A be a minimal SI-almost SS. Thus, S_A is an SI-almost SS and A is an almost SS by Theorem 3.11. Let B be an almost SS such that $B \subseteq A$. By Theorem 3.11, S_B is an SI-almost SS, and by Theorem 2.12 (i), $S_B \widetilde{\subseteq} S_A$. Since S_A is a minimal SI-almost SS,

$$B = supp(S_B) = supp(S_A) = A$$

by Corollary 2.11. Thus, A is a minimal almost SS.

Definition 3.17. Let f_S, g_S, and h_S be any SI-almost SSs. If $h_S \circ g_S \widetilde{\subseteq} f_S$ implies that $h_S \widetilde{\subseteq} f_S$ or $g_S \widetilde{\subseteq} f_S$, then f_S is called an SI-prime almost SS.

Definition 3.18. Let f_S and h_S be any SI-almost SSs. If $h_S \circ h_S \widetilde{\subseteq} f_S$ implies that $h_S \widetilde{\subseteq} f_S$, then f_S is called an SI-semiprime almost SS.

Definition 3.19. Let f_S, g_S, and h_S be any SI-almost SSs. If $(h_S \circ g_S) \widetilde{\cap} (g_S \circ h_S) \widetilde{\subseteq} f_S$ implies that $h_S \widetilde{\subseteq} f_S$ or $g_S \widetilde{\subseteq} f_S$, then f_S is called an SI-strongly prime almost SS.

It is obvious that every SI-strongly prime almost SS is an SI-prime almost SS and every SI-prime almost SS is an SI-semiprime almost SS.

Theorem 3.20. If S_P, the soft characteristic function of P, is an SI-prime almost SS, then P is a prime almost SS, where $\emptyset \neq P \subseteq S$.

Proof: Assume that S_P is an SI-prime almost SS. Thus, S_P is an SI-almost SS and thus, P is an almost SS by Theorem 3.11. Let A and B be almost SSs such that $AB \subseteq P$. Thus, by Theorem 3.11, S_A and S_B are SI-almost SSs, and by Theorem 2.12 (i) and (iii), $S_A \circ S_B = S_{AB} \widetilde{\subseteq} S_P$. Since S_P is an SI-prime almost SS and $S_A \circ S_B \widetilde{\subseteq} S_P$, it follows that $S_A \widetilde{\subseteq} S_P$ or $S_B \widetilde{\subseteq} S_P$. Therefore, by Theorem 2.12 (i), $A \subseteq P$ or $B \subseteq P$. Consequently, P is a prime almost SS.

Theorem 3.21. If S_P, the soft characteristic function of P, is an SI-semiprime almost SS, then P is a semiprime almost SS, where $\emptyset \neq P \subseteq S$.

Proof: Assume that S_P is an SI-semiprime almost SS. Thus, S_P is an SI-almost SS and thus, P is an almost SS by Theorem 3.11. Let A be an almost SS such that $AA \subseteq P$. Thus, by Theorem 3.11, S_A is an SI-almost SS, and by Theorem 2.12 (i) and (iii), $S_A \circ S_A = S_{AA} \widetilde{\subseteq} S_P$. Since S_P is an SI-semiprime almost SS, and $S_A \circ S_A \widetilde{\subseteq} S_P$, it follows that $S_A \widetilde{\subseteq} S_P$. Therefore, by Theorem 2.12 (i), $A \subseteq P$. Consequently, P is a semiprime almost SS.

Theorem 3.22. If S_P, the soft characteristic function of P, is an SI-strongly prime almost SS, then P is a strongly prime almost SS, where $\emptyset \neq P \subseteq S$.

Proof: Assume that S_P is an SI-strongly prime almost SS. Thus, S_P is an SI-almost SS and thus, P is an almost SS by Theorem 3.11. Let A and B be almost SSs such that $AB \cap BA \subseteq P$. Thus, by Theorem 3.11, S_A and S_B are SI-almost SSs and by Theorem 2.12,

$$(S_A \circ S_B) \widetilde{\cap} (S_B \circ S_A) = S_{AB} \widetilde{\cap} S_{BA} = S_{AB \cap BA} \widetilde{\subseteq} S_P$$

Since S_P is an SI-strongly prime almost SS and $(S_A \circ S_B) \widetilde{\cap} (S_B \circ S_A) \widetilde{\subseteq} S_P$, it follows that $S_A \widetilde{\subseteq} S_P$ or $S_B \widetilde{\subseteq} S_P$. Thus, by Theorem 2.12 (i), $A \subseteq P$ or $B \subseteq P$. Therefore, P is a strongly prime almost SS.

Conclusıon

In this paper, we established the notion of soft intersection almost subsemigroup, which is an extension of the nonnull soft intersection subsemigroup of semigroups. Given the collection of almost subsemigroups of a semigroup, we observe that a semigroup may be constructed under the binary operation of union for soft sets, but not under the binary of operation of intersection for soft sets. Additionally, we demonstrated how minimality, primeness, semiprimeness, and strongly primeness relate to the soft intersection almost subsemigroup of a semigroup and the almost subsemigroup of a semigroup. Future research can be conducted on a variety of soft intersection almost ideals, such as the left (right/two-sided) ideal, quasi-ideal, interior ideal, bi-ideal, bi-interior ideal, bi-quasi ideal, quasi-interior ideal, weak-interior ideal, bi-quasi-interior ideal of semigroups.

References

1.   Grosek, O., Satko, L. "A New Notion in the Theory of Semigroup". *Semigroup Forum* 20. (1980): 233–240.

2.   Bogdanovic, S., "Semigroups in which Some Bi-ideal is a Group". *Univ. u Novom Sadu Zb. Rad. Prirod.-Mat. Fak. Ser. Mat.* 11. (1981): 261–266.

3.   Wattanatripop, K., Chinram, R., Changphas, T. "Quasi-A-ideals and Fuzzy A-ideals in Semigroups". *Journal of Discrete Mathematical Sciences and Cryptograph* 21. (2018): 1131–1138.

4.   Kaopusek, N., Kaewnoi, T., Chinram, R. "On Almost Interior Ideals and Weakly Almost Interior Ideals of Semigroups". *Journal of Discrete Mathematical Sciences and Cryptograph* 23. (2020): 773–778.

5.   Iampan, A., Chinram, R., Petchkaew, P. "A Note on Almost Subsemigroups of Semigroups". *International Journal of Mathematics and Computer Science* 16, (4). (2021): 1623–1629.

6.   Chinram, R., Nakkhasen, W. "Almost Bi-quasi-interior Ideals and Fuzzy Almost Bi-quasi-interior ideals of Semigroups". *Journal of Mathematics and Computer Science* 26. (2022): 128–136.

7.   Gaketem, T. "Almost Bi-interior Ideal in Semigroups and Their Fuzzifications". *European Journal of Pure and Applied Mathematics* 15, (1). (2022): 281-289.

8.   Wattanatripop, K., Chinram, R., Changphas, T. "Fuzzy Almost Bi-ideals in Semigroups". *International Journal of Mathematics and Computer Science* 13. (2018): 51–58.

9.   Krailoet, W., Simuen, A., Chinram, R., Petchkaew, P. "A Note on Fuzzy Almost Interior Ideals in Semigroups". *International Journal of Mathematics and Computer Science* 16. (2021): 803–808.

10.   Molodtsov, D. "Soft Set Theory-first Results". *Computers and Mathematics with Applications* 37, (4-5). (1999): 19–31.

11.   Maji, P.K., Biswas, R., Roy, A.R. "Soft Set Theory". *Computers and Mathematics with Applications* 45. (2003): 555–562.

12.   Pei, D., and Miao, D. "From Soft Sets to Information Systems". *IEEE International Conference on Granular Computing* 2. (2005): 617-621.

13.   Ali, M.I., Feng, F., Liu, X., Min, W.K., Shabir, M. "On Some New Operations in Soft Set Theory". *Computers Mathematics with Applications* 57, (9). (2009): 1547-1553.

14.   Sezgin, A., Atagün, A.O. "On Operations of Soft Sets". *Computers and Mathematics with Applications* 61, (5). (2011): 1457-1467.

15.   Feng, F., Jun, Y.B., Zhao, X. "Soft Semirings". *Computers and Mathematics with Applications* 56, (10). (2008): 2621-2628.

16.   Ali, M.I., Shabir, M., Naz, M. "Algebraic Structures of Soft Sets Associated with New Operations". *Computers and Mathematics with Applications* 61, (9). (2011): 2647–2654.

17.   Sezgin, A., Ahmad, S., Mehmood, A. "A New Operation on Soft Sets: Extended Difference of Soft Sets". *Journal of New Theory* 27. (2019): 33-42.

18.   Stojanovic, N.S. "A New Operation on Soft Sets: Extended Symmetric Difference of Soft Sets". *Military Technical Courier* 69, (4). (2021): 779-791.

19.   Sezgin, A., Atagün, A.O. "New Soft Set Operation: Complementary Soft Binary Piecewise Plus Operation". *Matrix Science Mathematic* 7, (2). (2023): 125-142.

20.   Sezgin, A., Aybek, F.N. "New Soft Set Operation: Complementary Soft Binary Piecewise Gamma Operation". *Matrix Science Mathematic* 7, (1). (2023): 27-45.

21.   Sezgin, A., Aybek, F.N., Atagün, A.O. "New Soft Set Operation: Complementary Soft Binary Piecewise Intersection Operation". *Black Sea Journal of Engineering and Science* 6, (4). (2023): 330-346.

22.   Sezgin, A., Aybek, F.N., Güngör, N.B. "New Soft Set Operation: Complementary Soft Binary Piecewise Union Operation". *Acta Informatica Malaysia* 7, (1). (2023): 38-53.

23.   Sezgin, A., Demirci, A.M. "New Soft Set Operation: Complementary Soft Binary Piecewise Star Operation". *Ikonion Journal of Mathematics* 5, (2). (2023): 24-52.

24.   Sezgin, A., Yavuz, E. "New Soft Set Operation: Complementary Soft Binary Piecewise Lambda Operation". *Sinop University Journal of Natural Sciences* 8, (2). (2023): 101-133.

25.   Sezgin, A., Yavuz, E. "A New Soft Set Operation: Soft Binary Piecewise Symmetric Difference Operation". *Necmettin Erbakan University Journal of Science and* Engineering 5, (2). (2023): 189-208.

26.   Sezgin, A., Çağman, N. "New Soft Set Operation: Complementary Soft Binary Piecewise Difference Operation". *Osmaniye Korkut Ata University Journal of the Institute of Science and Technology* 7, (1). (2024): 58-94.

27.   Çağman, N., Enginoğlu, S. "Soft Set Theory and Uni-int Decision Making". *European Journal of Operational Research* 207, (2). (2010): 848-855.

28.   Çağman, N., Çıtak, F., Aktaş, H. "Soft Int-group and Its Applications to Group Theory". *Neural Computing and Applications* 2. (2012): 151–158.

29.   Sezer, A.S., Çağman, N., Atagün, A.O., Ali, M.İ., Türkmen, E. "Soft Intersection Semigroups, Ideals and Bi-ideals; A New Application on Semigroup Theory I". *Filomat* 29, (5). (2015): 917-946.

30.   Sezer, A.S., Çağman, N., Atagün, A. O. "Soft Intersection Interior Ideals, Quasi-ideals and Generalized Bi-ideals; A New Approach to Semigroup Theory II". *Journal of Multiple-valued Logic and Soft Computing* 23, (1-2). (2014): 161-207.

31.   Sezgin, A., Orbay, M. "Analysis of Semigroups with Soft Intersection Ideals". *Acta Universitatis Sapientiae Mathematica* 14, (1). (2022): 166-210.

32.   Rao, M.M.K. "Bi-interior Ideals of Semigroups". *Discussiones Mathematicae General Algebra and Applications* 38. (2018): 69–78.

33.   Rao, M.M.K. "Left Bi-quasi Ideals of Semigroups". *Southeast Asian Bulletin of Mathematics* 44. (2020): 369–376.

34.   Rao, M.M.K. "Quasi-interior Ideals and Weak-interior Ideals". *Asia Pacific Journal of Mathematics* 7, (21). (2020): 1-20.

35. Rao, M.M.K. "A Study of a Generalization of Bi-ideal, Quasi Ideal and Interior Ideal of Semigroup". *Mathematica Moravica* 22. (2018): 103–115.

36. Baupradist, S., Chemat, B., Palanivel, K., Chinram, R. "Essential Ideals and Essential Fuzzy Ideals in Semigroups". *Journal of Discrete Mathematical Sciences and Cryptography* 24, (1). (2021): 223-233.

37. Mahmood, T., Rehman, Z.U., Sezgin, A. "Lattice Ordered Soft Near Rings". *Korean Journal of Mathematics* 26, (3). (2018): 503-517.

38. Jana, C., Pal, M., Karaaslan, F., Sezgin, A. "(α, β)-Soft Intersectional Rings and Ideals with Their Applications". *New Mathematics and Natural Computation* 15, (2). (2019): 333–350.

39. Muştuoğlu, E., Sezgin, A., Türk, Z.K. "Some Characterizations on Soft Uni-groups and Normal Soft Uni-groups". *International Journal of Computer Applications* 155, (10). (2016): 1-8.

40. Sezer, A.S., Çağman, N., Atagün, A.O. "Uni-soft Substructures of Groups". *Annals of Fuzzy Mathematics and Informatics* 9, (2). (2015): 235–246.

41. Sezer, A.S. "Certain Characterizations of LA-semigroups by Soft Sets". *Journal of Intelligent and Fuzzy Systems* 27, (2). (2014): 1035-1046.

42. Özlü, Ş., Sezgin, A. "Soft Covered Ideals in Semigroups". *Acta Universitatis Sapientiae Mathematica* 12, (2). (2020): 317-346.

43. Atagün, A.O., Sezgin, A. "Soft Subnear-rings, Soft Ideals and Soft N-subgroups of Near-rings". *Mathematical Science Letters* 7, (1). (2018): 37-42.

44. Sezgin, A. "A New View on AG-groupoid Theory via Soft Sets for Uncertainty Modeling". *Filomat* 32, (8). (2018): 2995–3030.

45. Sezgin, A., Çağman, N., Atagün, A.O. "A Completely New View to Soft Intersection Rings via Soft Uni-int Product". *Applied Soft Computing* 54. (2017): 366-392.

46. Sezgin, A., Atagün, A.O., Çağman, N., Demir, H. "On Near-rings with Soft Union Ideals and Applications". *New Mathematics and Natural Computation* 18, (2). (2022): 495-511.

47. Pant, S., Dagtoros, K., Kholil, M. I., Vivas, A. "Matrices: Peculiar Determinant Property". *Optimum Science Journal*, (1). (2024): 1–7.

Information about authors:

Aslıhan SEZGİN – (corresponding author), Professor of Department of Mathematics and Science Education, Faculty of Education, (Amasya University, Turkey, e-mail: aslihan.sezgin@amasya.edu.tr)

Aleyna İLGİN – Research scholar of Department of Mathematics, Graduate School of Natural and Applied Sciences, Amasya University, (Amasya, Turkey).

Rakesh Kr Saha ⬤ , Hiranmoy Maiti ⬤ , Swati Mukhopadhyay* ⬤

University of Burdwan, Burdwan, West Bengal, India
*e-mail: swati_bumath@yahoo.co.in

Mass diffusion of MHD flow over an unsteady stretched surface with moving free stream

Abstract. An exploration is carried out to examine mass diffusion of unsteady 'boundary layer' (bl) motion of viscous liquid passed a stretched leaky piece with variable mass flux. For several engineering applications, moving free stream is considered here. This makes this research unique. The leading 'partial differential equations' (PDEs) accompanied by the 'boundary conditions' are converted to 'ordinary differential equations' (ODEs) with the help of 'similarity transformations' and 'numerical solutions' are attained by MATLAB software. The effect of pertinent 'parameters' on fluid 'flow, concentration, skin friction coefficient' and wall concentration are discussed 'graphically' and numerically. When suction/blowing parameter increases from -0.2 to 0.2, skin friction coefficient decreases 18.235%. Fluid concentration reduces with growing values of velocity ratio parameter λ for all cases considered. Compared to the case for static free stream, fluid velocity is higher when the free stream moves. Also higher concentration is noted in presence of moving free stream. The presence of moving free stream causes to diminish the effect of suction/blowing on flow and concentration fields. The increasing strength of suction causes to decrease the fluid velocity more significantly than that for blowing.
Key words: Unsteady stretching sheet, MHD, Mass diffusion, Variable free stream, Variable mass flux.

Introduction

Mass transport phenomenon in the branch of 'fluid mechanics' has achieved huge attention of the researchers due to its frequent occurrence in natural processes as well as industrial processes. Basically by mass transfer we mean the movement of molecules of substances or chemical species within or between fluid mediums. Generally this mass transfer process can be completed by two processes, diffusion and convection. There are several key factors which influence the rate of mass transfer including concentration difference, diffusion coefficient, temperature, surface area, fluid velocity etc. Mass transfer plays a crucial role in controlling and optimizing several processes across different sectors including chemical reactors, distillation, gas-liquid extraction, crystallization, waste water treatment, air pollution control, fermentation, fuel cells, batteries, micro fluidic devices etc. In these applications, product quality, environmental sustainability are improved by manipulating mass transfer. Chambre and Young [1] considered chemically reactive species, diffused into the fluid showed its effect on mass transfer. Mukhopadhyay

[2] examined solute transfer for laminar bl flow through a stretched 'cylinder' and for motion of fluid and mass transport, numerical solutions were obtained. Mukhopadhyay and Gorla [3] studied mass transfer in a 'upper convected Maxwell' liquid flow taking homogeneous/heterogeneous chemical reaction over an unsteady stretched sheet. Their study explored that speed of mass transport from the exterior was enhanced by the reaction rate. Srinivas et al. [4] analysed the mass transfer and fluid flow in an absorbent 'channel' having static or 'moving walls' in attendance of compound response. Mukhopadhyay et al. [5] considered a chemically reactive fluid flow over a moving plate. Maleque [6] investigated mass transfer of 'unsteady bl flow' influenced by natural convection and binary chemical reaction. Mukhopadhyay et al. [7] studied mass diffusion in an incompressible 'viscous' liquid 'flow' owing to a stretched permeable exterior by taking stratified medium. Mukhopadhyay [8] examined the transportation of mass in a chemically reactive liquid 'flow' through a stretched 'cylinder' in an absorbent 'medium'.

Magnetohydrodynamics (MHD) refers to the study of 'electrically conducting' liquid flows in

attendance of 'magnetic field'. In MHD, 'magnetic' properties and performance of 'electrically conducting' liquids such as salt water, plasma, liquid metals are generally studied. The 'interaction between' applied 'magnetic field' and moving fluid generates Lorentz forces which in turn affect the original flow. In several sectors viz. in industrial and engineering sectors where electrically conducting fluid and magnetic field are used, MHD has huge applications. Some of the applications include magnetic pumps, MHD power generation, micro fluidic devices, liquid metal cooling in Nuclear reactors, MHD heat transfer etc. Hayat et al. [9] analyzed mass transfer of an elastic 'viscous' liquid and showed the effect of 'magnetic field' applying homotopy analysis method. Shehzadi et al. [10] examined MHD flow of casson fluid and studied the mass transport behaviour. Babu et al. [11] inspectd the consequences of mass transfer and viscous dissipation in 'MHD' convective flow of micropolar liquid over moving permeable plate. Nayak et al. [12] considered 'free convective' flow of 'viscoelastic' liquid over an 'inclined plate'. They also analyzed the consequences of 'magnetic field' on 'flow and mass' transport. The impact of magnetic field on convective viscous dissipative fluid flow was investigated by Reddy [13]. Agarwalla and Ahmed [14] also studied 'MHD' convection fluid 'flow and mass transport'. But they found the exact solutions by taking variable plate velocity. Swain and Barik [15] considered 'MHD' mixed convective second grade fluid motion passing an upright infinite plate.

In the field of fluid mechanics, a stretching sheet is a thin material continuously stretched in one direction. For the understanding of bl flows, fluid-solid interactions, heat transport features, liquid motion due to a stretched piece plays important role. In several scientific fields and industrial processes, its applications including polymer and fibre production, metal sheet forming, coating processes, material science and engineering, modelling biological fluids, optimizing industrial processes, paper production become valuable tools. Researchers generally investigate flow due to a stretched piece in their studies considering different types of stretching velocities viz. linear stretching velocity, power-law stretching velocity, exponential stretching velocity, unsteady strething velocity etc. Kandasamy et al. [16] studied 'mass' transport of laminar flow past a porous stretched piece with Soret and Dufour consequences, thermophoresis and

chemical reaction by group theoretic approach. Elbashbeshy and Sedki [17] examined the influence of compound response on solute transport passed a stretched exterior in absorbent 'medium'. Rosly et al. [18] considered unsteady flow near a 'stagnation point' with 'mass' transport due to a porous surface and presented stability analysis. Takhar et al. [19] considered 'electrically conducting viscous' liquid flow past a stretched exterior and examined flow and mass transfer properties. Afify [20] analyzed consequences of 'magnetic field' on 'mass' transport of 'chemically reactive' convective motion past a stretched piece. Bhattacharyya et al. [21] examined MHD chemically reacting bl 'flow' past a permeable stretched piece. Mazid et al. [22] inspectd the combined impacts of chemical reaction, Soret and suction on motion of 'Maxwell ferro' liquid considering 'magnetic dipole'.

Consideration of mass flux condition at the boundary makes the mass transfer characteristics more interesting and meaningful in case of viscous fluid flow. Mass flux is mostly applied in designing and analyzing pipe flow for transporting liquid, gases, in heat exchangers, water treatment plant, ventilation system, chemical industries etc. Ganesan and Palani [23] developed a fluid model for an unsteady convective 'MHD flow' past an 'inclined plate'. Using 'finite difference method', they showed the consequences of mass flux on 'flow' characteristics. Saravana et al. [24] considered the impact of constant 'mass' flux on mass transfer for 'MHD viscous flow' over 'an infinite upright plate'. 'Unsteady convective' flow of 'viscous' liquid over a upright 'plate' was measured by Loganathan and Sivapoornapriya [25] and impact of mass flux was shown in their work. Abbasi et al. [26] explored the effects of 'mass flux' on MHD 'flow of Jeffrey' fluid. Das et al. [27] considered unsteady 'convective flow' past an upright 'plate' with mass flux. Ghosh and Mukhopadhyay [28] analyzed 'flow, heat and mass' transport in nanoliquid past an exponentially shrinking piece with mass flux. Palaniammal and Saritha [29] examined the concequences of 'mass flux' on fluid characteristics for MHD casson fluid flow.

The above discussion of existing literature encourages us to investigate mass diffusion of 'MHD' bl 'flow' past an unsteady stretching piece with variable mass flux, 'suction'/blowing and moving free stream. From existing literature, it is noted that some researchers analyzed 'MHD flow' owing to 'unsteady' stretched piece, some of them

investigated MHD 'flow and mass' transport over an 'unsteady' stretched exterior by considering chemical reaction. But as per author's knowledge, no one has yet considered MHD 'flow' and mass transport owing to an unsteady stretched surface with changeable chemical reaction, variable mass flux at the surface in presence of moving free stream. To fill this research gap, we have inspected the problem. Here lies the novelty of the present work. Our investigation will sort out the answers for the following questions:

(i)   What are the key features of flow and mass transfer when moving free stream is considered?

(ii)   How does variable mass flux influence mass transfer and concentration of the fluid?

(iii)   How do unsteadiness and magnetic field influence the 'flow' and concentration 'fields' in attendance of moving free stream?

Mathematical formulation

A 2D (two-dimensional) unsteady laminar bl flow of 'viscous electrically conducting' liquid in attendance of applied 'magnetic field', chemical reaction and variable mass flux at the boundary is modelled in the current investigation. The liquid is assumed to flow over a porous stretched piece which is stretched with time dependent velocity

$U_w(x,t) = \dfrac{bx}{1-\alpha t}$ where α being invariable of dimension $(time)^{-1}$ and b is another constant. The geometry of this fluid model is provided in Figure1.
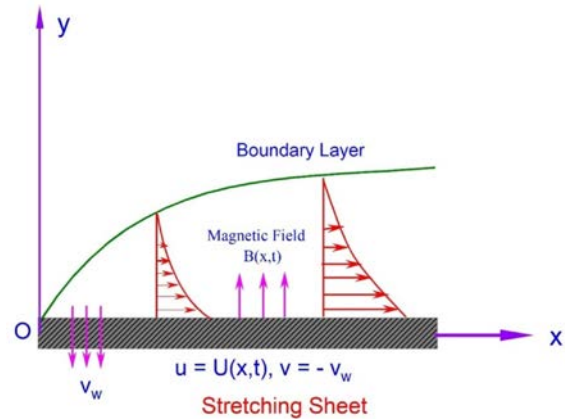
Figure 1 – Sketch of the physical flow problem

Here, moving free stream having velocity $U_\infty = \dfrac{ax}{1-\alpha t}$, a is a constant, is considered. By considering the above suppositions, the leading 'equations' of motion for this problem are as follows:

$$\frac{\partial u}{\partial x} + \frac{\partial v}{\partial y} = 0, \tag{1}$$

$$\frac{\partial u}{\partial t} + u\frac{\partial u}{\partial x} + v\frac{\partial u}{\partial y} = \upsilon\frac{\partial^2 u}{\partial y^2} + \frac{\partial U_\infty}{\partial t} + U_\infty\frac{\partial U_\infty}{\partial x} - \frac{\sigma B^2(x,t)}{\rho}(u - U_\infty), \tag{2}$$

$$\frac{\partial C}{\partial t} + u\frac{\partial C}{\partial x} + v\frac{\partial C}{\partial y} = D\frac{\partial^2 C}{\partial y^2} - \mathrm{K}(x,t)(C - C_\infty). \tag{3}$$

Moving free stream is considered. So the boundary conditions are given by

$$u = U_w(x,t) = \frac{bx}{1-\alpha t},$$
$$v = -\frac{v_0}{\sqrt{1-\alpha t}} = -v_w, \text{ at } y = 0, \tag{4}$$
$$-D\frac{\partial C}{\partial y} = q_m(x,t)$$

$$u \to U_\infty(x,t) = \frac{ax}{1-\alpha t}, C \to C_\infty \text{ as } y \to \infty. \tag{5}$$

Here x axis is taken alongside the stretched piece and y axis is assumed perpendicular to the piece. u and v are considered as 'velocity components' of the fluid respectively along x axis and y axis. υ is the 'kinematic' coefficient of 'viscosity', ρ denotes 'density' of liquid and σ is considered as 'electrical conductivity' of the fluid.

$B(x,t) = \dfrac{B_0}{(1-\alpha t)}$ represents the variable 'magnetic field' strength applied perpendicular to the sheet i.e. parallel to y axis and B_0 is the uniform strength of the magnetic field. C denotes the 'concentration' of the fluid, D denotes 'diffusion coefficient', C_∞ represents constant concentration distant from the sheet and $\mathrm{K}(x,t)$ represents variable reaction rate of solute which is defined as $\mathrm{K}(x,t) = \dfrac{\mathrm{K}_0}{(1-\alpha t)}$ where K_0 is uniform reaction rate. v_w represents 'suction/blowing through' the permeable piece and defined as $v_w = \dfrac{v_0}{\sqrt{1-\alpha t}}$, where $v_0 < 0$ defines blowing and $v_0 > 0$ defines suction, $q_m(x,t)$ denotes the variable surface mass flux and is given by $q_m(x,t) = \dfrac{C_0 dx^{\mathrm{r}}}{(1-\alpha t)^{m+\frac{1}{2}}}$ where C_0 is constant value of reference concentration and d is also constant; r, m are power-law indices and r represents space variation of mass flux whereas m denotes the time variation of mass flux.

Similarity transformations

In order to solve the PDEs (1)-(3) subject to the 'conditions' at the 'boundary' given by (4)-(5) respectively, these PDEs are converted to ODEs. For this, suitable similarity transformations are employed which are given by:

$$\psi = \sqrt{\upsilon x U(x,t)}\, f(\eta), \quad \eta = y\sqrt{\frac{U(x,t)}{\upsilon x}} \;,$$

$$C = C_\infty + C_0 \frac{dx^{\mathrm{r}}}{D\sqrt{\dfrac{b}{\upsilon}}} (1-\alpha t)^{-\mathrm{m}} \phi(\eta), \tag{6}$$

where ψ denotes 'stream function' and given by

$$u = \frac{\partial \psi}{\partial y}, v = -\frac{\partial \psi}{\partial x}. \tag{7}$$

Using (6) and (7) in (1) – (5) we get the transformed 'equations'

$$f''' + ff'' - f'^2 - \mathrm{A}\left(\frac{\eta}{2}f'' + f'\right) -$$
$$-\mathrm{M}(f' - \lambda) + \mathrm{A}\lambda + \lambda^2 = 0, \tag{8}$$

$$\frac{1}{\mathrm{Sc}}\phi'' - \mathrm{A}(\mathrm{m}\phi + \frac{\eta}{2}\phi') - \mathrm{r}f'\phi + f\phi' - \mathrm{k}_1\phi = 0, \tag{9}$$

with the 'boundary conditions'

$$f'(0) = 1, f(0) = \mathrm{S}, \phi'(0) = -1 \text{ at } \eta = 0, \tag{10}$$

$$f'(\eta) \to \lambda \text{ and } \phi(\eta) \to 0 \text{ as } \eta \to \infty. \tag{11}$$

Here $\mathrm{A} = \dfrac{\alpha}{b}$ represents unsteadiness parameter, $\mathrm{M} = \dfrac{\sigma B_0^2}{\rho b}$ denotes the 'magnetic parameter', $\mathrm{Sc} = \dfrac{\upsilon}{b}$ is the 'Schmidt number' and $\mathrm{k}_1 = \dfrac{\mathrm{K}_0}{(1-\alpha t)}$ represents chemical reaction parameter.

$\mathrm{S} = \dfrac{v_0}{\sqrt{\upsilon b}}$ represents suction (>0) /blowing (<0) parameter, $\lambda = \dfrac{a}{b}$ denotes velocity ratio parameter.

Numerical computations and its validation

The reduced the ODEs (8) and (9) are solved by numerically by considering the boundary conditions (10) and (11). For numerical computation, famous package of solving boundary value problem called bvp4C in MATLAB platform is employed. Before preceding the detail computations for the current problem, comparisons of the received data have been made with the available data found from existing literatures for checking the correctness of the 'numerical scheme'. In Table-I, $f''(0)$ for different data of 'unsteadiness parameter' A received for $\lambda = 0$ [i.e. when the free stream is not moving $(U_\infty = 0)$] are evaluated with the outcomes obtained by Sharidan et al. [30], Chamkha et al. [31]

and Bhattacharyya et al. [21]. Another comparison for the outcomes related to $f''(0)$ for some 'values of' unsteadiness parameter A, magnetic parameter M and 'suction/blowing parameter' S received in our case for $\lambda = 0$ is completed with the outcomes obtained by Bhattacharyya et al. [21] which is shown in Table-II. In both cases, an excellent agreement has been found.

Results and discussions

The influences of the non-dimensional parameters on velocity $f'(\eta)$, concentration $\phi(\eta)$, velocity gradient at the surface $f''(0)$ and surface concentration $\phi(0)$ have been presented through Table III, Figures 2-16 and analysed by taking some numerical values of the parameters available in existing literature.

Table I – Values of $f''(0)$ for various values of A with M=0, S=0 and $\lambda = 0$

A	$f''(0)$			
	Sharidan et al. [30]	Chamkha et al. [31]	Bhattacharyya et al. [21]	Present Study
0.8	-1.261042	-1.261512	-1.261487	-1.26106
1.2	-1.377722	-1.378052	-1.377910	-1.3779

Table II – Values of $f''(0)$ for various values of A, M and S for $\lambda = 0$

A	M	S	$f''(0)$	
			Bhattacharyya et al. [21]	Present Study
0	1	1	-1.9994675	-2.0
0.5	1	1	-2.1052957	-2.10567
1	1	1	-2.2085607	-2.20858
0.5	0	1	-1.7474293	-1.74853
0.5	0.5	1	-1.9389309	-1.93907
0.5	1	-1	-1.1300147	-1.13084
0.5	1	0	-1.5387832	-1.53905

Table III – Values of $f''(0)$ and $\phi(0)$ for various values of S for $\lambda = 0$ and $\lambda = 0.1$ when A=0.2, M=0.5, m=2, r=2, Sc=0.7, k_1=0.5

S	$f''(0)$		$\phi(0)$	
	$\lambda = 0$	$\lambda = 0.1$	$\lambda = 0$	$\lambda = 0.1$
-0.2	-1.18795	-1.12083	0.792108	0.781387
-0.15	-1.21084	-1.14187	0.783064	0.772279
-0.1	-1.23421	-1.16332	0.774098	0.763254
0	-1.28241	-1.20748	0.756398	0.745453
0.1	-1.33257	-1.25332	0.739007	0.727986
0.15	-1.35838	-1.27687	0.730426	0.719379
0.2	-1.38468	-1.30083	0.721922	0.710855

The influences of magnetic parameter (M) on velocity and concentration when suction and blowing are separately applied to the flow field are depicted in Figure 2 and 3 respectively. Figure 2 depicts that the velocity of the fluid decreases with enhancing values of M for both cases of suction and blowing. But for blowing velocity decreases quicker than for suction. The nature of this velocity profiles is fundamentally true as the enhancing values of M generates resistve force known as Lorentz force which opposes the motion of the fluid. Also for moving free stream thinning of boundary layer occurs. The influences of M on concentration are depicted in Figure 3 which explores that for both

suction and blowing concentration increases with enhancing values of M. The enhancing values of M

causes to decrease the fluid velocity which in turn causes to increase the fluid concentration.
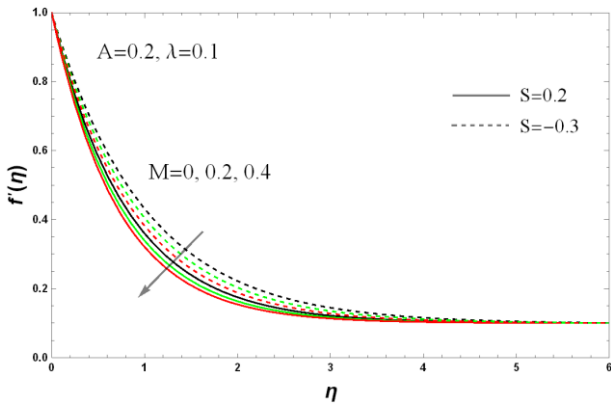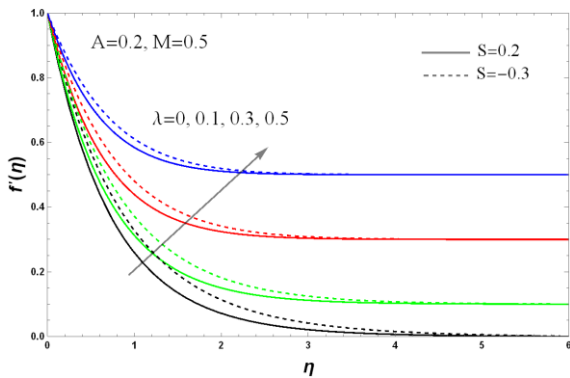

Figure 2 – Variations of velocity $f'(\eta)$
for various values of M
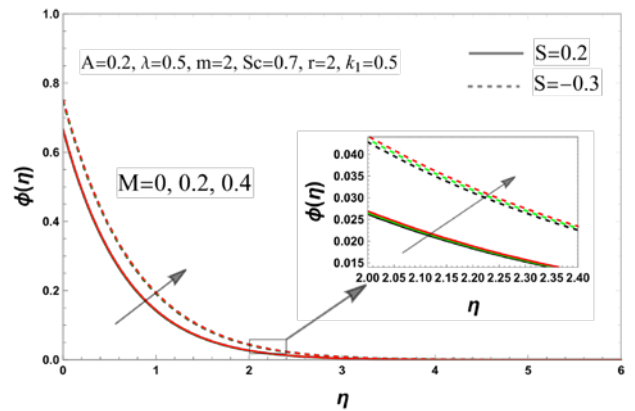
Figure 3 – Variations of concentration $\phi(\eta)$
for various values of M

Figure 4 explores that velocity of the fluid decreases with enhancing values of unsteadiness parameter (A) for both suction and injection cases. Physically the enhancing values of A adds to higher resistance in the fluid motion which reduces the fluid velocity. Higher velocity is noted for blowing

compared to suction. From Figure 5 it is seen that the concentration of the fluid decreases with enhancing values of A. Solute bl thickness diminishes for unsteadiness. It is also observed that compared to blowing more decrease in concentration is noted for suction.
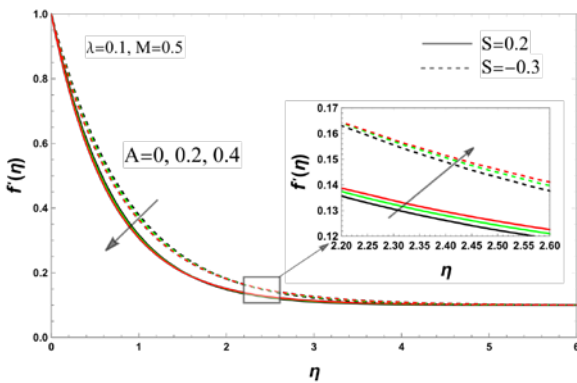
**Figure 4** – Variations of velocity $f'(\eta)$
for various values of A
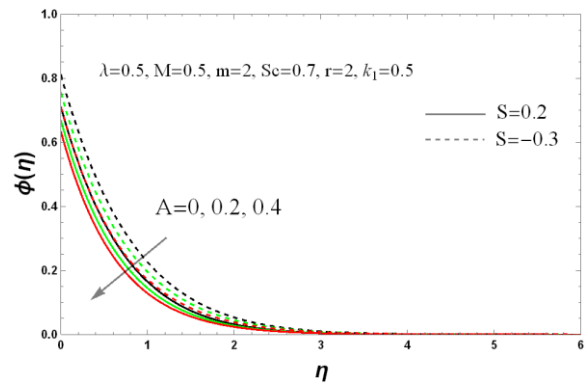
Figure 5 – Variations of concentration $\phi(\eta)$
for various values of A

The rising values of suction/blowing parameter S compresses the fluid velocity which is presented in Figure 6. Fluid velocity is slightly higher for steady case compared to unsteady flow. Thickness of bl reduces with the rise in S. Figure 7 shows the effect of suction/blowing

parameter S on fluid concentration. From this figure it is shown that fluid concentration decreases with increasing values of S. It is also observed that concentration decreases more in unsteady flow which is obvious. Here also width of solute bl becomes thinner for rising S.
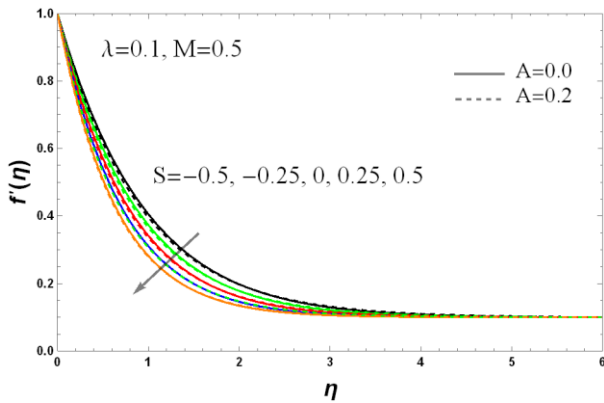
Figure 6 – Variations of velocity $f'(\eta)$
for various values of S
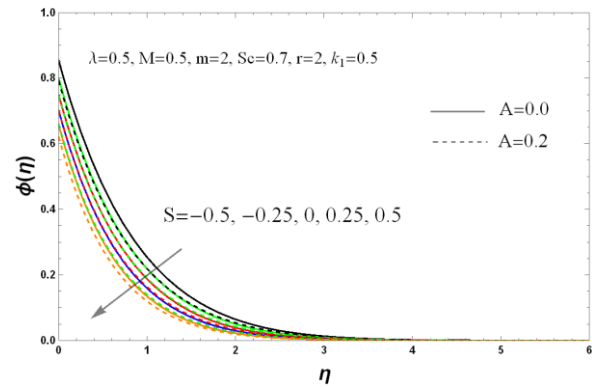
Figure 7 – Variations of concentration $\phi(\eta)$
for various values of S

Figures 8(a)-(b) depict the variation of velocity ratio parameter λ on velocity of the fluid. It is evident that the velocity of the fluid rises with enhancing values of λ and bl formation is observed [Figure 8(a)] for $\lambda < 1$. $\lambda = 0$ means the free stream is not moving. So, one can conclude that moving free stream compels the fluid to move faster [Figure 8(a)].

When the sheet is stretched with equal velocity as of free stream velocity i.e. for $\lambda = 1$, no bl formation is noted and an inverted bl is created when free stream velocity is greater than the stretching velocity which is depicted in Figure 8(b). From Figure 8(a), it is also observed that the effects of both suction and blowing gradually decreases with increasing values of λ.

Figure 8a – Variations of velocity $f'(\eta)$
for various values of $\lambda(<1)$
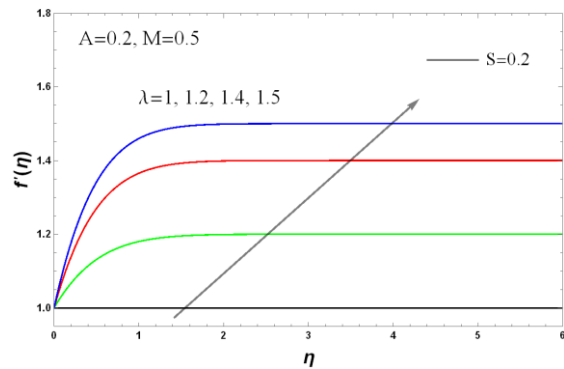
Figure 8b – Variations of velocity $f'(\eta)$
for various values of $\lambda(\geq 1)$

From Figures 9(a)-(b) it is noticed that concentration of the fluid deceases with increasing values of velocity ratio parameter λ both for $\lambda < 1$ [Figure 9(a)] and $\lambda \geq 1$ [Figure 9(b)]. Higher concentration is noted when the free stream is not moving [Figure 9(a)].

The fluid concentration decreases with enhancing values of Schmidt number Sc which is depicted in Figure 10. This figure also shows that suction compresses the fluid concentration more than that of blowing.
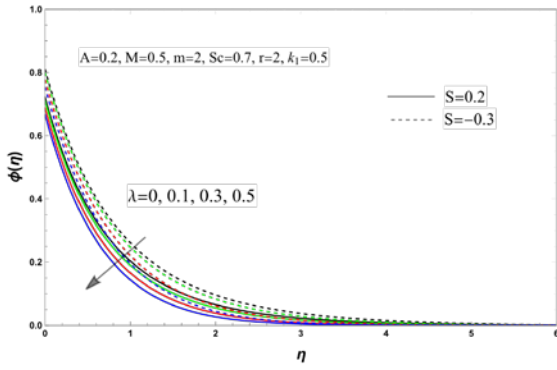
Figure 9a – Variations of concentration $\phi(\eta)$
for various values of $\lambda(<1)$
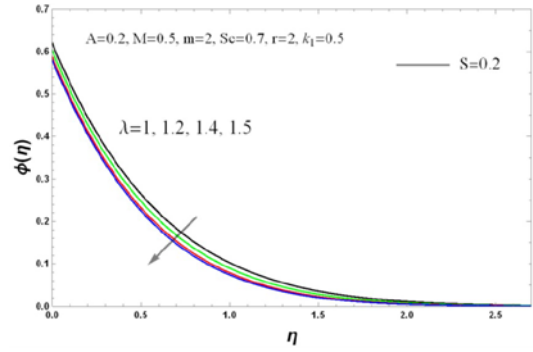
Figure 9b – Variations of concentration $\phi(\eta)$
for various values of $\lambda(\geq 1)$
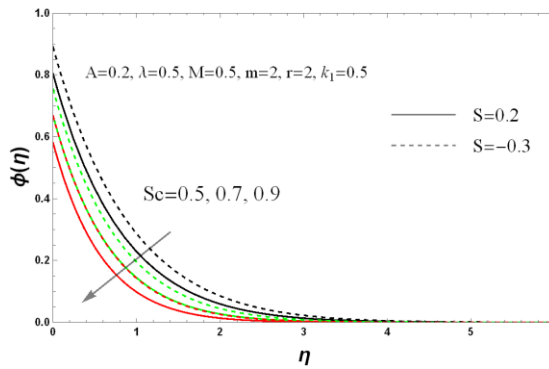
Figure 10 -Variations concentration $\phi(\eta)$
for various values of Sc

Variable mass flux at the boundary plays an important role which can be viewed by the impact of the variations of m and r on concentration profiles. Figures 11 and 12 represent the behaviours of fluid concentration for different values of m and r respectively. These figures explore that concentration of the fluid decreases with increasing values of both m and r for both suction and blowing. But the enhancing values of r [Figure 12] affect the fluid concentration more than that of m [Figure 11]. Physically this can be explained as: with rising values of m unsteadiness of mass flux increases which in turn causes to decrease the fluid concentration. This is obvious and one can easily understand this feature from the last condition given by Equation (5). Moreover, thinner solute bl is observed as the mass flux differs with time and distance along the surface i.e. for higher values of power indices m and r.
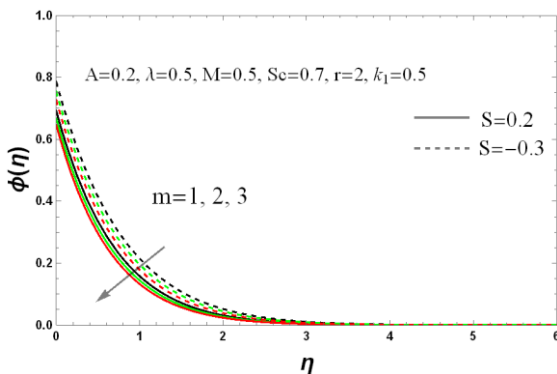
Figure 11 – Variations of concentration $\phi(\eta)$ for various
values of m
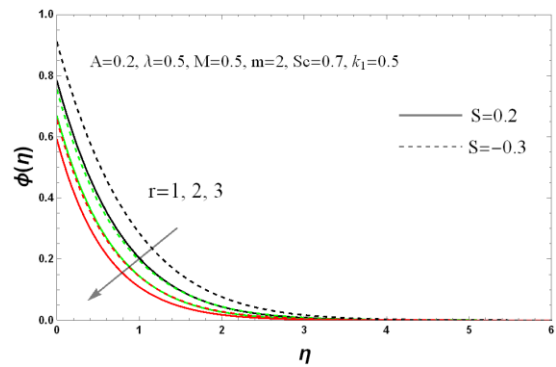
Figure 12 – Variations of concentration $\phi(\eta)$
for various values of r

The impact of chemical reaction parameter k_1 on concentration of the fluid is explored in Figure 13 which shows that fluid concentration decreases with increasing values of chemical reaction parameter k_1 for both suction and blowing. Here, $k_1 = 0$ means there is no chemical reaction.

The behaviours of velocity gradient at the surface $f''(0)$ with A for different values of magnetic parameter M are shown in Figures 14. We know that skin friction coefficient is proportional to $f''(0)$ so one can say from Figure 14 that skin friction coefficient decreases with rising values of M. The developed resisting force by enhancing magnetic field causes the decrement of skin friction coefficient. It is also observed that skin friction coefficient is compressed when moving outer flow is taken into account [Table III]. Figure 15 shows the variation of wall concentration with A for different values of M. In the figure wall concentration increases with enhancing values of M whereas it diminishes with the rising values of unsteadiness paraneter A [Figure 15].
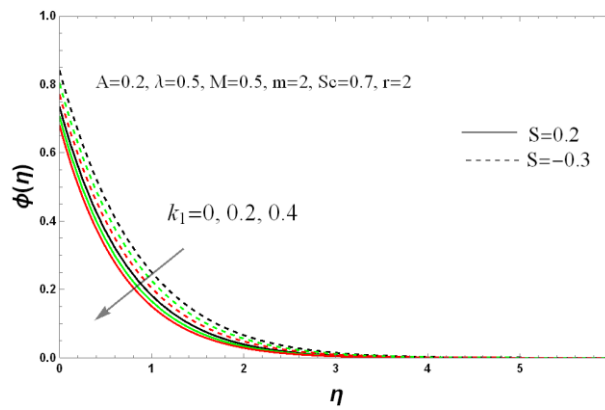
Figure 13 – Variations of concentration $\phi(\eta)$

for various values of k_1
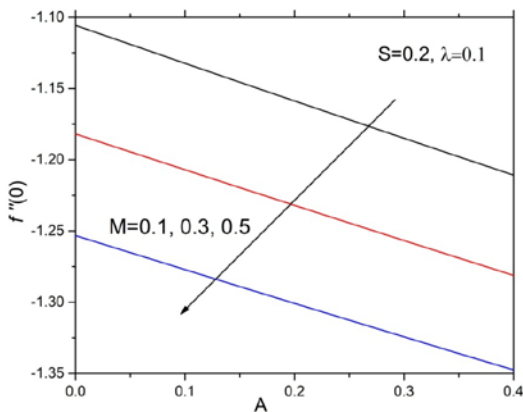
Figure 14 – Variations of velocity gradient at the wall $f''(0)$ with A for different values of M
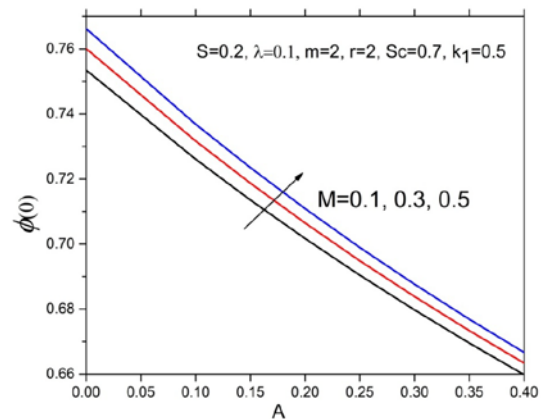
Figure 15 – Variations of wall concentration $\phi(0)$ with A for different values of M
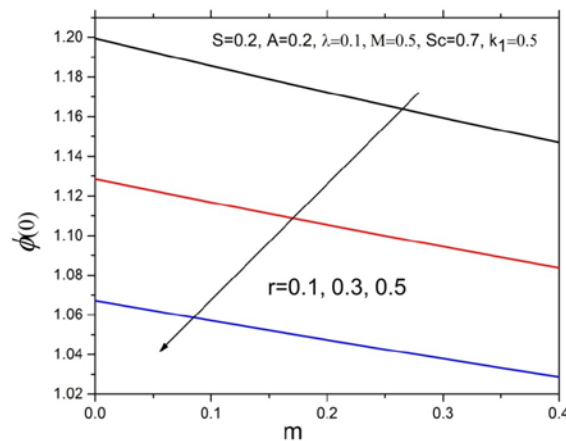
Figure 16 – Variations of wall concentration $\phi(0)$
with m for different values of r

Wall concentration decreases with increasing values of m and r which is depicted in Figures 16. Variations of surface shear stress $f''(0)$ and wall concentration $\phi(0)$ for different values of S are numerically presented in Table III. From this table it is observed that when the values of S increases from -0.2 to 0.2, $f''(0)$ decreases from -1.18795 to -1.38468 for static free stream ($\lambda = 0$) whereas for moving free stream ($\lambda = 0.1$) it decreases from -1.12083 to -1.32521. Consequently, it is concluded that moving free stream compresses the skin friction coefficient. Similar type of behaviour is observed for wall concentration which is shown in Table III.

Conclusions

Mass transfer of an unsteady chemically reactive MHD boundary layer flow over a stretching sheet in presence of variable mass flux and moving free stream is considered. Suitable similarity transformations are employed to find self-similar equations which are solved numerically with the help of bvp4C. The impact of several controlling parameters on flow and mass transfer are analysed graphically and demonstrated comprehensively through tables. Following are the remarkable observations of this study:

(i) The rising values of magnetic parameter M, unsteadiness parameter A, suction/blowing parameter S compress the fluid velocity.

(ii) Fluid velocity is found to rise for improved values of λ and bl structure is noted for $\lambda < 1$. Inverted bl structure is observed for $\lambda > 1$ and no bl structure is observed for $\lambda = 1$.

(iii) Fluid concentration reduces with growing values of velocity ratio parameter λ for all cases considered.

(iv) Compared to the case for static free stream, fluid velocity is higher when the free stream moves. Also higher concentration is noted in presence of moving free stream.

(v) The presence of moving free stream causes to diminish the effect of suction/blowing on flow and concentration fields.

(vi) The increasing strength of suction causes to decrease the fluid velocity more significantly than that for blowing.

(vii) Fluid concentration decreases with enhancing values of chemical reaction parameter k_1, power-law indices r and m whereas concentration is found to increase for increasing values of magnetic parameter M.

(viii) Skin friction coefficient decreases whereas wall concentration increases with the rising values of M.

References

1.   P.L. Chambré, and J.D. Young, On the diffusion of a chemically reactive species in a laminar boundary layer flow. *The Physics of fluids*,1958, *1*(1), pp.48-54.

2.   S. Mukhopadhyay, Chemically reactive solute transfer in a boundary layer slip flow along a stretching cylinder. *Frontiers of Chemical Science and Engineering,* 2011, 5, pp.385-391.

3.   S. Mukhopadhyay, R.S.R. Gorla, Unsteady MHD boundary layer flow of an upper convected Maxwell fluid past a stretching sheet with first order constructive/destructive chemical reaction. *Journal of Naval Architecture & Marine Engineering*, 2012, 9(2), pp.123-133.

4.   S. Srinivas, A. Gupta, S. Gulati, and A.S. Reddy, Flow and mass transfer effects on viscous fluid in a porous channel with moving/stationary walls in presence of chemical reaction. *International communications in heat and mass transfer*,2013, *48*, pp.34-39.

5.   S. Mukhopadhyay, K. Vajravelu, and R.A. Van Gorder, Chemically reactive solute transfer in a moving fluid over a moving surface. *Acta Mechanica*, 2013, *224*(3), pp.513-523.

6.   K.A. Maleque, Unsteady natural convection boundary layer flow with mass transfer and a binary chemical reaction. *British Journal of Applied Science & Technology*, 2013, *3*(1), pp.131-149.

7.   S. Mukhopadhyay, K. Bhattacharyya and G.C. Layek, Mass transfer over an exponentially stretching porous sheet embedded in a stratified medium. *Chem. Engng. Commun.*, 2014, 201(2), pp. 272-286.

8.   S. Mukhopadhyay, Chemically reactive solute transfer in boundary layer flow along a stretching cylinder in porous medium. *Afrika Matematika*, 2014, *25*, pp.1-10.

9.   T. Hayat, M. Qasim, and Z. Abbas, Three-dimensional flow of an elastico-viscous fluid with mass transfer. *International journal for numerical methods in fluids*,2011, *66*(2), pp.194-211.

10.   S.A. Shehzad, T. Hayat, M. Qasim, and S. Asghar, Effects of mass transfer on MHD flow of Casson fluid with chemical reaction and suction. *Brazilian Journal of Chemical Engineering*, 2013, *30*, pp.187-195.

11.   M.S. Babu, J.G. Kumar, and T.S. Reddy, Mass transfer effects on unsteady MHD convection flow of micropolar fluid past a vertical moving porous plate through porous medium with viscous dissipation. *Int. J. Appl. Math. Mech*, 2013, *9*(6), pp.48-67.

12.   M.K. Nayak, G.C. Dash, and L.P. Singh, Unsteady radiative MHD free convective flow and mass transfer of a viscoelastic fluid past an inclined porous plate. *Arabian Journal for Science and Engineering*, 2015, *40*, pp.3029-3039.

13.   B.P. Reddy, Mass transfer effects on an unsteady MHD free convective flow of an incompressible viscous dissipative fluid past an infinite vertical porous plate. *International Journal of Applied Mechanics and Engineering*, 2016, *21*(1), pp.143-155.

14.   S. Agarwalla, and N. Ahmed, MHD mass transfer flow past an inclined plate with variable temperature and plate velocity embedded in a porous medium. *Heat Transfer—Asian Research*, 2018, *47*(1), pp.27-41.

15.   B.K. Swain, and R.N. Barik, Mass Transfer Effects on Mixed Convective MHD Flow of Second Grade Fluid Past a Vertical Infinite Plate with Viscous Dissipation and Joule Heating. *Journal of Institute of Science and Technology*, 2022, *27*(1), pp.51-67.

16.   R. Kandasamy, T. Hayat, S. Obaidat, Group theory trans-formation for Soret and Dufour effects on free convective heat and mass transfer with thermophoresis and chemical reaction over a porous stretching surface in the presence of heat source/sink. *Nucl. Eng. Des*. 2011, 241(6), pp.1607-1619.

17.   E.M.A. Elbashbeshy, and A.M. Sedki, Effect of chemical reaction on mass transfer over a stretching surface embedded in a porous medium. *Int. J. of computational Engineering Research*, 2014, *4*(2), pp.20-28.

18.   N.S. Rosly, N. Ahmad, S. Ahmad, and N. Ramli, Stability analysis of mass transfer effects on the unsteady stagnation-point flow past a permeable sheet. *ESTEEM Academic Journal*, 2023, *19*, pp.145-157.

19.   H.S. Takhar, A.J. Chamkha, and G. Nath, Flow and mass transfer on a stretching sheet with a magnetic field and chemically reactive species. *International Journal of Engineering Science*, 2000, *38*(12), pp.1303-1314.

20.   A.A. Afify, MHD free convective flow and mass transfer over a stretching sheet with chemical reaction. *Heat and Mass Transfer*, 2004, *40*(6-7), pp.495-500.

21.   K. Bhattacharyya, S. Mukhopadhyay, and G.C. Layek, Unsteady MHD boundary layer flow with diffusion and first-order chemical reaction over a permeable stretching sheet with suction or blowing. *Chemical engineering communications*, 2013, *200*(3), pp.379-397.

22.   A.Majeed, A. Zeeshan, R. Ellahi, Chemical reaction and heat transfer on boundary layer Maxwell Ferro-fluid flow under magnetic dipole with Soret and suction effects. *Engineering Science and Technology, An International Journal*, 2017, 20(3), pp.1122-1128.

23.   P. Ganesan, and G. Palani, Finite difference analysis of unsteady natural convection MHD flow past an inclined plate with variable surface heat and mass flux. *International journal of heat and mass transfer*, 2004, *47*(19-20), pp.4449-4457.

24.   R. Saravana, S. Sreekanth, S. Sreenadh, and R.H. Reddy, Mass transfer effects on MHD viscous flow past an impulsively started infinite vertical plate with constant mass flux. *Advances in Applied Science Research*, 2011, *2*(1), pp.221-229.

25.   P. Loganathan, and C. Sivapoornapriya, Viscous dissipation effects on unsteady natural convective flow past an infinite vertical plate with uniform heat and mass flux. *Wseas Transactions on Heat and Mass Transfer*, 2014, *9*, pp.63-73.

26.   F.M. Abbasi, S.A. Shehzad, T. Hayat, A. Alsaedi, and M.A. Obid, Influence of heat and mass flux conditions in hydromagnetic flow of Jeffrey nanofluid. *AIP Advances*, 2015, *5*(3), 037111.

27.   S. Das, R.N. Jana, and A.J. Chamkha, Unsteady free convection flow past a vertical plate with heat and mass fluxes in the presence of thermal radiation. *Journal of Applied Fluid Mechanics*, 2015, *8*(4), pp.845-854.

28.   S. Ghosh, and S. Mukhopadhyay, Flow and heat transfer of nanofluid over an exponentially shrinking porous sheet with heat and mass fluxes. *Propulsion and Power Research*, 2018, *7*(3), pp.268-275.

29.   K. Saritha, and P. Palaniammal, MHD viscous Cassonfluid flow in the presence of a temperature gradient dependent heat sink with prescribed heat and mass flux. *Frontiers in Heat and Mass Transfer (FHMT)*, 2018, *10.*

30.   S. Sharidan, T. Mahmood, and I. Pop, Similarity solutions for the unsteady boundary layer flow and heat transfer due to a stretching sheet, *Int. J. Appl. Mech. Eng.*, 2006, 11, 647–654.

31.   A.J. Chamkha, A.M. Aly, and M.A. Mansour, Similarity solution for unsteady heat and mass transfer from a stretching surface embedded in a porous medium with suction=injection and chemical reaction effects, Chem. Eng. Commun., 2010, 197, 846–858.

Information about authors:

Rakesh Kr Saha – M.Sc , Research scholar of Department of Mathematics, The University of Burdwan, (Burdwan-713104, West Bengal, India);

Hiranmoy Maiti – M.Sc, Research scholar of Department of Mathematics, The University of Burdwan, (Burdwan-713104, West Bengal, India);

Swati Mukhopadhyay – (corresponding author), Doctor of science, Professor of Department of Mathematics, The University of Burdwan, (Burdwan-713104, West Bengal, India, e-mail: swati_bumath@yahoo.co.in).

L.A. Alexeyeva ⓘⒹ

Institute of Mathematics and Mathematical Modeling of
Ministry of Science and Higher Education of the Republic of Kazakhstan, Almaty, Kazakhstan
e-mail: alexeeva@math.kz

Ether as an electro-gravimagnetic field, its density and properties

Abstract. Based on biquaternion wave (*biwave*) equations, a biquaternionic model of the ether is developed – an electro-gravimagnetic field, the state of which is described by the biquaternion of the strength of EGM field. Its complex scalar part determines the density of the ether, and the complex vector part characterizes the strength of the electric and gravimagnetic fields. The biquaternion gradient of the ether biquaternion determines the biquaternion of EGM charge-current, which contains in the scalar part the electric charge and gravitational mass, and the vector part is formed by electric and gravimagnetic currents. Special cases of these biwave equations are the biquaternionic representation of the Maxwell and Dirac equations.

Representations of biquaternion of photons and elementary atoms are obtained as partial stationary solutions of biwave equations with a fixed oscillation frequency. The presence of a gravitational component of the EGM field of the photon is shown, which explains the light pressure. Using the biquaternion model of the atom, a periodic system of atoms is constructed based on the structure of a simple musical scale.

A field analogue of Newton's second law is presented as a biquaternion generalization of the Dirac system of equations. It describes the transformation of the EGM charge-current biquaternion under the influence of an external EGM field. It contains, in addition to all known physical forces, a number of new forces that are proposed for discussion and experimental verification.

The biquaternion representation of Newton's third law of action and reaction in the scalar part is a well-known analogue of Betti's law on the power of forces acting on EGM charges and currents.

Key words: biquaternion wave, electro-gravimagnetic field, Betti's law, complex vector, bigradients.

Introduction

Modern Newtonian mechanics is based on the three basic laws formulated by Newton for a material point. Based on these laws, the equations of motion of systems of material points, a rigid body, and mechanics of continuous media were constructed. However, real material bodies are not material points, but consist of distributed masses, characterized by gravitational density, electric charge, which move (the state of rest is always only relative). Is it possible to construct equations of state for a continuous medium without initially using the material point model, which requires discretization of a continuous medium to construct its equations of motion?

The Poisson equation is indicative here, the solutions of which describe the potentials of the gravitational or electric fields, if the densities of masses or electric charges are on the right side of the equation, respectively. Moreover, if they are moving? For moving electric charges and currents, the emerging electromagnetic fields describe Maxwell equations. In addition, what will be the gravitational fields of the moving masses – the question remains open to this day.

However, these questions have a positive answer, if we use a more complex mathematical apparatus to describe the motion of material media, which is the differential algebra of biquaternions [1-2]. Here, based on this algebra, the equations of motion of distributed masses and electric charges and the gravitational and electromagnetic fields generated by them are proposed. Equations for the interaction of charges and currents and energy relations characterizing the interaction energy are constructed.

By this the model is based on the same Newton laws of inertia, proportionality of force and accel-

eration, action and counter-action, only formulated in terms of biquaternion gradients (*bigradients*), generalizing the concept of a gradient to scalar-vector fields. The constructed equations are biquaternionic generalization of Maxwell equations (GME) and Dirac equations (GDE). The static GME solutions describe static gravitational and electric fields, the potentials of which satisfy the Poisson equation.

Those the proposed model includes the well-known classical equations of mathematical physics and field theory, which combines the gravitational field and the electromagnetic field into a single electro-gravimagnetic field. At the same time, biquaternionic field analogue of Newton second law, in addition to the known physical forces, contains new forces that are offered to the audience for discussion.

1. Biquaternions and bigradients

The foundations of differential algebra of biquaternions are presented by the author in [1-2]. Here we briefly give the basic concepts necessary to describe the biquaternionic model of EGM field. We introduce a complex space of quaternions $\mathrm{K} = \{\mathbf{F} = f + F\}$ (*f* are complex numbers: $f = f_1 + if_2$, and *F* is a three-dimensional vector with complex components: $F = F_1 + iF_2$). K is a linear space with the well-known operation of quaternionic multiplication ($\circ$):

$$\mathbf{F} \circ \mathbf{G} = (f + F) \circ (g + G) = \\ = (fg - (F,G)) + (fG + gF + [F,G]) \qquad (1)$$

which is noncommutative, but associative: $(\mathbf{F} \circ \mathbf{G}) \circ \mathbf{H} = \mathbf{F} \circ (\mathbf{G} \circ \mathbf{H})$. Further, we use *mutual bigradients*. These are differential operators of the form

$$\nabla^{\pm}\mathbf{F} = (\partial_{\tau} \pm i\nabla) \circ (f + F) = \\ (\partial_{\tau} f \mp i\, divF) \pm \partial_{\tau} F \pm i\,\mathrm{grad}\, f \pm i\,\mathrm{rot}\, F \qquad (2)$$

Their composition gives the wave operator:

$$\nabla^{-}\left(\nabla^{+}\mathbf{K}\right) = \nabla^{+}\left(\nabla^{-}\mathbf{K}\right) = \frac{\partial^2 \mathbf{K}}{\partial \tau^2} - \Delta\mathbf{K} \triangleq \Box\mathbf{K}. \qquad (3)$$

It is convenient to use this property when solving biquaternionic wave (*biwave*) equations:

$$\nabla^{\pm}\mathbf{B} = \mathbf{G}(\tau, x) \qquad (4)$$

An example of such an equation is the system of Maxwell equations, which is reduced to the biwave equation (4) (with the sign +).

2. Biquaternions of the electro-gravimagnetic field. Either equation

Let consider in the Minkowski space $(\tau, x) = \{\tau = ct, x_1, x_2, x_3\}$ the EGM-field generated by distributed electric charges and masses and their currents. To describe it, the following biquaternions (*Bq*) is introduced:

$$\textit{either}\ \mathrm{Bq}\qquad \mathbf{A}(\tau,x) = i\alpha + A, \quad \alpha = \alpha_1 + i\alpha_2, \\ A = E + iH \qquad (5)$$

where a scalar part $\alpha(\tau, x)$ is named *either density*, *E* and *H* are tensions of electric and *gravimagnetic* fields (a potential part *H* corresponds to a strength of gravitational field, and its vortex component corresponds to a strength of magnetic field *B*:

$$H = G + B,\ rot\ G = 0,\ div\ B = 0. \qquad (6)$$

Also we determine

charge-current Bq

$$\mathbf{\Theta}(\tau,x) = i\rho + J, \quad \begin{array}{l} \rho = -\rho^E + i\rho^H, \\ J = -J^E + iJ^H \end{array} \qquad (7)$$

Here $\rho^E(\tau, x)$ and $\rho^H(\tau, x)$ are densities of electric charge and gravitational mass, $J^E(\tau, x)$, $J^H(\tau, x)$ are the density of electric and gravimagnetic currents.

It has the form of the biwave equation –

either equation $\nabla^{+}\mathbf{A} = \mathbf{\Theta}(\tau, x)\ \Leftrightarrow$ (8)

$$\partial_{\tau}\alpha - div\ A = \rho, \quad \partial_{\tau}A + i\,\mathrm{rot}\, A = J\ \Leftrightarrow (9)$$

$$\begin{cases} \operatorname{rot} H = \partial_\tau E + J^E, & \operatorname{rot} E = -\partial_\tau H + J^H \\ \rho^E = \partial_\tau \alpha_2 + \operatorname{div} E, & \rho^H = \partial_\tau \alpha_1 - \operatorname{div} H \end{cases} \quad (10)$$

When

$$\alpha = 0, \ \operatorname{div} H = 0, J^H = 0, \quad (11)$$

the Eqs (10) coincide with Maxwell equations. From (8) it follows that the charges-currents are *physical manifestation of bigradient of EGM-field.*

Energy density and Poynting vector of EM field are generalized into the *energy-momentum* biquaternion of EGM field

$$\mathbf{\Xi} = \frac{1}{2}\mathbf{A}^* \circ \mathbf{A} = W_\mathbf{A} + iP_\mathbf{A}, \quad \mathbf{A}^* = -i\overline{\alpha} - \overline{A},$$

$$W_\mathbf{A} = 0,5\left(|\alpha|^2 + \|A\|^2\right), \quad (12)$$

$$P_\mathbf{A} = -\operatorname{Re}(\alpha\overline{A}) + [\operatorname{Re}(A), \operatorname{Im}(A)]$$

Here $W_\mathbf{A}$ is energy density, $P_\mathbf{A}$ is the Poynting vector, which characterizes the direction of energy propagation in the EGM medium. Both of these values are valid.

The mutual bigradient from Eq (8) gives the wave equation for EGM tension:

$$\Box\mathbf{A} = \nabla^-\mathbf{\Theta}(\tau, x)J \implies$$
$$\Box\alpha = \partial_\tau\rho + \operatorname{div} J, \quad (13)$$
$$\Box A = \nabla\rho + \partial_\tau J - i\operatorname{rot} J$$

Whence it follows that electric, magnetic and gravitational waves propagate at the light speed.

The biquaternion of the energy-momentum of EGM charges-currents is

$$\mathbf{\Xi}_\mathbf{\Theta} = 0,5\mathbf{\Theta} \circ \mathbf{\Theta}^* = -(i\rho + J) \circ (i\overline{\rho} + \overline{J}) =$$
$$= 0,5\left(|\rho|^2 + \|J\|^2\right) - \quad (14)$$
$$-i\left\{\operatorname{Re}\left(\rho\overline{J}\right) - i\left[\operatorname{Re} J, \operatorname{Im} J\right]\right\} = W_\mathbf{\Theta} + iP_\mathbf{\Theta}$$

Here $W_\mathbf{\Theta}$ characterizes the energy density of EGM charges-currents, and Poynting vector $P_\mathbf{\Theta}$ determines the direction of propagation of this energy.

EXAMPLE 1. Let consider photons as some solutions of A-field Eq (8).

Definition. We call a photon an *elementary,* generated by a concentrated EGM charge of the form: $\mathbf{\Theta}(\mathbf{x}, \tau) = i\delta(\mathbf{x})\ e^{-i\omega\tau}$.

Its has the biquaternionic representation

$$\mathbf{\Phi}^0(\mathbf{x}, \tau) = \frac{e^{i\omega(r-\tau)}}{4\pi r}\left\{\omega + \mathbf{e_x}\left(i\omega + \frac{1}{r}\right)\right\},$$

$$\mathbf{e_x} = \mathbf{x}/r, \quad r = \|\mathbf{x}\|.$$

Its energy-momentum

$$\mathbf{\Xi}_\Phi^0(\mathbf{x}, \omega) = \frac{1}{\pi r^2}\left\{\omega^2 + \frac{1}{2r^2} + i\omega^2\mathbf{e_x}\right\}.$$

Note that scalar part $\mathbf{\Phi}^0(\mathbf{x}, \tau)$ is equal to

$$\frac{\omega}{4\pi r}e^{i\omega(r-\tau)} =$$

$$= \frac{\omega}{4\pi r}\left(\cos\omega(r-\tau) + i\sin\omega(r-\tau)\right)$$

Here the real part determines the density of the electric field of the photon, the imaginary part is the density of the gravimagnetic field of the photon. And the imaginary part $\mathbf{\Phi}^0(\mathbf{x}, \tau)$ is a gravimagnetic wave that generates light pressure.

For the construction of biquaternions of photons and light, see [13, 14].

3. Third Newton law of charge-current interaction

Let's consider two EGM-fields $\mathbf{A}$ and $\mathbf{A}'$, generated by charges-currents $\mathbf{\Theta}, \mathbf{\Theta}'$. We introduced a biquaternion of power – density of the forces acting from the field $\mathbf{A}'$ on the charges-currents $\mathbf{\Theta}(\tau, x)$ of the field $\mathbf{A}$ in form

$$\mathbf{F} = f + iF = \mathbf{A}' \circ \mathbf{\Theta} =$$
$$= -(\rho\alpha' + (A', J)) + i\{\alpha'J + \rho A' - i[A', J]\} \quad (15)$$

Its scalar part has the form of a power of acting forces:

$$f = -(A',J) - \rho\alpha' = (E',J^E) + (H',J^H) + \\ + i(H',J^E) - i(E',J^H) - \rho\alpha' \triangleq M$$, (16)

and the vector part contains all known forces and not only

$$F = \alpha'J + \rho A' - i[A',J] \quad \Rightarrow$$

$$\mathrm{Re}(F) = -\rho^E E' - \rho^H H' + [E',J^H] - \\ -[H',J^E] + \mathrm{Re}(\alpha'J) = -\rho^E E' - \rho^H G' + [J^E,B'] - \\ -\left\{ \rho^H B' + [G',J^E] - [E',J^H] + \mathrm{Re}(\alpha'J) \right\}$$ (17)

$$\mathrm{Im}(F) = \\ = \left\{ \rho^H E' - \rho^E H' + [E',J^E] + [H',J^H] + \mathrm{Im}(\alpha'J) \right\}$$

Indeed, in $\mathrm{Re}(F)$ on the right there are known forces: the Coulomb force of electric action $\rho^E E'$, in vortex part of the vector H' there is the Lorentz force $B' \times J^E$, in the potential part of the vector H' there is a gravitational force $\rho^H G'$.

Also you see here on the right the unknown forces (in curly brackets) : *electromass* force $E' \times J^H$ of electric field impact on mass currents; *gravimagnetic* force $\rho^H B'$ of influence of magnetic field on mass; *gravielectric* force $[G',J^E]$ of gravity action on electric currents. These forces, $\alpha'J$ and ones in $\mathrm{Im}(F)$ are *the new forces*.

Similarly, we introduce the power-force biquaternion of acting from the A-field on the charges-currents of the A'-field:

$$\mathbf{F}' = f' + iF' = \mathbf{A} \circ \mathbf{\Theta}'.$$

According to third Newton law on action and counteraction we postulate
The law for EGM action-contraction:

$$\mathbf{F}' = -\mathbf{F} \iff \mathbf{A}' \circ \mathbf{\Theta} = -\mathbf{A} \circ \mathbf{\Theta}' \qquad (18)$$

We name Eq (16) as *third Newton law for EGM charges-currents*.

4. Newton's second law and interaction equations.

By analogue of second Newton law we postulate
The law for EGM charges-currents interaction

$$\kappa \ \nabla^- \circ \mathbf{\Theta} = \mathbf{F}, \quad \kappa \ \nabla^- \circ \mathbf{\Theta}' = \mathbf{A} \circ \mathbf{\Theta}' \quad (19)$$

Here the interaction constant κ is like to gravitational constants. Together with biwave equations for EGM fields:

$$\nabla^+ \circ \mathbf{A} = \mathbf{\Theta}, \quad \nabla^+ \circ \mathbf{A}' = \mathbf{\Theta}', \qquad (20)$$

and the third Newton law (16), they give a closed system of nonlinear differential equations for $\{\mathbf{\Theta}, \mathbf{A}\}, \{\mathbf{\Theta}', \mathbf{A}'\}$ determination.

The introduction of a constant κ is related to dimension. The dimension $\mathbf{A}$ is denoted by $[\mathbf{A}] = \alpha$ (energy density), $[x] = l$ (length), then $[\mathbf{\Theta}] = \alpha l^{-1}$, $[\kappa] = \alpha l$. Let's call κ the *radiation constant*, because its dimension determines the density of the energy flux through the surface.

Expanding the scalar and vector parts of (18), we obtain
EGM field charge-current transformation equations

$$i\kappa \left(\partial_\tau \rho + div J \right) = -(A',J) - \rho\alpha' = M \quad (21)$$

$$\kappa \left(\partial_\tau J - i rot J + \nabla\rho \right) = \\ = iF = i\alpha'J + i\rho A' + [A',J] \qquad (22)$$

под воздействием внешнего ЭГМ-поля $\mathbf{A}'$.

It follows from (19) that charge conservation law changes when the charges-currents interact under the influence of the *EGM* fields generated by them. A nonzero right-hand side appears in the equation, associated with the power *M* of the forces of action from another field, which is naturally observed in open systems. From scalar part of (20) we obtain
The law of conservation of electric charge and gravitational mass:

$$\kappa \left(\partial_\tau \rho^E + div\, J^E \right) =$$
$$= -(H', J^E) - (E', j^H) - Im(\rho \alpha') \quad (23)$$
$$\kappa \left(\partial_\tau \rho^H + div\, J^H \right) =$$
$$= -(H', j^H) + (E', J^E) + Re(\rho \alpha')$$

As you can see, the power of the electric and gravimagnetic forces of the second field affects the mass and mass currents of the first.

The imaginary part of the vector equation (20) gives the equations of motion of gravimagnetic currents:

Field analogue of Newton's second law

$$\kappa \left(\partial_\tau J^H - rot J^E + \nabla \rho^H \right) =$$
$$= \rho^E E' - \rho^H H' + [E', J^H] + \quad (24)$$
$$+ [H', J^E] + Re\left(\alpha' J \right)$$

where the analogue of momentum is the density of gravimagnetic currents J^H. The real part of Eq (20) gives

Equations of motion of electric currents

$$\kappa \left(\partial_\tau J^E + irot J^H + \nabla \rho^E \right) =$$
$$= -\rho^H E' - \rho^E H' + [E', J^E] - \quad (25)$$
$$- [H', J^H] - Im\left(\alpha' J \right)$$

It describes the effect of an external field on electric currents. Its analog in modern physics is unknown to the author.

If the external EGM field is much more powerful than the intrinsic field of charge-currents, then its change can be ignored. Then we have a linear system of biquaternionic equations for determining the transformation of masses, charges and their currents under its influence, which we name the

Charge-currents transformation equation

$$\nabla^- \circ \mathbf{\Theta} = \kappa^{-1} \mathbf{A}' \circ \mathbf{\Theta} \quad (26)$$

where the biquaternion $\mathbf{A}'$ of the external EGM field is known.

From (26) by use (8) and (18) we get

$$\Box \mathbf{A} - \kappa^{-1} \mathbf{A} \circ \mathbf{\Theta}' = \mathbf{0}, \quad (27)$$

$$\Box \mathbf{\Theta} + \kappa^{-1} \nabla^+ \left(\mathbf{A}' \circ \mathbf{\Theta} \right) = \mathbf{0}, \quad (28)$$

Eqs (26) and (27) are the biquaterninic generalization of Dirac and Klein-Gordon equations.

6. The first Newton law for EGM field. The law of inertia

For free charge-currents $\mathbf{F} = 0$. Hence, from second Newton law for EGM of charge-currents, we obtain

The law of inertia

$$\nabla^- \mathbf{\Theta} = 0 \quad \leftrightarrow \quad (29)$$

$$\partial_\tau \rho + div\, J = 0, \quad grad\, \rho + \partial_\tau J - irot J = 0 \quad (30)$$

The first scalar equation is the mass-charge conservation law, which naturally must be satisfied in closed systems. The second vector equation defines the free motion (*inertia*) of electric and gravimagnetic currents in the absence of external influences, which is completely due to the inhomogeneity of the state associated with the presence of gradients and rotors of these fields. Separating the real and imaginary parts from (29) we get

First Newton law for mass charges and EGM field curents:

$$\partial_\tau J^E - rot\, J^H + grad\, \rho^E = 0,$$
$$\partial_\tau \rho^E + div\, J^E = 0;$$
$$\partial_\tau J^H + rot\, J^E + grad\, \rho^H = 0, \quad (31)$$
$$\partial_\tau \rho^H + div\, J^H = 0$$

These equations give a closed system of equations for determining the charges and currents of the A-field in the absence of external fields.

Solutions of equation (27) can be used for biquaternionic representations of elementary particles. In particular, the author used monochromatic solutions of equation (27) to construct harmonic bosons and leptons [11].

EXAMPLE 2. By use harmonic bosons, a periodic system of elementary atoms has been presented, constructed on the principle of a simple musical scale [12]:

Simple gamut							
do	*re*	*mi*	*fa*	*sol*	*la*	*si*	*do*
ω	$9\omega/8$	$5\omega/4$	$4\omega/3$	$3\omega/2$	$5\omega/3$	$15\omega/8$	2ω

Periodic table of elementary atoms						
1	2	3	4	5	6	7
$\omega_1 = \omega$	$9\omega/8$	$5\omega/4$	$4\omega/3$	$3\omega/2$	$5\omega/3$	$15\omega/8$
$\omega_2 = 2\omega_1$	$9\omega_2/8$	$5\omega_2/4$	$4\omega_2/3$	$3\omega_2/2$	$5\omega_2/3$	$15\omega_2/8$
$\omega_3 = 2\omega_2$	$9\omega_3/8$	$5\omega_3/4$	$4\omega_3/3$	$3\omega_3/2$	$5\omega_3/3$	$15\omega_3/8$
...	...	...	...	...	...	...
$\omega_n = 2\omega_{n-1}$	$9\omega_n/8$	$5\omega_n/4$	$4\omega_n/3$	$3\omega_n/2$	$5\omega_n/3$	$15\omega_n/8$
...	...	...	...	...	...	...

The elementary atom in this periodic system has the form:

$$\mathbf{At}^{n,k}(t,x) = \frac{1}{r}e^{-iw_{n,k}t/c}\left\{\sin\left(w_{nk}r/c\right) + \left(\cos\left(w_{nk}r/c\right) - c\frac{\sin\left(w_{nk}r/c\right)}{w_{nk}r}\right)e_{\mathbf{x}}\right\}.$$

where the oscillation frequency $w_{nk} = 2^{n-1}\gamma_k w_{H_0}$ of the element in k-column of n-row of the periodic table , γ_k is the multiplier in k-column, w_{H_0} is the oscillation frequency of elementary hydrogen atom $\mathbf{At}^{1,1}(H_0)$.

Conclusion

We introduced postulates for EGM-field on the base of generalization of biquaternionic form of Maxwell and Dirac equations and obtained closed hyperbolic system which connect EGM-field, charges and currents in united system of equations. For this we enter new scalar α -field which is the either density. It characterizes an attraction-resistance properties of the either. That gives possibility to explain some physical phenomena which are observed in practice. In particular, the solutions of EGM-field describe electric and gravimagnetic waves which, in general case, are not transversal and have longitudinal component. Longitudinal EM-waves are observed in practice but classic electrodynamics doesn't explain there existence. Many interesting physical properties of this model appear by interaction of different system of charges and currents and their EGM-fields. Some of them were described in papers [1-3].

References

1. Алексеева Л.А. *Уравнения взаимодействия А-полей и законы Ньютона* (Известия НАН РК. Серия физико-математическая, №3, 2004, с.45-53

2. Alexeyeva L.A. *Newton's laws for a biquaternionic model of the electro-gravimagnetic fields, charges, currents, and their interactions* (Journal of Physical Mathematics, no1, 2009), Article ID S090604, 16pp.

3. Алексеева Л.А. *Полевые аналоги законов Ньютона для одной модели электро-гравимагнитного поля* (Гиперком-плексные числа в геометрии и физике, № 1,6, 2009),- С.122-134.

4. Алексеева Л.А. *Дифференциальная алгебра бикватернионов* (Математический журнал, № 4, 10, 2010), сс. 5-13; (Математический журнал, № 1, 11, 2011),33-41.

5. Alexeyeva L.A. *Biquaternions algebra and its applications by solving of some theoretical physics equations* (Clifford Analysis, Clifford algebras and applications, no 1, 7, 2012), pp.19-39.

6. Алексеева Л.А. *Уравнение трансформации и его обобщенные решения в дифференциальной алгебре бивакватернионов* (Доклады НАН РК, №4, 2013), сс.12-19.

7. Alexeyeva L.A. *Differential Algebra of Biquaternions. Dirac Equation and Its Generalized Solutions* (Progress in Analysis. Proceedings of the 8th Congress of the ISAAC, Moscow, 22-27 August 2013), pp.153-161.

8. Alexeyeva L.A. *Maxwell equations, their hamiltonian and biquaternionic forms and properties of their solutions* (Mathematical journal, 2016), pp.25-39.

9. Alexeyeva L.A. *Biquaternionic model of electro-gravimagnetic field, charges and currents. Law of inertia* (Journal of modern physics, no 7, 2016), pp.435-444, http://dx.doi.org/ 10.4236/jmp.2016.75045.

10. Alexeyeva L.A Biquaternionic form of laws of Electro-Gravimagnetic Charges and Currents interactions //*Journal of Modern Physics*, 7(2016), 1351-1358. http://dx.doi.org/10.4236/jmp.2016.711121

11. Alexeyeva L.A. *Periodic system of atoms as simple gamma in biquaternionic representation* (Scientific federation. 2nd International conference on Quantum Mechanics and Nuclear Engineering. Keynote forum, Paris, 23-24 September 2019), p. 56.

12. Alexeyeva L.A. *Biquaternionic model of electro-gravimagnetic fields an interactions* // (Scientific federation. 2nd Global summit on physics. Plenary forum. Paris, 26-27 September 2019), p. 19.

13. Алексеева Л.А. *Бикватернионы фотонов. Свет* (Журнал проблем эволюции открытых систем, Вып.22 , Т.1, 20200, с.75-82.

14. Alexeyeva L.A. *Ether and photons in biquaternionic presentation* (SSRG-IJAP, Int. Journal of Applied Physics, vol. 7, Issue 1, 2020), p. 1-7.

Information about authors:

Lyudmila A.Alexeyeva – Doctor of science, professor of Institute of Mathematics and Mathematical Modeling, (Almaty, Kazakhstan, e-mail: alexeeva@math.kz).

Lazhar Bougoffa

Imam Mohammad Ibn Saud Islamic University (IMSIU), Riyadh, Saudi Arabia
e-mail: lbbougoffa@imamu.edu.sa

A new transform for solving linear second-orders ODE with variable coefficients

Abstract: In this paper, we present a novel symmetry-enhanced transform

$$\mathcal{L}(f(x); a) = \int_{-\infty}^{+\infty} e^{-ax^2} f(x)dx = \mathcal{B}(a), a > 0$$

to evaluate Gaussian integrals commonly used in mathematical and physical domains, particularly in quantum field theory. Additionally, we utilize this original transformation methodology to solve a wide range of second-order linear ordinary differential equations (ODEs) that have variable coefficients, which is a common occurrence in physics. Notable examples encompass Weber, Euler-Cauchy, and Bessel equations, highlighting the broad applicability of our proposed method. Diverging from established transforms like the widely used Laplace transform, our innovative approach introduces a symmetrical model, offering a distinct and founding perspective to the field.

Key words: New integral transform; Gaussian integral; Equation of free oscillations; Weber's equation; Euler-Cauchy Equation; Bessel's equation.

1 Introduction

Recently, Bougoffa and Rach proved the following formula [1]

Lemma 1

$$\int_{-\infty}^{\infty} e^{-ax^2} f(x)dx = \sqrt{\frac{\pi}{a}} \sum_{n=0}^{\infty} \frac{f^{(2n)}(0)}{(4a)^n n!}, a > 0 \quad (1.1)$$

provided that the function f is infinitely differentiable in $\mathbb{R}$ and, in a neighborhood of $x = 0$, it equals its Maclaurin series expansion about x. Here we must assume that f is such that the integral in the left hand side of (1.1) exists (that is, has some finite value). This assumption is usually satisfied in applications. We shall discuss this in section 2.

This formula has obtained by a new combination with the Adomian decomposition method [2, 3] and the explicit solution

$$u(x, t) = \frac{1}{\sqrt{4k\pi t}} \int_{-\infty}^{\infty} f(\xi) e^{-\frac{(\xi - x)^2}{4kt}} d\xi,$$

$$-\infty < x < \infty, t > 0$$

(1.2) of the initial – value problem for the heat equation

$$\frac{\partial u}{\partial t} = k \frac{\partial^2 u}{\partial x^2}, k > 0, t \geq 0, u(x, 0) = f(x). \quad (1.3)$$

This is a new helpful tool in calculating the Gaussian integrals [4] as a convenient convergent series.

Indeed, if we substitute $f(x) = 1$ into (1.1), then we obtain

$$\int_{-\infty}^{\infty} e^{-ax^2} dx = \sqrt{\frac{\pi}{a}}, a > 0. \quad (1.4)$$

The alternatives of the Gaussian integral can be derived from (1.1). For example, the evaluation of

$$\int_{-\infty}^{\infty} e^{-ax^2} x^{2n} dx = \frac{\sqrt{\pi}(2n)!}{4^n a^{n+\frac{1}{2}} n!} \quad (1.5)$$

is obtained by letting $f(x) = x^{2n}, n \geq 0$ into (1.1). It can be checked easily that different definite integrals of the above Gaussian form can be derived from formula (1.1).

1- The evaluation of the well-known integral: $\int_0^{\infty} \frac{e^{-a^2(1+x^2)}}{1+x^2} dx = \frac{\pi}{2} \mathrm{erf}(ca)$ can be evaluated directly from (1.1) by letting $f(x) = \frac{1}{x^2+1}$ with

$f(0) = 1, f''(0) = -2!, f^{(4)}(0) = 4!$. A simple substitution leads to

2-
$$\int_{-\infty}^{\infty} \frac{e^{-a^2 x^2}}{1+x^2} dx = \frac{\sqrt{\pi}}{a}\left[1 + \sum_{n=1}^{\infty} \frac{(-1)^n (2n)!}{4^n a^{2n} n!}\right]. \quad (1.6)$$

Since $\frac{(2n)!}{n!} = 2^n \left(1 \cdot 3 \cdot 5 \cdots (2n-1)\right)$. Hence

$$\int_{-\infty}^{\infty} \frac{e^{-a^2 x^2}}{1+x^2} dx = \frac{\sqrt{\pi}}{a}\left[1 + \sum_{n=1}^{\infty} (-1)^n \frac{1 \cdot 3 \cdot 5 \cdots (2n-1)}{(2a^2)^n}\right]. \quad (1.7)$$

Using the asymptotic expansion of the complementary error function

$$\text{erfc}(x) = \frac{e^{-x^2}}{\sqrt{\pi}x}\left[1 + \sum_{n=1}^{\infty} (-1)^n \frac{1 \cdot 3 \cdot 5 \cdots (2n-1)}{(2x^2)^n}\right], \quad (1.8)$$

we obtain

$$\int_{-\infty}^{\infty} \frac{e^{-a^2(1+x^2)}}{1+x^2} dx = \pi \, \text{erfc}(a). \quad (1.9)$$

3- The Dawson's integral [5, 6]:

This integral $\int_{-\infty}^{\infty} D(x)\, dx$ is called the Dawson's integral, where $D(x) = e^{-x^2} \int_0^x e^{t^2}\, dt$ and it arises in computation of the Voigt lineshape in heat conduction and in the theory of electrical oscillations in certain special vacuum tubes. It can be derived from formula (1.1) that

$$\int_{-\infty}^{\infty} D(x)\, dx = \int_{-\infty}^{\infty} e^{-x^2} \left[\int_0^x e^{t^2}\, dt\right] dx = 0. \quad (1.10)$$

4- The plasma dispersion function [7]:

The plasma dispersion function when the imaginary component of ξ is equal to zero and is defined as $Z(\xi) = \frac{1}{\sqrt{\pi}} \int_{-\infty}^{\infty} \frac{e^{-x^2}}{x-\xi} dx$.

An immediate consequence of this is

$$Z(\xi) = -\sum_{n=0}^{\infty} \frac{(2n)!}{4^n n!} \frac{1}{\xi^{2n+1}} =$$
$$= -\frac{1}{\xi}\left(1 + \frac{1}{2}\frac{1}{\xi^2} + \frac{3}{4}\frac{1}{\xi^4} + \frac{15}{8}\frac{1}{\xi^6} + \cdots\right). \quad (1.11)$$

This follows simply by letting the following in (1.1)

$$f(x) = \frac{1}{x-\xi},$$

$$f^{(2n)}(0) = -(2n)!\,\xi^{-2n-1}, n \geq 1. \quad (1.12)$$

The reader will find in the Table 1 different definite integrals of the above forms which can be easily calculated by (1.1).

No.	$f(x)$	$\int_{-\infty}^{\infty} e^{-ax^2} f(x) dx, a > 0$
1	1	$\dfrac{\sqrt{\pi}}{\sqrt{a}}$
2	x^2	$\dfrac{\sqrt{\pi}}{2a\sqrt{a}}$
3	x^n, n is odd	0
4	x^4	$\dfrac{3\sqrt{\pi}}{4a^2\sqrt{a}}$
5	x^{2n}	$\dfrac{(2n)!\sqrt{\pi}}{4^n a^{n+\frac{1}{2}} n!}$
6	$\dfrac{x^2}{x^2+b^2}$	$\dfrac{\sqrt{\pi}}{\sqrt{a}} - \pi b e^{ab}(1 - \text{erf}(\sqrt{ab}))$
7	$\dfrac{1}{x^2+b^2}$	$\dfrac{\sqrt{\pi}}{b} e^{ab}(1 - \text{erf}(\sqrt{ab}))$
8	$\cos rx$	$\dfrac{\sqrt{\pi}}{\sqrt{a}} e^{-\frac{r^2}{4a}}$
9	$e^{\pm rx}$	$\dfrac{\sqrt{\pi}}{\sqrt{a}} e^{\frac{r^2}{4a}}$

No.	$f(x)$	$\int_{-\infty}^{\infty} e^{-ax^2} f(x)dx, a > 0$
10	xe^{-2rx}	$\dfrac{r}{a}\dfrac{\sqrt{\pi}}{\sqrt{a}} e^{\frac{r^2}{a}}$
11	$x^2 e^{-2rx}$	$\dfrac{1}{2a}\dfrac{\sqrt{\pi}}{\sqrt{a}}(1 + \dfrac{2r^2}{a})e^{\frac{r^2}{a}}$
12	$e^{\frac{-r}{x^2}}$	$\dfrac{\sqrt{\pi}}{\sqrt{a}} e^{-2\sqrt{ra}}$

Table 1: **Some functions and their transforms** $\int_{-\infty}^{\infty} e^{-ax^2} f(x)dx, a > 0$.

Another important observation on some elementary integrals is

Lemma 2 Define the function F_n by

$$F_n(x) = \int_x^{\infty} t^n e^{-at^2} dt, a > 0. \quad (1.13)$$

Then F_n satisfies

$$\begin{cases} F_{2n}(x) + F_{2n}(-x) = \frac{\sqrt{\pi}(2n)!}{4^n a^{n+\frac{1}{2}}n!} \\ F_{2n+1}(x) + F_{2n+1}(-x) = 0. \end{cases} \quad (1.14)$$

Proof. Replacing x with $-x$, we obtain

$$F_n(-x) = \int_{-x}^{\infty} t^n e^{-at^2} dt, a > 0. \quad (1.15)$$

If we make the transformation $t \to -t$, we get $F_n(-x) = \int_{-\infty}^{x}(-1)^n t^n e^{-at^2} dt, a > 0$.

Thus,

$$F_{2n}(x) + F_{2n}(-x) = \int_{-\infty}^{\infty} t^{2n} e^{-at^2} dt. \quad (1.16)$$

Hence, from Table 1, we have

$$F_{2n}(x) + F_{2n}(-x) = \frac{\sqrt{\pi}(2n)!}{4^n a^{n+\frac{1}{2}}n!}. \quad (1.17)$$

We note that if we choose $n = 0$ *and* $a = \frac{1}{2}$, then $Q(x) + Q(-x) = 1$, where $Q(x) = \frac{1}{\sqrt{2\pi}}\int_x^{\infty} e^{-\frac{t^2}{2}} dt$ is the Q- function corresponds to the tail probability of standard normal distribution [8].

Similarly, we have $F_{2n+1}(x) + F_{2n+1}(-x) = 0$.

The following recurrence follows by integration by parts

Lemma 3 The function F_n satisfies the following recurrence

$$F_n(x) = \frac{n-1}{2a} F_{n-2}(x) + \frac{x^{n-1}}{2a} e^{-ax^2} \quad (1.18)$$

with

$$F_0(x) = \frac{\sqrt{\pi}}{2\sqrt{a}}\left(1 - \text{erfc}(\sqrt{a}x)\right) \text{ and}$$
$$F_1(x) = \frac{1}{2a} e^{-ax^2}. \quad (1.19)$$

Also, an alternative expression for F_{2n+1} can be obtained from the recurrence and mathematical induction

Lemma 4

$$\boldsymbol{F_{2n+1}(x) = \frac{n!}{2a^{n+1}} e^{-ax^2} \sum_{k=0}^{n} \frac{(\sqrt{a}x)^{2k}}{k!}}. \quad (1.20)$$

Many integral transforms of the familiar Laplace transform $\mathcal{L}(f; s) = \int_0^{\infty} e^{-sx} f(x)dx$ with kernel $k(s, x) = e^{-sx}$ are introduced such as the Laplace-Carson transform, which is defined by [9] $\mathcal{L}(f(x); p) = p \int_0^{+\infty} e^{-px} f(x)dx, p > 0$ and the so-called Sumudu transform: $\mathcal{F}(f(x); q) = \frac{1}{q}\int_0^{+\infty} e^{-\frac{1}{q}x} f(x)dx, q > 0$, which has been the subject of several papers. This integral transform is obtained from the Laplace-Carson transform by means of the trivial change of variable $\boldsymbol{p = \frac{1}{q}}$. All the properties demonstrated for the Sumudu transform may very readily be deduced from the corresponding properties for the standard Laplace transform. These integral transforms have been demonstrated to provide accurate and computable solutions for a wide class of linear differential equations. It is imperative to acknowledge that while

the Laplace transform is a powerful tool for solving certain differential equations, it is not universally applicable. Indeed, not all functions possess a Laplace transform, rendering it inadequate for certain classes of linear ordinary differential equations (ODEs). For in- stance, the function $f(x) = e^{x^2}$ does not have a Laplace transform, as the integral diverges for all values of s.

The transformation $\mathcal{L}(f(x); a)$ with its Properties 1-5 (Theorem 2) offers a powerful solution for tackling different linear ordinary differential equations. Among the equations are the Euler-Cauchy equation, Weber's equation [10], and associated Bessel's equation [11], etc. By converting them into more manageable forms, we can compute one solution with ease, and then the second independent solution can be deduced by the method of reduction of order to such equations. This approach is de- tailed after Section 3. This integral transform is also particularly significant in physics boundary value problems, as it can solve linear equations with initial and boundary conditions that the Laplace transform cannot handle. Therefore, our newly proposed integral transform presents a promising alter- native for addressing such equations.

The symmetry transformation technique involves simplifying the differential equation into a first-order linear differential equation, which can then be solved with ease through an inverse transform. Although this method is effective, it may sometimes yield a second-order ODE with variable coefficients. Hence, this approach is only successful under suitable conditions on the coefficients of the ODE.

To provide a comprehensive understanding of the meaning of this transformation in mathematical terms, we will present a detailed discussion of its integral transform definition, including its formula, properties, and practical applications. This will allow for a thorough exploration of its conceptual underpinnings and how it can be effectively utilized.

2 A new integral transform

We begin by stating the following definition:

Definition 1 *Let f be a function defined for all* $x \geq 0$. *Our new integral transform is the integral of* f *times* $e^{-ax^2}, a > 0$ *from* $-\infty$ *to* $+\infty$, *and is denoted by* $\mathcal{L}(f(x); a)$:

$$\mathcal{L}(f(x); a) = \int_{-\infty}^{+\infty} e^{-ax^2} f(x) dx, a > 0. \quad (2.1)$$

Here we must assume that f satisfies

$$|f(x)| \leq M e^{bx^2} \text{ for all } -\infty < x < +\infty, a > b, \quad (2.2)$$

where b and M are some constants, such that the integral exists. then
$\mathcal{L}(f(x); a)$ *is a function of a, say,* $B(a)$, *and*

$$\mathcal{L}(f(x); a) = \int_{-\infty}^{+\infty} e^{-ax^2} f(x) dx = \mathcal{B}(a), \quad (2.3)$$

$$a > 0.$$

Furthermore, if $f : \mathbb{R} \longrightarrow \mathbb{R}$ is infinitely differentiable and, in a neighborhood of $x = 0$, it equals its Maclaurin series expansion about x, *then*

$$\mathcal{B}(a) = \sqrt{\frac{\pi}{a}} \sum_{n=0}^{\infty} \frac{f^{(2n)}(0)}{(4a)^n n!}. \quad (2.4)$$

The given function f in (2.3) is called the inverse transform of $B(a), a > 0$ *and is denoted by* $\mathcal{L}^{-1}(B)$; *that is,* $f(x) = \mathcal{L}^{-1}(\mathcal{B}(a)), a > 0$ provided that $\mathcal{L}(f(x); a) \neq 0$.

In order to guarantee the convergence of the series $\sum_{n=0}^{\infty} \frac{f^{(2n)}(0)}{(4a)^n n!}$ for $a > 0$, we must assume that the higher order derivatives of $f(x)$ at $x = 0$ are bounded. We first note that, it may happen in certain cases that $\mathcal{L}(f(x); a)$ exists for a given function f, but $\mathcal{L}^{-1}(\mathcal{B}(a))$ is not uniquely determined. This can be seen from the example given in Table 1-No. 9: $\mathcal{L}(e^{\pm rx}; a) = \frac{\sqrt{\pi}}{\sqrt{a}} e^{\frac{r^2}{4a}}$, which shows that the inverse of this transform is not essentially unique. This is true in many situations in the application of this transform for solving second-order ODEs. It is a very convenient one, since it allows us to find two solutions. This can be seen from a simple example in Section 3.

Another observation that we need is that it can be easily checked that $\mathcal{L}(f(x); a)$ for any odd function, for example $f(x) = x^n, n = 1,3, \ldots$. In this case, a useful modified of this integral transform is given by

$$\mathcal{L}(f(x); a) = \int_0^{+\infty} e^{-ax^2} f(x) dx, a > 0. \quad (2.5)$$ In general, for any even or odd function, we may say that the inverse of a given transform is essentially unique. In particular, if two continuous functions have the same transform, they are completely identical, and in this case we could determine the function $f(x)$ from its transform $\mathcal{B}(a)$ provided that

it was possible to express $\mathcal{B}(a)$ in terms of simpler functions with known inverse transforms. Indeed, any odd or even function f can be determined from its transform $B(a)$ using the Mellin's Inversion Formula

$$g(t) = \mathcal{L}^{-1}(\mathcal{B}(a)) =$$

$$= \frac{1}{2\pi i} \lim_{T \to +\infty} \int_{\gamma-iT}^{\gamma+iT} e^{at} \mathcal{B}(a) da, t > 0, \qquad (2.6)$$

where γ is a positive constant and is greater than the real part of all singularities of $\mathcal{B}(a)$, and the function $g(t) = \frac{f(\sqrt{t})}{\sqrt{t}}$; can be done with the substitution $t = x^2$. We give an example to illustrate the application of this inversion. Let $\mathcal{B}(a) = \frac{1}{\sqrt{a}}$. Substituting into the Mellin's inversion formula, we find that

$$g(t) = \frac{1}{2\pi i} \lim_{T \to +\infty} \int_{\gamma-iT}^{\gamma+iT} e^{at} \frac{1}{\sqrt{a}} da =$$

$$= \frac{1}{\sqrt{\pi t}} \lim_{T \to +\infty} [\text{erf}(\sqrt{at})]_{\gamma-iT}^{\gamma+iT} = \frac{1}{\sqrt{\pi t}} \qquad (2.7)$$

Consequently, $f(x) = \frac{1}{\sqrt{\pi}}$.

We would now like to examine some examples of functions that do not have a Maclaurin expansion. The first example in this section reproduces a related integral to $\mathcal{L}(f(x); a)$.

Examples [12, 13]

1- $\int_{-\infty}^{+\infty} (e^{-a_1 x^2} - e^{-a_2 x^2}) \frac{1}{x^2} dx, a_1, a_2 > 0$.

This integral can be obtained by writing $(e^{-a_1 x^2} - e^{-a_1 x^2}) \frac{1}{x^2} = \int_{a_1}^{a_1} e^{-tx^2} dt$. Thus

2-
$$\int_{-\infty}^{+\infty} (e^{-a_1 x^2} - e^{-a_2 x^2}) \frac{1}{x^2} dx =$$
$$2\sqrt{\pi}(\sqrt{a_2} - \sqrt{a_1}).$$

3- $\mathcal{L}(e^{\frac{-b}{x^2}}; a) = \int_{-\infty}^{+\infty} e^{-ax^2} e^{\frac{-b}{x^2}} dx =$
$$\frac{\sqrt{\pi}}{\sqrt{a}} e^{-2\sqrt{ab}}, b > 0.$$

4- $\mathcal{L}\left(\ln x^2; a = \frac{1}{2\sigma^2}\right) = \sqrt{2\pi}\sigma$
$$(\ln \sigma^2 - \sigma - \ln 2).$$

5- $\int_{-\infty}^{+\infty} e^{-ax^2} [\int_{-x}^{+\infty} e^{-by^2}] dx =$

$$\frac{\pi}{2\sqrt{ab}}, a, b > 0.$$

We have

Theorem 1 *If f is defined and piecewise continuous on every finite inter-val on the $x-$axis and satisfies the condition (2.2). Then the new integral transform $\mathcal{L}(f(x); a)$ exists for $a > b$.*

Proof. Since f is piecewise continuous and $e^{-ax^2} f(x)$ is integrable over any finite interval on the $x-$axis

$$|\mathcal{L}(f(x); a)| =$$
$$= \left|\int_{-\infty}^{\infty} e^{-ax^2} f(x) dx\right| \le \int_{-\infty}^{\infty} e^{-ax^2} |f(x)| dx \le$$
$$M \int_{-\infty}^{\infty} e^{-(a-b)x^2} dx.$$

From (No. (1)-Table 1), we have $\int_{-\infty}^{\infty} e^{-(a-b)x^2} dx = \frac{\pi}{\sqrt{a-b}}$.

Thus $|\mathcal{L}(f(x); a)| \le M \frac{\sqrt{\pi}}{\sqrt{a-b}}, a > b$.

It can be checked easily that the condition (2.2) holds. Indeed, if we choose, for example, $f(x) = x^{2n}$, then from Maclaurin series that is, $x^{2n} < n! e^{x^2}$ and so on.

Theorem 2 *Let* $\mathcal{L}(f(x); a) = \int_{-\infty}^{\infty} e^{-ax^2} f(x) dx = \mathcal{B}(a), a > 0$, *then*

1- $\mathcal{L}(x^2 f(x); a) = -\frac{d\mathcal{B}}{da}(a)$.

2- $\mathcal{L}(xf'(x); a) = -[\mathcal{B}(a) + 2a\frac{d\mathcal{B}}{da}(a)]$.

3- $\mathcal{L}(f''(x); a) = -2a\left[\mathcal{B}(a) + 2a\frac{d\mathcal{B}}{da}(a)\right]$.

4- $\mathcal{L}(x^2 f''(x); a) = \frac{d}{da}\left[2a\left(\mathcal{B}(a) + 2a\frac{d\mathcal{B}}{da}(a)\right)\right]$.

5- $\mathcal{L}(e^{bx^2} f(x); a) = \mathcal{B}(a - b), a > b$ (Shifting Property).

6- $e^{bx^2} f(x) = \mathcal{L}^{-1}(\mathcal{B}(a - b)), a > b$.

Property 2 holds if f is continuous on $(-\infty, \infty)$ and satisfies the condition (2.2) and f' is piecewise continuous on every finite interval on $(-\infty, \infty)$. Similarly, Property 3 holds if f and f' are continuous on $(-\infty, \infty)$ and satisfy (2.2) and f'' is piecewise continuous on every finite interval of $(-\infty, \infty)$.

Proof.

1- $\mathcal{B}(a) = \int_{-\infty}^{\infty} e^{-ax^2} f(x) dx, a > 0$.

Differentiating $\mathcal{B}(a)$ under the integral sign with respect to the parameter a, we obtain

$$\frac{d\mathcal{B}}{da} = \mathcal{B}'(a) = -\int_{-\infty}^{\infty} e^{-ax^2} x^2 f(x) dx = -\mathcal{L}(x^2 f(x); a).$$

2- Assume that $f'(x)$ is continuous on $(-\infty, \infty)$. Thus, $\mathcal{L}(xf'(x); a) = \int_{-\infty}^{\infty} e^{-ax^2} xf'(x) dx$.

Since f satisfies $|f(x)| \le Me^{bx^2}$, integration by parts yields

$$\mathcal{L}(xf'(x); a) = -\int_{-\infty}^{\infty} e^{-ax^2} f(x) dx + 2a \int_{-\infty}^{\infty} e^{-ax^2} x^2 f(x) dx$$

The integrals $\mathcal{L}(f(x); a)$ and $\mathcal{L}(x^2 f(x); a)$; $a)$ exist for $a > b$. So that $\mathcal{L}(xf'(x); a)$ exists for $a > b$. Using now $\mathcal{B}(a) = \mathcal{L}(f(x); a)$ and $\mathcal{B}'(a) = -\mathcal{L}(x^2 f(x); a)$, we obtain the desired property.

If f' is piecewise continuous on $(-\infty, \infty)$. Then, the proof is similar.

3- Assume that f'' is continues on $(-\infty, \infty)$. Thus, by Definition 1, we have $\mathcal{L}(f''(x); a) = \int_{-\infty}^{\infty} e^{-ax^2} f''(x) dx$.

Integration by parts yields

$$\mathcal{L}(f''(x); a) = -2a \int_{-\infty}^{\infty} e^{-ax^2} f(x) dx + (2a)^2 \int_{-\infty}^{\infty} e^{-ax^2} x^2 f(x) dx.$$

Since f and f' satisfy (2.2), the two integrals $\mathcal{L}(f(x); a)$ and $\mathcal{L}(x^2 f(x); a)$ exist for $a > b$. So that $\mathcal{L}(f''(x); a)$ exists for $a > b$, and the proof is complete.

The proof of this for f'' is piecewise continuous on $(-\infty, \infty)$ is similar.

4- Properties 4 follows simply from Definition 1 and Property 3.

5- $\mathcal{L}(e^{bx^2} f(x); a) = \int_{-\infty}^{\infty} e^{-(a-b)x^2} f(x) dx = \mathcal{B}(a - b), a > b.$

In order to verify the accuracy of our present method, we present some elementary examples.

3 Applications: Solutions of linear second-orders ODE

It is important to note a key difference in our approach before using this transformation. Unlike the Laplace, this new integral transform transform focuses On expressing $\mathcal{B}(a)$ and its derivatives $\mathcal{B}'(a)$, $\mathcal{B}''(a),\dots$ with respect to a while dealing with the derivatives of functions. This is explained in Properties 1-6. Our approach works in general for finding one solution for the second-order differential equations by using the properties that govern this transform. Therefore, considering initial and boundary conditions at the first step is not necessary for any obtained solution.

It happens quite often that one solution can be found by this integral trans- form. Then a second linearly independent solution can be deduced by the method of reduction of order, which works easily in general. It is important to note that when using the new transform, the general solutions obtained should contain undetermined constants and these constants can be deter- mined by including the initial or boundary conditions that are given. To help understand this process, we provide some examples below:

3.1 Equation of free oscillations

We begin by considering the linear equation for free oscillations

$$y'' - w^2 y = 0, -\infty < x < \infty, \quad (3.1)$$

Applying (2.3) to both sides of Eq.(3.1), we have

$$\mathcal{L}(y''; a) - w^2 \mathcal{L}(y; a) = 0 \quad (3.2)$$

Using Definition 1 and Property 3, we obtain

$$-2a[\mathcal{B}(a) + 2a\frac{d\mathcal{B}}{da}(a)] - w^2\mathcal{B}(a) = 0. \quad (3.3)$$

Thus,

$$(2a)^2 \frac{d\mathcal{B}}{da}(a) + (w^2 + 2a)\mathcal{B}(a) = 0. \quad (3.4)$$

which is a linear first-order equation. Solving for $\mathcal{B}$, we obtain $\mathcal{B}(a) = \frac{C}{\sqrt{a}} e^{\frac{w^2}{4a}}$, where C is a constant of integration. Hence from Table 1, we have $e^{\pm wx} = \mathcal{L}^{-1}\left(\frac{\sqrt{\pi}}{\sqrt{a}} e^{\frac{w^2}{4a}}\right)$. Thus $y_1 = C_1 e^{wx}$ and $y_2 = C_1 e^{-wx}$, where $C_1 = \frac{C}{\sqrt{\pi}}$. Consequently the general solution is then given by $y = C_1^* e^{wx} + C_2^* e^{-wx}$. The constants C_1^* and C_2^* follow easily from the initial or boundary conditions of this equation.

3.2 Weber Equation

Consider the linear Weber equation

$$y'' - (b^2 x^2 + b)y = 0, -\infty < x < \infty, \quad (3.5)$$

which often arises in various applications. Applying (2.3) to both sides of Eq.(3.5), we have

$$\mathcal{L}(y''; a) - b^2\mathcal{L}(x^2 y; a) - b\mathcal{L}(y; a) = 0. \quad (3.6)$$

Using Definition 1 and Properties 1 and 3, we obtain

$$-2a\left[\mathcal{B}(a) + 2a\frac{d\mathcal{B}}{da}(a)\right] +.$$
$$+b^2\frac{d\mathcal{B}}{da}(a) - b\mathcal{B}(a) = 0 \quad (3.7)$$

Thus,

$$(b^2 - (2a)^2)\frac{d\mathcal{B}}{da}(a) - (b + 2a)\mathcal{B}(a) = 0, \quad (3.8)$$

which is a first-order linear equation. Solving for $\mathcal{B}$, we obtain, $\mathcal{B}(a) = \frac{C}{\sqrt{a - \frac{b}{2}}}, a > \frac{b}{2}$, where C is a constant of integration. Hence from shifting property, we obtain $y_1 = C_1 e^{\frac{b}{2}x^2}, C_1 = \frac{C}{\sqrt{\pi}}$ .The second independent solution y_2 can be obtained by the method of reduction of order. Indeed, if one solution y_1 is known to the homogeneous linear ODE: $y'' + p(x)y' + q(x)y = 0$, then, $y_2 = \int U(x)dx$ where $U(x) = \frac{1}{y_1^2}e^{-\int p(x)dx}$.

So that the desired second solution of Weber equation

$$y_2 = \frac{1}{C_1}e^{\frac{b}{2}x^2}\int e^{-bx^2}dx = \frac{\sqrt{\pi}}{2C_1\sqrt{b}}e^{\frac{b}{2}x^2}\,\mathrm{erf}\left(\sqrt{b}x\right).$$ It follows that y_1 and y_2 form a basis of solutions. Hence, the general solution is obtained $y = C_1^* y_1 + C_2^* y_2$ and the particular solution can be deduced from the general solution and the initial conditions or boundary conditions.

3.3 Euler-Cauchy Equation

Consider the linear Euler-Cauchy equation

$$x^2 y'' + bxy' + cy = 0, -\infty < x < \infty. \quad (3.9)$$

A simple application of (2.3) with Properties 2 and 4 to both sides of Eq.(3.9) leads to

$$(2a)^2\frac{d^2\mathcal{B}}{da^2}(a) + (2a)(5-b)\frac{d\mathcal{B}}{da}(a) +$$
$$+(2 - b + c)\mathcal{B}(a) = 0. \quad (3.10)$$

Note that the Laplace and Sumudu transforms convert Eq. (3.9) into

$$s^2 Y''(s) + s(4-b)Y'(s) + (2-b+c)Y(s) = 0$$
and $s^2 Y''(s) + bsY'(s) + cY(s) = 0$, respectively.

If we assume that $2 - b + c = 0$, that is $b = c + 2$, then this integral transform takes the Euler-Cauchy differential equation and turns it under a suitable condition on its coefficients into a first-order linear differential equation. Thus, Eq.(3.10) becomes $(2a)^2\frac{d^2\mathcal{B}}{da^2}(a) + (2a)(5-b)\frac{d\mathcal{B}}{da}(a) = 0.$ So the Sumudu transform is not a best choice for Euler-Cauchy Equation. The solution is then simple $\mathcal{B}(a) = \frac{C}{b-3}a^{\frac{b-3}{2}} + D$, where C and D are constants of integration. If we assume that $3 - b = 2n + 1, n = 1,2, ...,$ that is, $b = 2 - 2n$, then $\mathcal{B}(a) = -\frac{C}{2n+1}\frac{1}{a^n\sqrt{a}} + D$. Using $\mathcal{B}(a) \to 0$ as $a \to \infty$ to get $D = 0$. Hence, from Table 1, we obtain that $y_1 = C_n x^{2n}, C_n = -\frac{C\,4^n n!}{\sqrt{2}\,(2n)!(2n+1)}, n = 1,2, ...,$ which is indeed a solution of the Cauchy-Euler equation:

$$x^2 y'' + 2(1-n)xy' - 2ny = 0,.$$
$$-\infty < x < \infty \quad (3.11)$$

The second independent solution y_2 can be also obtained by the method of reduction of order.

3.4 The associated Bessel Equation

Consider the linear associated Bessel equation

$$x^2 y'' + 2(m+1)xy' +,$$
$$[x^2 - l(l + 2m + 1)]y = 0, -\infty < x < \infty \quad (3.12)$$

where l and m are parameters. Applying (2.3) and using Properties 1, 2 and 4, we obtain

$$(2a)^2\frac{d^2\mathcal{B}}{da^2}(a) + (6a - 4am - 1)\frac{d\mathcal{B}}{da}(a) -.$$
$$[2m + l(l + 2m + 1)]\mathcal{B}(a) = 0 \quad (3.13)$$

Proceeding as in Example 3, if we assume that $2m + l(l + 2m + 1) = 0$, then, Eq.(3.21) can be converted into

$$(2a)^2\frac{d^2\mathcal{B}}{da^2}(a) + (6a - 4am - 1)\frac{d\mathcal{B}}{da}(a) = 0. \quad (3.14)$$

Hence $\frac{d\mathcal{B}}{da}(a) = \frac{C}{a^{\frac{3-2m}{2}}}e^{-\frac{1}{4a}}$. As a specific example, let $m = 1$. Thus $\frac{d\mathcal{B}}{da}(a) = \frac{C}{\sqrt{a}}e^{-\frac{1}{4a}}$. Using

Property 1: $\mathcal{L}(x^2 y''; a) = -\frac{dB}{da}$ and from Table 1, we immediately obtain $y_1 = C_1 \frac{\cos x}{x^2}$, which is a solution to Eq. (3.12) when

$$m = 1 \ and \ l = 1 \ or \ l = 2.$$

3.5 Other Equations

We would now like to examine other equations. Let

$$xy' + y = (x^2 + 1)e^{\frac{x^2}{2}}, -\infty < x < \infty. \quad (3.15)$$

Applying (2.3) to both sides of Eq.(3.15), we obtain, $\mathcal{L}(xy'; a) + \mathcal{L}(y; a) = \mathcal{L}\left((x^2 + 1)e^{\frac{x^2}{2}}; a\right)$. (3.16)

Using Property 2 and Definition 1, we obtain

$$-\left[\mathcal{B}(a) + 2a\frac{dB}{da}(a)\right] + \mathcal{B}(a) =$$
$$= \mathcal{L}\left((x^2 + 1)e^{\frac{x^2}{2}}; a\right). \quad (3.17)$$

Since $\mathcal{L}\left((x^2 + 1)e^{\frac{x^2}{2}}; a\right) = \mathcal{L}\left(x^2 e^{\frac{x^2}{2}}; a\right) + \mathcal{L}\left(e^{\frac{x^2}{2}}; a\right)$, $\mathcal{L}\left(e^{\frac{x^2}{2}}; a\right) = \frac{\sqrt{\pi}}{\sqrt{a-\frac{1}{2}}}$ and $\mathcal{L}\left(x^2 e^{\frac{x^2}{2}}; a\right) = \frac{\sqrt{\pi}}{2}\frac{1}{\left(a-\frac{1}{2}\right)\sqrt{a-\frac{1}{2}}}$, where $a > \frac{1}{2}$. We have

$$\frac{dB}{da}(a) = -\frac{\sqrt{\pi}}{2}\frac{1}{2a\left(a-\frac{1}{2}\right)\sqrt{a-\frac{1}{2}}} - \frac{\sqrt{\pi}}{2a\sqrt{a-\frac{1}{2}}}, a > \frac{1}{2}. \quad (3.18)$$

Solving for $\mathcal{B}$, we obtain

$$\mathcal{B}(a) = -\frac{\sqrt{\pi}}{2}\int\frac{1}{2a\left(a-\frac{1}{2}\right)\sqrt{a-\frac{1}{2}}}da - \\ -\sqrt{\pi}\int\frac{1}{2a\sqrt{a-\frac{1}{2}}}da. \quad (3.19)$$

Since

$$\int\frac{1}{2a\sqrt{a-\frac{1}{2}}}da = \sqrt{2}\arctan(\sqrt{2a-1}) \quad (3.20)$$

And

$$\int\frac{1}{2a(a-\frac{1}{2})\sqrt{a-\frac{1}{2}}}da = -2^{\frac{3}{2}}\arctan(\sqrt{2a-1}). \quad (3.21)$$

We have $\mathcal{B}(a) = \frac{\sqrt{2\pi}}{\sqrt{2a-1}} + C$. Using $\mathcal{B}(a) \to 0 \ as \ a \to \infty$, to get $\mathcal{B}(a) = \frac{\sqrt{\pi}}{\sqrt{a-\frac{1}{2}}}$.

It follows that, from Table 1, $y_1(x) = e^{\frac{x^2}{2}}$. Consequently, the general solution to this equation is construct as the sum of y_1 and z, where z is the general solution to the corresponding homogeneous $xy' + y = 0$. Hence $y(x) = e^{\frac{x^2}{2}} + \frac{C}{x}$ and the constant C can be determined from the IC $y(x_0) = \alpha, x_0 \neq 0$.

4 Conclusion

This new integral transform has been demonstrated to provide accurate and computable solutions for a wide class of linear second-order differential equa- tions with variable coefficients such as Euler-Cauchy Equation, Weber's equa- tion and Bessel's equation. This integral transform takes a differential equation and turns it into a first-order linear differential equation, which is simpler than the given second-order and can be easily solved, applying the inverse transform gives us our desired solution. But sometimes the application of this integral transform gives a second-order ODE with variable coefficients, and this will show that the present method works well only under suitable conditions on the coefficients of this ODE.

Conflicts of Interest

The authors declare no conflicts of interest.

References

1. L. Bougoffa and R. Rach, Evaluation of Gaussian integrals by Ado- mian decomposition, *Scientia Series A: Mathematical Sciences*, Vol. 30 (2020), 1–5.

2. G. Adomian, Nonlinear Stochastic Systems Theory and Applications to Physics, Kluwer Aca- demic Publishers, Dordrecht, 1989.

3. G. Adomian and R. Rach, Evaluation of integrals by decomposition, *Journal of Computational and Applied Mathematics,* 23(1986), 99–101.

4. Victor H. Moll, Special Integrals of Gradshteyn and Ryzhik: The Proofs- Volume II, CRC Press, Taylor and Francis Group, 2016.

5. F. Dawson,On the Numerical Value of $\int_0^h e^{x^2} dx$, *London Math. Soc. Proc.,* 29, 519-522, 1898.

6. D.A. Dijkstra,A Continued Fraction Expansion for a Generalization of Dawson's Integral, *Math. Comp.,* 31, 503-510, 1977.

7. B. D. Fried and S. D. Conte, The Plasma Dispersion Function (Aca- demic, New York, 1961).

8. S. M. Stewart, Some alternative derivations of Craig's formula, *The Mathematical Gazette,* Vol. 101, No. 551, pp. 268-279, 2017.

9. V.A. Ditkin and A.P. Prudnikov, Integral Transforms and Operational Calculus (Oxford: Pergamon), 1965.

10. Andrei D. Polyanin, Valentin F. Zaitsev, Handbook of Exact Solutions for Ordinary Differential Equations, Second Edition, Chapman and Hall/CRC, 2003.

11. Isaac I.H. Chen, The associated Bessel functions and recurrence formulas, *INT. J. MATH. EDUC. SCI. TECHNOL.,* 1984, VOL. 15, NO. 3, 345–348.

12. Victor H. Moll, Special Integrals of Gradshteyn and Ryzhik: The Proofs- Volume II, CRC Press, Taylor and Francis Group, 2016.

13. Owen, D., A table of normal integrals, *Communications in Statistics: Simulation and Computation,* B9 (4): 389–419. 1980.

Information about authors:
Lazhar Bougoffa – Professor of Department of Mathematics, Faculty of Science, Imam Mohammad Ibn Saud Islamic University (IMSIU), (Riyadh, Saudi Arabia. e-mail address: lbbougoffa@imamu.edu.sa).

N.A. Beissen[1] , D.S. Utepova[1,2*] , V.N. Kossov[2] , S. Toktarbay[1,3] ,

M.K. Khassanov[1] , T. Yernazarov[1] , A.K. Imanbayeva[1]

[1]Al-Farabi Kazakh National University, Almaty, Kazakhstan
[2]Abai Kazakh National Pedagogical University, Almaty, Kazakhstan
[3]Kazakh National Women's Teacher Training University, Almaty, Kazakhstan
*e-mail: utepova_daniya@mail.ru

Comparing the efficiency of GPU and CPU in gravitational lensing simulation

Abstract. In this study, we investigate the computational advancements in simulating gravitational lensing, particularly focusing on the Schwarzschild black hole model. The traditional approach of back ray tracing, where photons are traced back from the observer to the source, is computationally intensive, especially when aiming to achieve high-resolution images of lensing effects around black holes. By employing a numerical method that integrates the Schwarzschild metric with initial conditions derived from the observer's plane, we map the deflection of light around a black hole to generate simulated images of gravitational lensing.
The core of our study is the comparison between traditional CPU-based (Central Processing Unit-based) computations and GPU-accelerated (Graphics Processing Unit-accelerated) processes using the Numba library. Our findings reveal that GPU acceleration, with its parallel processing capabilities, significantly reduces computation time, particularly as the complexity of the simulation increases with larger grid sizes. This computational efficiency is crucial for simulations of gravitational lensing, where the number of independent calculations grows exponentially with the resolution and accuracy of the desired image.
Our study underscores the importance of leveraging GPU technology for astrophysical simulations on personal computers, offering a substantial improvement in performance over CPU-based methods.
Key words: Gravitational Lensing, GPU Parallelization, Schwarzschild Black Hole, Ray Tracing Methods, Numba Library.

Introduction

One of the most astonishing predictions of Einstein's equations corresponds to the final state of the gravitational collapse of a massive star: a Black Hole. These enigmatic objects, characterized by their intense gravitational fields from which not even light can escape, are described by solutions to Einstein's field equations, known as metrics. The Schwarzschild metric, for example, describes a non-rotating black hole [1], while the Kerr metric accounts for one that rotates [2]. These metrics play a crucial role in understanding the spacetime curvature around black holes and the resultant phenomena such as gravitational lensing.

A monumental achievement in the observation of black holes was made by the Event Horizon Telescope (EHT) collaboration, which captured the first-ever image of a supermassive black hole located at the center of the galaxy M87 [3]. This historic image, showing the shadow of the black hole surrounded by a ring of light distorted by its massive gravitational field, provides unprecedented direct visual evidence of a black hole's existence, and offers a profound confirmation of general relativity in the strong gravity regime. The EHT's success not only marks a significant milestone in observational astronomy but also highlights the critical role of simulations in interpreting the bending of light and the structure of the space around black holes.

Furthermore, the EHT has also studied the supermassive black hole at the center of our own Milky Way galaxy, known as Sagittarius A* (Sgr A*). Recent observations have similarly captured the shadow of Sgr A*, providing additional invaluable data that reinforces our understanding of black hole environments and the behavior of light in intense gravitational fields [4]. These studies of both M87

and Sgr A* enhance our comparative understanding of black hole dynamics and continue to validate the theoretical frameworks underpinning general relativity.

There are various methods to simulate the lensing effects caused by massive objects like black holes [5]. One such method is the back ray tracing method [6], which effectively reverses the path of light from the observer to the source through the curved spacetime around a massive object. This method allows for the accurate simulation of the bending of light as it passes near a massive object, providing insights into the observable phenomena associated with gravitational lensing.

In this work, we will focus on accelerating the computation of the lensing effect, which utilizes the back ray tracing method, by leveraging the parallel processing capabilities of GPUs. The use of GPUs for such simulations represents a significant advancement over traditional CPU-based computations, allowing for a substantial increase in computational efficiency and speed. By employing simple tools available in Python, we aim to demonstrate the feasibility and benefits of using GPU acceleration for the simulation of gravitational lensing effects, offering a more accessible and efficient approach for researchers and enthusiasts in the field of astrophysics.

Models

Schwarzschild Black Hole

A Schwarzschild black hole represents the simplest type of black hole, which is non-rotating and spherically symmetric [1]. We choose to focus on the Schwarzschild metric for this study because it offers the simplest model to illustrate our goals, allowing for a clear understanding of the fundamental principles without the complexities introduced by rotation or charge. It is described by the Schwarzschild metric, a solution to Einstein's field equations in general relativity. The Schwarzschild metric is given by the following equation in spherical coordinates (t, r, θ, φ)

$$ds^2 = -\left(1 - \frac{2GM}{c^2 r}\right) c^2 dt^2 + \frac{1}{1 - \frac{2GM}{c^2 r}} dr^2 +$$
$$+ r^2 d\theta^2 + r^2 \sin^2 \theta \, d\varphi^2 \qquad (1)$$

where ds^2 is the spacetime interval, G is the gravitational constant, M is the mass of the black

hole, c is the speed of light, and r, θ, ϕ are the radial, polar, and azimuthal coordinates, respectively. The term $2GM/c^2$ represents the Schwarzschild radius, beyond which spacetime is significantly curved by the mass of the black hole. Further, we will assume $G = c = 1$, as is commonly accepted in the GR.

The equation of motion for light, or photons, moving in the vicinity of a Schwarzschild black hole can be derived from the Schwarzschild metric. In context of the energy E and the angular momentum L the equation of motion can be written as [7]:

$$\frac{dr}{d\lambda} = v_r \qquad (2.1)$$

$$\ddot{r} = -[\frac{M}{r^2 - 2M} E^2 + \frac{M}{2Mr - r^2} \dot{r}^2 +$$

$$+ (2M - r)\dot{\theta}^2 + \frac{2M - r}{r^4 \sin^2 \theta} L^2] \qquad (2.2)$$

$$\frac{d\theta}{d\lambda} = v_\theta \qquad (2.3)$$

$$\ddot{\theta} = -\frac{2}{r} \dot{r}\dot{\theta} + \frac{\cos \theta}{r^4 \sin^3 \theta} L^2 \qquad (2.4)$$

$$\frac{d\varphi}{d\lambda} = \frac{L}{r^2 \sin^2 \theta} \qquad (2.5)$$

These five equations form the basis for implementing the back ray tracing method, where v_r and v_θ represent the velocity components r and θ directions, respectively. E denotes energy, and L denotes angular momentum, both of which are given in the form [8].

$$E = \sqrt{-g_{tt}} \qquad (3)$$

$$L = p_\varphi \qquad (4)$$

Back ray tracing

In contrast to natural lensing image generation, there is a noticeable difference when the lensing image is generated computationally. One of the most effective methods of generating this process using computational means is the back ray tracing method, the essence of which is the propagation of photons back in time from the observer to the source of gravity.

To obtain the lensing image of a black hole using the back ray tracing method, we position our black hole model at the origin (see Figure 1a) within Minkowski spacetime and encircle it with a virtual

background sphere, colored in four colors: red, green, yellow, and blue. The observer is located inside this background sphere and looks towards the exact point where all four colors intersect. In the absence of a black hole, the observer would see a picture as depicted in Figure 1b.

Consider two local coordinate systems: (x, y, z) and (r, θ, φ). The first system is associated with the observer, and the second with the black hole. In this setup, the $z-$axis is directed towards the black hole. At the point $z = 0$, there is an observer whose coordinates in the black hole's reference frame are $(r_O, \theta_O, \varphi_O)$.
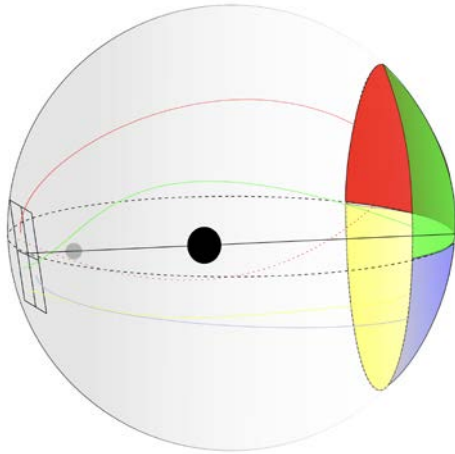
Figure 1a – Schematics of the mapping of Black Hole and observer
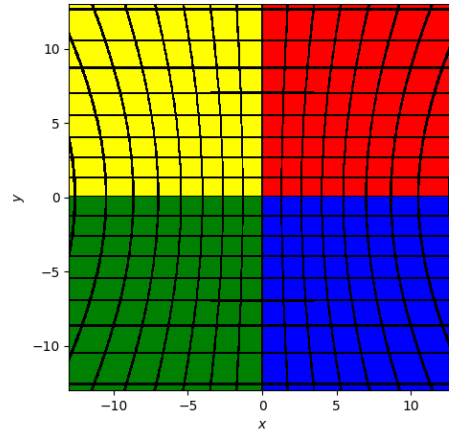
Figure 1b – Grid representing the background sphere in flat spacetime

Because the geodesic equations for light rays are represented in Schwarzschild metric coordinates (r, θ, φ), it is necessary to convert the initial conditions of the light ray on the image plane. This transformation can be done using expressions $(5.1) - (5.6)$. More details about these expressions can be found in the work [9-12]:

$$r(0) = \sqrt{r_O^2 + x^2 + y^2} \qquad (5.1)$$

$$\theta(0) = \cos^{-1}\left[\frac{r_O \cos \theta_O + y \sin \theta_O}{r(0)}\right] \qquad (5.2)$$

$$\varphi(0) =$$
$$= \tan^{-1}\left[\frac{(y \cos \theta_O - r_O \sin \theta_O)sin\varphi_O - xcos\varphi_O}{(y \cos \theta_O - r_O \sin \theta_O)cos\varphi_O - xsin\varphi_O}\right] \qquad (5.3)$$

and the initial tangent vector $(\dot{x}, \dot{y}, \dot{z}) \approx (0,0,1)$ is translated into

$$\dot{r}(0) = -\frac{r_O}{r(0)} \qquad (5.4)$$

$$\dot{\theta}(0) = \frac{(x^2+y^2) \cos \theta_O - yr_O \sin \theta_O}{r^2(0)\sqrt{x^2+(y \cos \theta_O - r_O \sin \theta_O)^2}} \qquad (5.5)$$

$$\dot{\varphi}(0) = \frac{x \sin \theta_O}{x^2+(y \cos \theta_O - r_O \sin^2 \theta_O)} \qquad (5.6)$$

Thus, by discretizing the observer plane and numerically solving equations (2.1)-(2.5) for each cell (x_i, y_i) considering the initial conditions (5.1)-(5.6), we obtain the image of the black hole as shown in Figure 2. The massive computations are performed by Runge-Kutta-4 method.
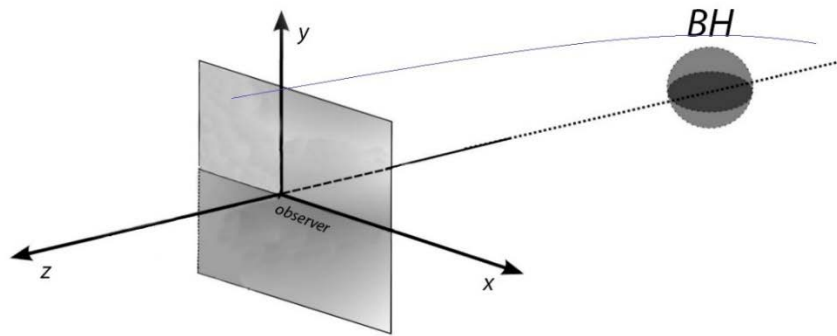
Figure 2 – Creating an image of a black hole's lensing effect from the viewpoint
of a distant observer requires tracing the paths of light rays backward
to each pixel on the observer's image plane
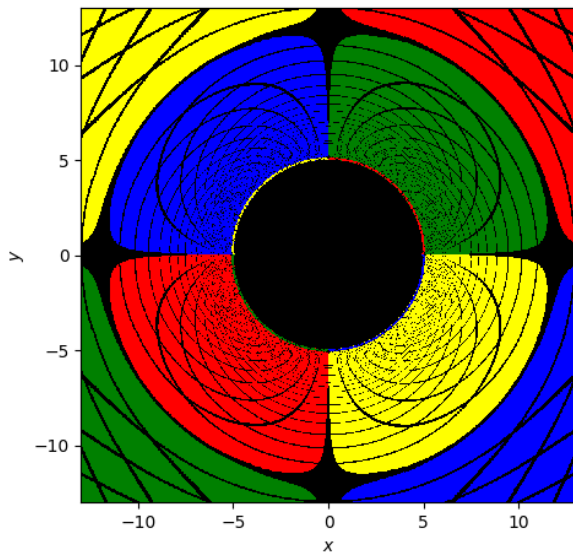
Figure 3 – Lensing of Schwarzschild Black Hole
with mass $M = 1$. The observer is at initial position
$r_O = 15$, in the equatorial plane ($\theta_O = \pi/2$).
The background sphere is at $r = 30$.
The image contains 1000×1000 cells.
($G = c = 1$, geometric units)

As anticipated, the shadow depicted in figure 3 forms a precise circle, reflecting the spherical symmetry characteristic of the Schwarzschild Black Hole. It's crucial to highlight several aspects of the image [13].

• Photons associated with large absolute values of x and y are considered direct photons. This means they do not circumnavigate the Black Hole on their way to the background. Additionally, the further we move away from the Black Hole, the more the spacetime resembles Minkowski spacetime.

• In addition to the shadow, examining Figure 3 reveals two distinct areas (an inner and an outer zone). The inner zone is associated with photons that have circled the Black Hole once.

• Should there be a white spot in the background image, as depicted in Figure 1a, the act of lensing would result in the creation of an Einstein ring. This ring would precisely align at the boundary separating the inner and outer zones mentioned previously

Results and Discussion

Acceleration by python tools

Here, we will examine the code's flowchart for obtaining the image of a lensing object and discuss modifying this code to run on a graphics processing unit (GPU) using the Numba package.

First, let's look at the flowchart of the code designed to run on a CPU (see Figure 4). As illustrated in Figure 4, the program is structured as follows: it begins with the initialization of input parameters, then calculates the components of the metric tensor (in our case, the Schwarzschild metric). Following this, a ray is launched from each cell on the observer's plane in the reverse direction with unique initial conditions, and the ray's position is calculated at each step until it either enters the event horizon area or leaves the outer sphere. The history of each ray is calculated sequentially, one after another. After determining the history of all rays, the image is formed.
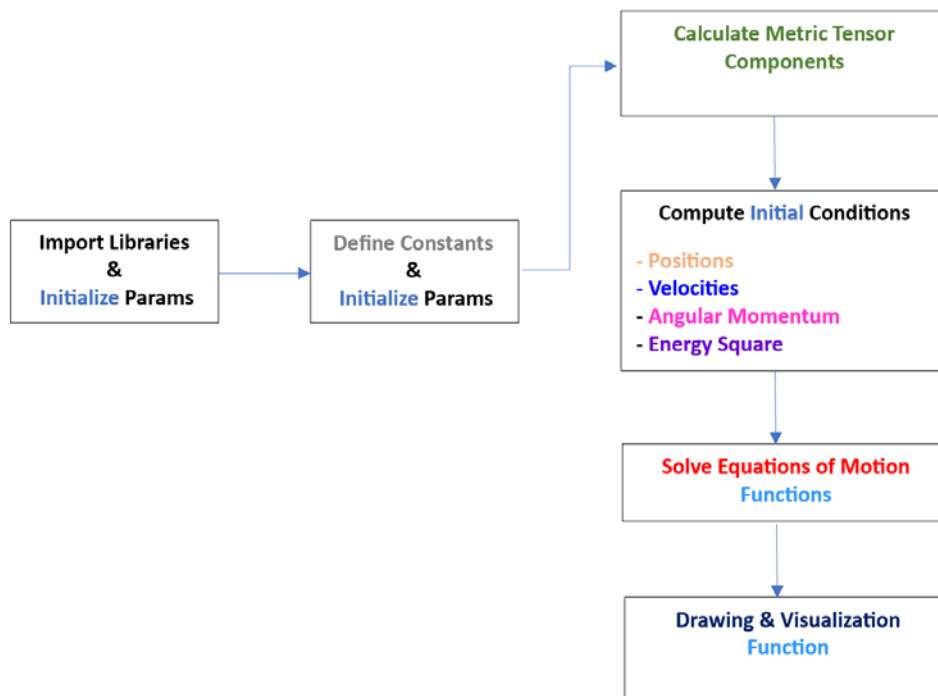
Figure 4 – A simplified block diagram representing
the flow and functionalities of the code running on the CPU

From the flowchart presented, it becomes immediately clear that this task is highly suited for parallel computation since it is evident that tracking the history of each ray in parallel, rather than waiting for the completion of the previous one, is the most efficient approach. The easiest way to implement this is to use the Numba library [14]. Numba is a just-in-time compiler that accelerates Python code, especially for numerical computations, by converting it to machine-level code. It supports both CPU and GPU execution, making it ideal for parallel computing tasks. With Numba, developers can achieve significant performance improvements without major changes to their existing Python code, leveraging the power of GPUs for faster data processing and analysis. To parallelize the code and run it on a graphics processor using the Numba library, it suffices to add the @jit(target_backend='cuda') decorator to all functions where calculations are performed relative to a given ray. As a result, we obtain code designed for execution on a graphics processor, the flowchart of which is presented in Figure 5.

Next, we will present a graph comparing the computational time of the code executed on a CPU versus the code executed on a GPU using the Numba package.

The comparison plot (Fig. 6) shows that the calculation time of the original (non-parallel) method shows a linear increase on a logarithmic scale, indicating a power law relationship between grid size and calculation time. In contrast, the modified method using CUDA shows a nonlinear increase. This nonlinearity arises from the overhead associated with parallel processing and memory management on the GPU. As grid size increases, the benefits of parallelization become more pronounced, but the initial overhead and complexity of managing large data sets across multiple cores results in a nonlinear trend in computational efficiency.
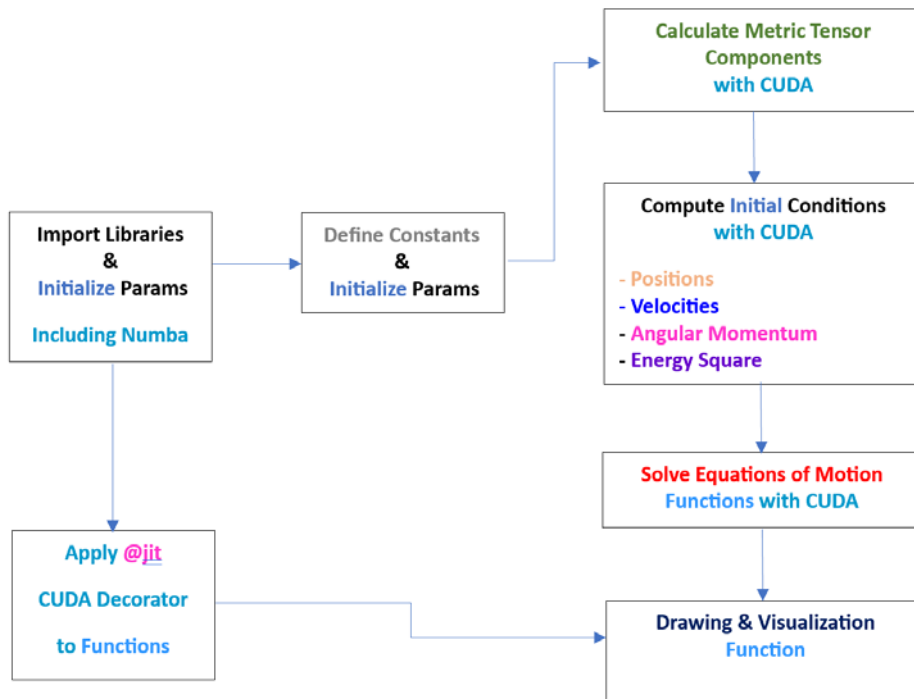
Figure 5 – A modified block diagram representing
the flow and functionalities of the code running on the GPU
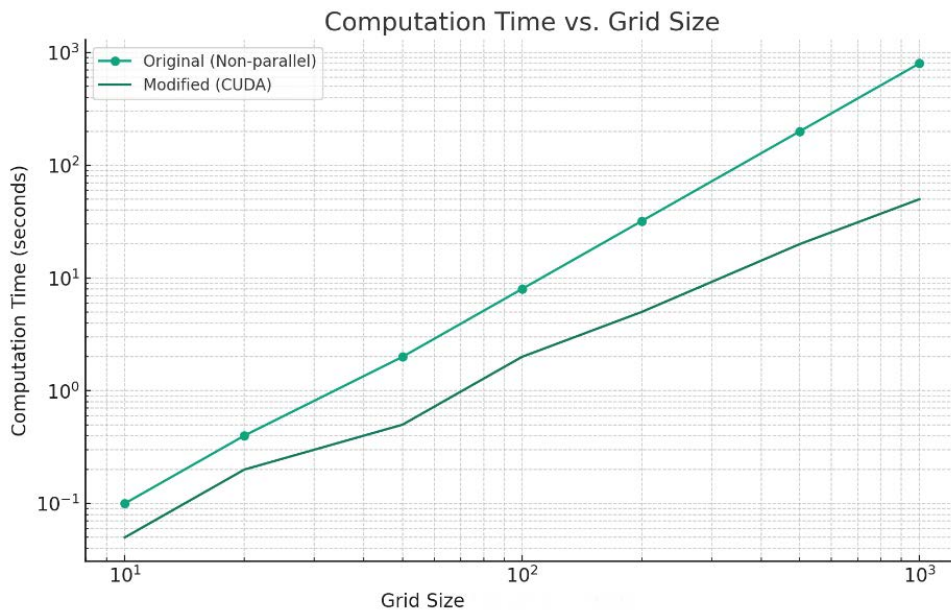
Figure 6 – The graph illustrates the comparison of computation time between
the original (non-parallel) and modified (CUDA-parallel) methods when increasing
the grid size from 10x10 to 1000x1000. Here both axes are presented on a logarithmic scale

Conclusion

Our study highlights the considerable computational benefits of applying GPU acceleration with the Numba library for gravitational lensing simulations. By transitioning from CPU to GPU execution, we noted a significant reduction in computation time, especially for larger grid sizes, underscoring the efficiency of parallel processing. The use of Numba stands out as the simplest method for parallelizing Python code to run on a GPU, offering a straightforward path to enhance simulation speed. This technique not only renders complex simulations more accessible but also paves the way for broader and more detailed astrophysical studies. In the future, we plan to consider various quadrupolar space-times, both static [15-21] and stationary [22] and in this case, using the GPU for calculations will be even more time efficient, since in this scenario the geodesy equations become more complex and require more computational time in the context of a single light beam.

Acknowledgments

References

1. Schwarzschild K. Über das Gravitationsfeld eines Massenpunktes nach der Einsteinschen Theorie. *Sitzungsberichte der Königlich Preußischen Akademie der Wissenschaften.* 1 (1916) 189-196.
2. Kerr R.P. Gravitational Field of a Spinning Mass as an Example of Algebraically Special Metrics. *Physical Review Letters.* 11(5) (1963) 237-238.
3. Event Horizon Telescope Collaboration, Kazunori Akiyama, et al. First M87 Event Horizon Telescope Results. IV. Imaging the Central Supermassive Black Hole. *Astrophys. J.* 875(1) (2019): L4. DOI: 10.3847/2041-8213/ab0e85.
4. The Event Horizon Telescope Collaboration (May 1, 2022). "First Sagittarius A* Event Horizon Telescope Results. I. The Shadow of the Supermassive Black Hole in the Center of the Milky Way". *The Astrophysical Journal Letters.* 930 (2): L12.
5. Hilbert S., Hartlap J., White S.D.M., & Schneider P. Gravitational Lensing with Three-Dimensional Ray Tracing: A Comparative Study of Ray Tracing Methods. (2011) *arXiv:*1110.4894.
6. Nightingale J.W., Hayes R.G., Kelly A., Amvrosiadi, A., Etherington A., He Q., Li N., Cao X., Frawley J., Cole S., Enia A., Frenk C.S., Harvey D.R., Li R., Massey R.J., Negrello M., Robertson A. PyAutoLens: Open-Source Strong Gravitational Lensing. *Journal of Open Source Software.* 6(58) (2021), 2525. DOI: 10.21105/joss.02825
7. Weinberg, S. Gravitation and Cosmology: Principles and Applications of the General Theory of Relativity. *John Wiley & Sons.* (1972) ISBN 0471925675. P.185.
8. Velásquez-Cadavid J.M., Arrieta-Villamizar J.A., Lora-Clavijo F.D. et al. OSIRIS: a new code for ray tracing around compact objects. *Eur. Phys. J.* 82 (2022) 103 DOI: 10.1140/epjc/s10052-022-10054-0.
9. Younsi Z. General relativistic radiative transfer in black hole systems. Ph. D. Thesis. April (2014).
10. Younsi Z., Zhidenko A., Rezzolla L., Konoplya R., and Mizuno Y. New method for shadow calculations: Application to parametrized axisymmetric black holes. *Phys. Rev. D.* 94(8) (2014) 084025. DOI: 10.1103/PhysRevD.94.084025
11. Hung-Yi Pu, Kiyun Yun, Ziri Younsi, and Suk-Jin Yoon. Odyssey: A Public GPU-Based Code for General-Relativistic Radiative Transfer in Kerr Spacetime. *Astrophys. J.* 820(2) (2016) 105. DOI: 10.3847/0004-637X/820/2/105.
12. Lin F.L., Patel A. & P, H.Y. Black hole shadow with soft hairs. *J. High Energ. Phys.* 117 (2022). DOI: 10.1007/JHEP09(2022)117.
13. Pedro V.P. Cunha, Nelson A.Eiró, Carlos A.R. Herdeiro, José P.S. Lemos. Lensing and shadow of a black hole surrounded by a heavy accretion disk., *Journal of Cosmology and Astroparticle Physics.* (2020), March. DOI: 10.1088/1475-7516/2020/03/035.
14. Numba, High-Performance Python with CUDA Acceleration: (2013). https://developer.nvidia.com/blog/numba-python-cuda-acceleration/.
15. Boshkayev K., Gasperı̇n E., Gutierrez- Pineres A.C., Quevedo H., Toktarbay S. Motion of test particles in the field of a naked singularity, *Phys. Rev. D.* 93 (2016) 024024. DOI: 10.1103/PhysRevD.93.024024.
16. Abishev M., Beissen N., Belissarova F., Boshkayev K., Mansurova A., Muratkhan A, Quevedo H., Toktarbay S. Approximate perfect fluid solutions with quadrupole moment. *International Journal of Modern Physics D.* 30(13) (2021) 2150096. DOI: 10.1142/S0218271821500966.
17. Toktarbay S., Quevedo H., Abishev M., Muratkhan A. Gravitational field of slightly deformed naked singularities, *European Physical Journal C.* 82(4) (2022). DOI: 10.1140/epjc/s10052-022-10230-2.
18. Muratkhan A., Orazymbet A., Zhakipova M., Assylbek M., Toktarbay, S. A shadows from the static black hole mimickers, *International Journal of Mathematics and Physics.* 13(2) 2023 44–49. DOI: 10.26577/ijmph.2022.v13.i2.06.
19. Beissen N., Utepova D., Abishev M., Quevedo H., Khassanov M., Toktarbay S. Gravitational refraction of compact objects with quadrupoles, Symmetry. (2023) 15(614). DOI: 10.3390/sym15030614.
20. Beissen N., Utepova D., Muratkhan A., Orazymbet A., Khassanov M., Toktarbay S. Application of GBT theorem for gravitational deflection of light by compact objects, *Recent Contributions to Physics.* 1(84) (2023) 15-21. DOI: 10.26577/RCPh.2023.v84.i1.02.

21. Quevedo H. Mass Quadrupole as a Source of Naked Singularities. *Int. J. Mod. Phys. D.* 20 (2011) 1779-1787. DOI: 10.1142/S0218271811019852.

22. Toktarbay S., Quevedo H. A stationary q-metric // *Gravitation and Cosmology*. Vol. 20, № 4. (2014) 252-254.

Information about authors:

Beissen N.A. – Candidate of Physical and Mathematical Sciences, associate Professor, Dean of the Faculty of Physics and Technology Al-Farabi Kazakh National University, Almaty, Kazakhstan, e-mail: nurzada.beissen@kaznu.edu.kz

Utepova D.S. – PhD student, Al-Farabi Kazakh National University, Abai Kazakh National Pedagogical University, Almaty, Kazakhstan, e-mail: utepova_daniya@mail.ru

Kossov V.N. – Doctor of Physical and Mathematical Sciences, Professor, Abai Kazakh National Pedagogical University, Almaty, Kazakhstan, e-mail: kosov_vlad_nik@list.ru

Toktarbay S. – PhD, Al-Farabi Kazakh National University, Kazakh National Women's Teacher Training University, Almaty Kazakhstan, e-mail: Saken.Toktarbay@kaznu.edu.kz

Khassanov M.K. – PhD, Al-Farabi Kazakh National University, Almaty Kazakhstan, e-mail: Manas.Khassanov@kaznu.edu.kz

Yernazarov T. – PhD student, Al-Farabi Kazakh National University, Almaty Kazakhstan, e-mail: Tursynbek.Yernazarov@kaznu.edu.kz

Imanbayeva A.K. – Candidate of Physical and Mathematical Sciences, Al-Farabi Kazakh National University, Almaty Kazakhstan, e-mail: akmaral@physics.kz

Ye. Kurmanov[1,2,3*] , T. Konysbayev[1,2] , G. Suliyeva[1,2,4] , G. Ikhsan[1] ,

N. Saiyp[2] , G. Rabigulova[2] and A. Urazalina[1,2,5]

[1]National Nanotechnology Laboratory of Open Type, Almaty, Kazakhstan
[2]Al-Farabi Kazakh National University, Almaty, Kazakhstan
[3]International Engineering Technological University, Almaty, Kazakhstan
[4]Fesenkov Astrophysical Institute, Almaty, Kazakhstan
[5]Institute of Nuclear Physics, Almaty, Kazakhstan
*e-mail: g_suliyeva@mail.ru

Radiative characteristics of accretion disks around rotating regular black holes

Abstract. Our research focuses on examining the characteristics of thin accretion disks encircling rotating regular black holes. In this study, we investigate the important features of accretion disks surrounding Bardeen's regular black holes, which play a crucial role in addressing the singularity issue. The horizon configuration of rotating Bardeen black holes is analyzed in details, as well as the innermost stable circular orbits related to this spacetime. The primary goal is to derive quantitively the radiative flux, differential and spectral luminosities of the accretion disk. Within the specified gravitational field, particularly, by taking the parameter $r_0^* > 0$ and fixing the $j = 0.2$, our findings show that the corresponding accretion disk's luminosity exceeds that one predicted by the Kerr metric at identical value of spin parameter ($j = 0.2$). Making the juxtaposition of Bardeen's black hole parameter r_0^* with the spin parameter j of the Kerr black hole we reveal that the spacetime corresponding to the non-rotating Bardeen black holes, in some certain cases, can imitate the Kerr spacetime.
Key words: rotating Bardeen spacetime, angular velocity, angular momentum, energy and radiative flux.

Introduction

One of general relativity's (GR) most intriguing predictions is the existence of black holes (BHs). Many observational data points available to us now support the presence of BHs in the universe [1, 2]. The existence of BHs in the universe has been overwhelmingly confirmed, and a new era of astronomical detection has begun with the inaugural detection of gravitational waves (GWs) originating from the binary BHs coalescence [3, 4] and the first images of the M87* and SgrA* shadows [1, 2]. Nevertheless, the interpretation of observations does not exclude alternative models of gravity.

A class of BHs with coordinate singularities (horizons) but without true singularities throughout spacetime are called regular black holes (RBHs). In most circumstances, determining a RBH often refers to a spacetime with finite curvature invariants everywhere, especially at the center of the BH [5, 6].

One of early goals for searching for RBH models was to eliminate spacetime singularities. Over the past few years, there has been a significant interest among scientists in singularity-free models of RBHs [7–10]. These models have gained attention because they offer an alternative to the complex causal structures that are inherent in BHs as predicted by GR.

Bardeen introduced the initial version of RBHs, now known as Bardeen BHs, by substituting the mass of Schwarzschild BHs with a function that depends on the radial distance. This modification eliminates the singularity of the Kretschmann scalar in the Bardeen BH. Additionally, the core of this BH exhibits de Sitter characteristics, meaning that the Ricci curvature is positive near the center of the BH [11]. Subsequently to this, several additional models for RBHs have been proposed in the literature [12–17]. It can be readily demonstrated that all of these alternative models for RBHs violate the strong

energy condition, thereby potentially challenging the singularity theorems. The effects of *static* Bardeen and Hayward RBHs on the spectral luminosity of accretion disks has been the subject of recent investigations, which have shown that these BHs behave differently from what is predicted for Schwarzschild and Kerr BHs [18].

Furthermore, the spectral and thermodynamic characteristics of accretion disks surrounding rotating Hayward BHs were studied by some of us in Ref. [19]. Additionally, employing the Hartle-Thorne geometry, we have analyzed the motion of test particles moving in circular orbits [20].

Motivated by the arguments stated above about RBHs, by examining the emission spectrum of the accretion disks, we set a goal to discern between rotating regular BHs and Kerr ones. The Novikov, Page, and Thorne models have been used to assess the properties of an accretion disk.

The paper is structured as follows: In Section II, we outline the key features of rotating RBHs and provide with the results concerning the motion of test particles in orbits encircled by accretion disks. In Section III, the thin accretion disk formalism is applied to considered model of RBHs. Lastly, our findings are discussed in Section V. Throughout the article, we adopt geometric units, where $G = c = 1$.

Bardeen regular black holes

The solution considered here is constructed on the basis of a mass function of the following form:

$$m(r) = M\left[1 + \left(\frac{r_0}{r}\right)^q\right]^{-\frac{p}{q}}. \qquad (1)$$

The objective is to guarantee that the spacetime exhibits asymptotically flat behavior for positive values of p and q under static conditions. Prior research has indicated that such static solutions for RBHs can arise from a theory involving the coupling of nonlinear electrodynamics with gravity [21–23]. In this framework, M and r_0 denote the parameters for mass and length, respectively. The particular selections of $p = q = 3$ and $p = 3$, $q = 2$ correspond to Hayward [16] and Bardeen [11, 24] (BHs). Moreover, opting for $p \geq 3$ guarantees the smoothness of the geometry in the central region of static RBHs.

Upon deriving the aforementioned mass function, the more general line element, which accounts for the cosmological constant Λ and the Kerr rotation parameter will take the subsequent form in Boyer-Lindquist coordinates:

$$ds^2 = -\frac{1}{\Sigma}\left(\Delta_r - \Delta_\theta a^2 \sin^2\theta\right)dt^2 +$$
$$+\frac{\Sigma}{\Delta_r}dr^2 + \frac{\Sigma}{\Delta_\theta}d\theta^2 +$$
$$+\frac{1}{\Xi^2\Sigma}\left[\left(r^2 + a^2\right)^2\Delta_\theta - \Delta_r a^2\sin^2\theta\right]\sin^2\theta d\varphi^2$$
$$-\frac{2a}{\Xi\Sigma}\left[\left(r^2 + a^2\right)\Delta_\theta - \Delta_r\right]\sin^2\theta dt d\varphi, \qquad (2)$$

where

$$\Delta_\theta = 1 + \frac{\Lambda}{3}a^2\cos^2\theta, \ \Sigma = r^2 + a^2\cos^2\theta, \quad (3)$$
$$\Delta_r = \left(r^2 + a^2\right)\left(1 - \frac{\Lambda}{3}r^2\right) - 2rm,$$
$$\Xi = 1 + \frac{\Lambda}{3}a^2, \qquad (4)$$

here a is the parameter of Kerr associated with the source's angular momentum. The metric (2) reduces to the Kerr solution when both Λ and r_0 are vanishing. Hereafter, we will consider the Bardeen rotating RBH for simplicity, i.e. with $p = 3$, $q = 2$, besides, without the cosmological constant, $\Lambda = 0$.

In Ref. [25], the authors investigated the event horizon of a rotating Bardeen BH surrounded by ideal liquid dark matter, and the BH as a particle accelerator. Also, the structure of the horizon and ergosphere in a rotating regular Bardeen BH was studied in Ref. [26].

The rotating Bardeen solution comprises inner and outer horizons, which are useful for defining the accretion disk's features and the values of j and r_0^*. The condition $1/g_{rr} = 0$ allows one to determine the horizons of rotating Bardeen BHs. The condition produces 10 roots, but only 4 of them are physically significant; the other 6 are not. The inner and outer horizons for Bardeen and Kerr BHs are given by two equations. Here, for rotating Bardeen BHs the outer and inner horizons are each given by two equations. The graphical representation of the inner and outer

horizons as functions of r_0^* and $j = a/M$ for rotating Bardeen BHs are shown in Figs. 1, 2, 3 and 4. In the limiting case, for vanishing j the horizon of the Bardeen BH is depicted by Fig. 3. Instead for vanishing r_0^* the horizon of the Kerr metric is described by Figs. 1 and 2.

Another straightforward representation of the horizons can be found using the same condition $1/g_{rr} = 0$, but here one should calculate r_0^* instead

of r_h/M. In this case, we obtain two roots for r_0^* and keep only the positive one. The inner horizon r_h/M ranges from 0 to ~1 and the outer horizon varies from ~1 to 2 in analogy to Figs. 1, 2 and 3. The contours of fixed horizons are illustrated as functions of r_0^* and $j = a/M$ in Fig. 4. It turned out, that rotating Bardeen BHs indeed possess the two horizons as expected and there is no contradictions, which seem to appear in Figs. 1, 2 and 3.
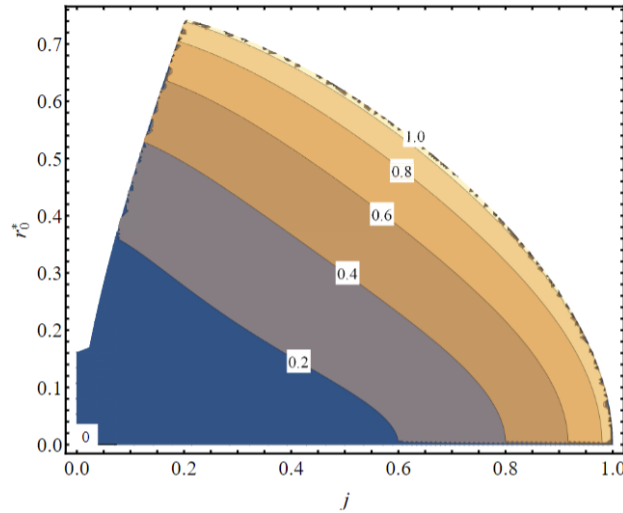
Figure 1 – Contour plots of the rotating Bardeen black hole's inner horizon positions
as a function of the spin $j = a/M$ and deformation $r_0^* = r_0/M$ parameters.
The numbers in the contours indicate the horizon radius normalized by the mass r_h/M
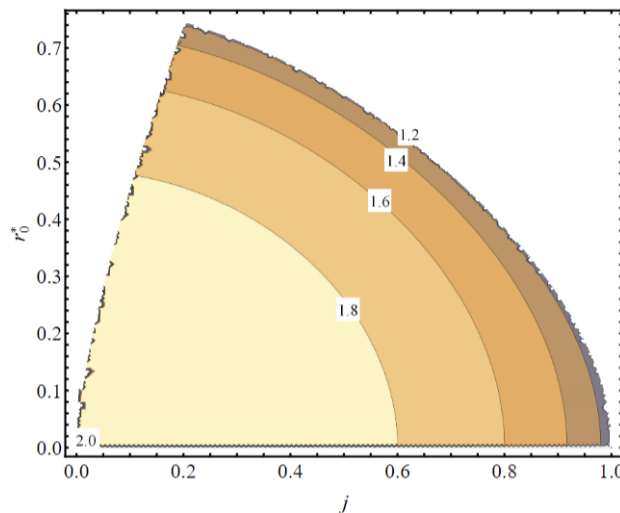
Figure 2 – Contour plots of the rotating Bardeen black hole's outer horizon positions as a function
of $j = a/M$ and $r_0^* = r_0/M$. The numbers in the contours indicate the horizon radius normalized
by the mass r_h/M
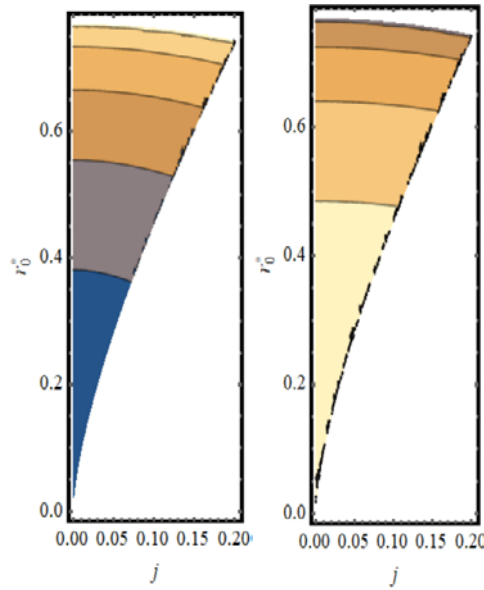
Figure 3 – Contour plots of the rotating Bardeen BH's inner (left panel) and outer (right panel)

horizon positions as a function of $j = a/M$ and $r_0^* = r_0/M$.

Contours indicate fixed values of r_h/M in analogy to Figs. 1 and 2
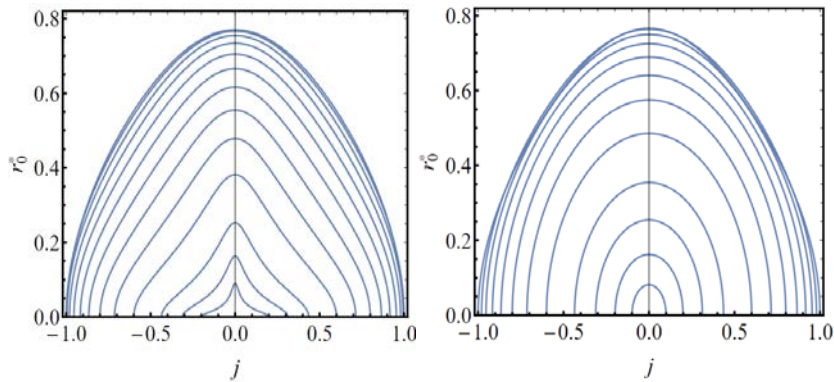
Figure 4 – Contour plots depict the positions of the inner (on the left panel) and outer (on the right panel) horizons of the rotating

Bardeen BH depending on $j = a/M$ and $r_0^* = r_0/M$. The contours represent constant values of r_h/M

Circular orbits for massive test particles in the field of rotating Bardeen regular black holes

The angular velocity of test particles is obtained as follows:

$$\Omega = \frac{aM\left(r^2 - 2r_0^2\right) - \sqrt{M\left(r^2 - 2r_0^2\right)}(r^2 + r_0^2)^{5/4}}{a^2 M\left(r^2 - 2r_0^2\right) - (r^2 + r_0^2)^{5/2}} \, , \quad (5)$$

where $a > 0$ ($a < 0$) is the parameter related to the co-rotating (counterrotating) particles towards the BH's rotation direction.

Subsequently, the radial profiles for the angular momentum L and specific energy E are determined with the following expressions:

$$L = \frac{\left(Kr^2 + a^2 \Pi_+\right)\Omega - aN}{\sqrt{K\left(\Pi_- + 2aN\Omega - \left(Kr^2 + a^2 \Pi_+\right)\Omega^2\right)}}, \quad (6a)$$

$$E = \frac{\Pi_- + aN\Omega}{\sqrt{K\left(\Pi_- + 2aN\Omega - \left(Kr^2 + a^2 \Pi_+\right)\Omega^2\right)}}, \quad (6b)$$

where

$$K = K(r) = (r^2 + r_0^2)^{3/2}, \quad (7)$$

$$N = 2Mr^2, \quad (8)$$

$$\Pi_+ = K + N, \quad (9)$$

$$\Pi_- = K - N. \quad (10)$$

The above expressions for angular momentum and specific energy are characterized by the RBH solution parameters, a and r_0, which fix the constants of motion at any given distance. Further, for the convenience of our analysis, dimensionless quantities are introduced, denoted as $\Omega^*(r) = M\Omega(r)$, $L^*(r) = L(r)/M$, $E^*(r) = E(r)$ and $r_0^* = r_0/M$. In Ref. [19] the behaviors of Ω^*, L^* and E^* are illustrated for Kerr BHs. As predicted, deviations from the Schwarzschild solution become more significant close to the BH (at smaller radial distance).

Massive test particles moving in the gravitational field of a compact object can have an innermost stable circular orbit (ISCO). The radius of the ISCO, denoted as r_{ISCO}, commonly marks the boundary of the accretion disk. This boundary is crucial as it signifies the closest stable orbit around the BH where matter can orbit without being drawn into it. Its specific numerical value is determined by various parameters that describe the gravity source, such as the mass, mass multipoles, angular momentum, charges and other parameters. The significance of the ISCO lies in its paramount role in the study of astrophysical compact objects. To make the constraints about the values for the source parameters, researchers can estimate the ISCO by studying the behavior of accretion disks. For

instance, in the case of a Kerr BH, an estimation of the angular momentum may be obtained using an ISCO measurement, if an independent mass measure is available. The r_{ISCO} is determined by the condition $dL/dr = 0$ [27]. The r_{ISCO} for the Kerr spacetime is determined in Ref. [28]. However, the r_{ISCO} for Bardeen BHs cannot be obtained analytically. Consequently, the value of r_{ISCO} has been computed only numerically.
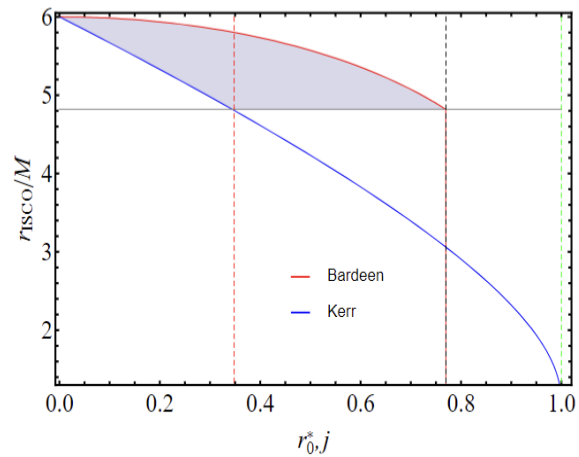
Figure 5 – The r_{ISCO} for the Bardeen BH versus r_0^* in comparison to the r_{ISCO} for the Kerr BH versus j. The shaded region shows the degeneracy in r_{ISCO} for both Bardeen and Kerr spacetimes
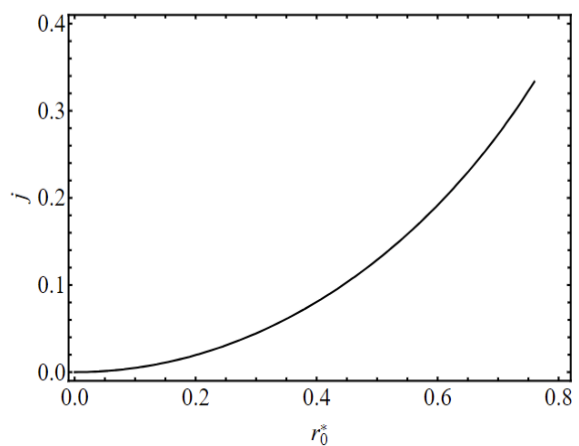
Figure 6 – Degeneracy in the r_{ISCO} values between the Bardeen and Kerr spacetimes. This curve proves that the Bardeen BHs may mimic the Kerr BHs in particular cases.

Fig 5 depicts the r_{ISCO} in the Bardeen spacetime versus r_0^* in comparison to the r_{ISCO} of the Kerr metric versus dimensionless angular momentum j. The red and blue solid curves display the dependence of the r_{ISCO} versus j, r_0^* for Bardeen and Kerr BHs, respectively. The horizontal solid gray line and the shaded region show when r_{ISCO} is equal for both Bardeen and Kerr spacetimes. Thus, we may conclude that r_0^* of the Bardeen BH can mimic j of the Kerr BH up to $j \sim 3.5$. The degeneracy of the r_{ISCO} in the Bardeen spacetime versus r_0^* and that one for the Kerr metric as a function of j is displayed in the Fig. 6.

Thin accretion disk spectra

We employ the well-known formalism outlined in the pioneering works of Page and Thorne, and Novikov and Thorne [29, 30]. Our goal is to understand the dynamics of the accretion disk surrounding spinning RBHs, using numerical analysis.

The radiative flux $\mathcal{F}$ is determined as follows:

$$\mathcal{F}(r) = -\frac{\dot{m}}{4\pi\sqrt{-g}} \frac{\Omega_{,r}}{(E-\Omega L)^2} \int_{r_{\mathrm{isco}}}^{r} (E-\Omega L)L_{,\tilde{r}} d\tilde{r}, \qquad (11)$$

where $\dot{m}$ is the mass accretion rate and
$$\sqrt{-g} = \sqrt{-g_{rr}\left(g_{tt}g_{\varphi\varphi} - g_{t\varphi}^2\right)}.$$

In this context, the assumption of an accretion disk in thermodynamic equilibrium is another crucial approximation. On this supposition, it is possible to describe the radiation coming from the disk itself as isotropic radiation from a black body. It is possible to compute the temperature related to this radiation by applying the Stefan-Boltzmann formula

$$\mathcal{F}(r) = \sigma T^{*4}, \qquad (12)$$

here the radiative flux, which is a function of radial distance and denoted by $\mathcal{F}(r)$ and σ is the Stefan-Boltzmann constant.

The differential luminosity $\frac{d\mathcal{L}_\infty}{d\ln r}$ can be calculated from the flux $\mathcal{F}$ using the following relationship

$$\frac{d\mathcal{L}_\infty}{d\ln r} = 4\pi r\sqrt{-g}E\mathcal{F}(r). \qquad (13)$$

Radiation released by the accretion disk at a certain distance r is described by the differential luminosity and the radiative flux. In real-world observations, the frequency and the spectral distribution are physically quantifiable variables and prove to be easier to measure.

The spectral luminosity $\mathcal{L}_{v,\infty}$ is defined as follows:

$$v\mathcal{L}_{v,\infty} =$$
$$= \frac{60}{\pi^3} \int_{r_{ISCO}}^{\infty} \frac{\sqrt{-g}E}{M_T^2} \frac{(u^t y)^4}{\exp[u^t y / \mathcal{F}^{*1/4}]-1} dr, \qquad (14)$$

here $y = hv/kT^*$, with h, k and v representing the Planck's constant, Boltzmann constant and frequency at which the radiation is emitted. Given the above, u^t can be defined as

$$u^t(r) = \frac{1}{\sqrt{-g_{tt} - 2\Omega g_{t\varphi} - \Omega^2 g_{\varphi\varphi}}}. \qquad (15)$$

Results and discussion

Figs. 7, 8 illustrate orbital angular velocity of the test particles $\Omega^*(r)$ versus normalized radial distance r/M. Fig. 7 displays the results for a rotating Bardeen BH with various values of $j = [0, 0.2, 0.4, 0.6, 0.8]$ at a fixed $r_0^* = 0.2$. In comparison to the static Bardeen spacetime (black solid color) with $j = 0.2$, the rotating Bardeen spacetime with the varying values of j at fixed $r_0^* = 0.2$ lead to a smaller angular velocity in all ranges of r. The Fig. 8 shows the results for different values of $r_0^* = [0, 0.25, 0.5, 0.75]$ at a fixed $j = 0.2$. The solid black curve indicates the Kerr metric. The angular

velocity in Kerr spacetime with $r_0^* =0$ at fixed j=0.2 is greater than the rotating Bardeen spacetime in all ranges of r.

In Figs. 9, 10 we depicted the dependence of L^* on the r/M for rotating Bardeen BHs with various values j at fixed $r_0^* =0.2$ (Fig. 9) and with various values of r_0^* at fixed $j = 0.2$ (Fig. 10).
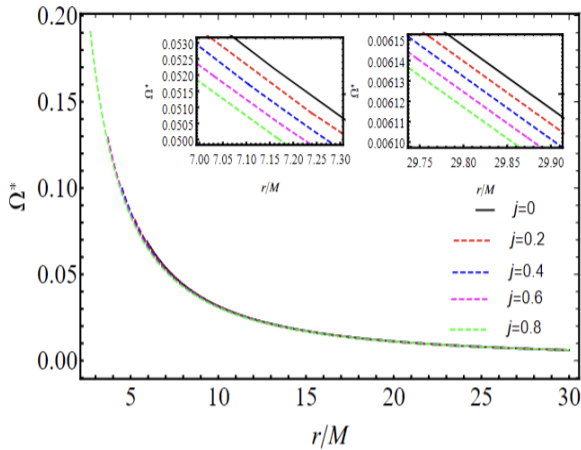
Figure 7 – Dependence of test particle's angular velocity on the radial distance r/M for rotating Bardeen BHs with $r_0^* =0.2$
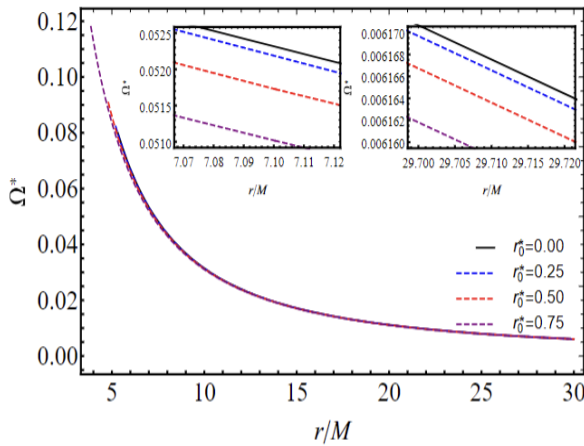
Figure 8 – Dependence of test particle's angular velocity on the radial distance r/M for rotating Bardeen BHs with $j = 0.2$
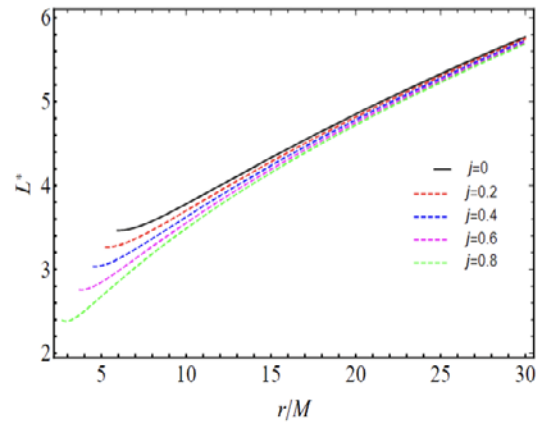
Figure 9 – L^* as a function of r/M for rotating Bardeen BHs with $r_0^* =0.2$
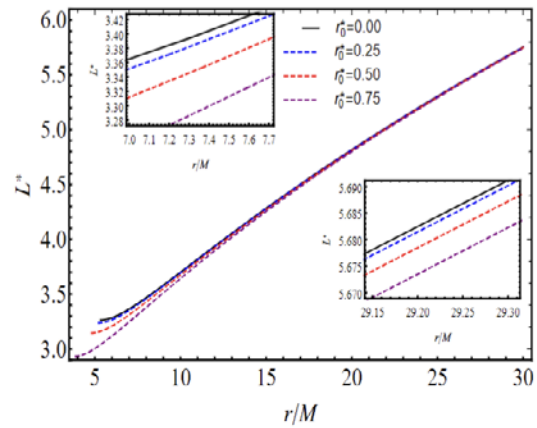
Figure 10 – L^* as a function of r/M for rotating Bardeen BHs with $j = 0.2$

In Figs. 11, 12 we constructed the dependence of E^* of test particles on the r/M for rotating Bardeen BHs with various values j at fixed $r_0^* =0.2$ (Fig. 11) and with various values of r_0^* at fixed $j = 0.2$ (Fig. 12).

As seen from Figs. 8, 10, 12 $\Omega^*(r)$, $L^*(r)$, E^* with varied values of r_0^* at fixed j are always less than the Kerr case (black solid curve). In Figs. 7, 9, 11 $\Omega^*(r)$, $L^*(r)$, E^* with different values of j at fixed r_0^* are always less than in case static Bardeen BH (black solid curve).
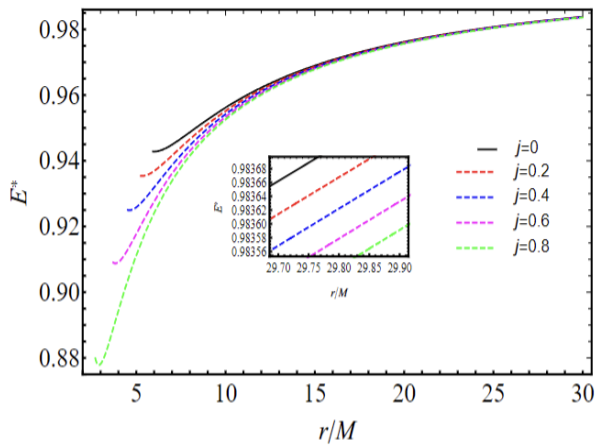
Figure 11 – E^* as a function of r/M
for rotating Bardeen BHs with $r_0^* = 0.2$
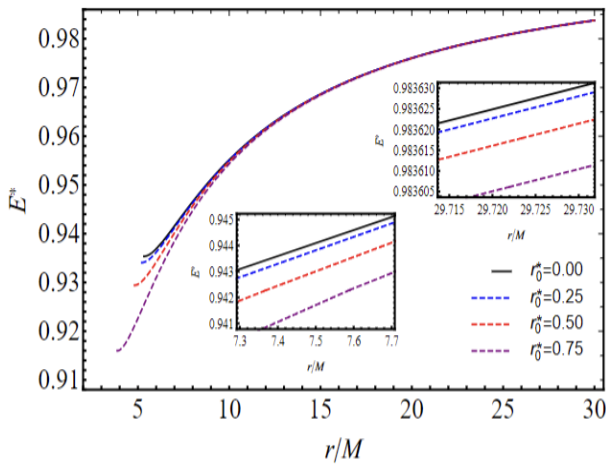
Figure 12 – E^* as a function of r/M
for rotating Bardeen BHs with $j = 0.2$

spinning Bardeen BHs ($r_0^* = 0.2, j = 0.2$) is greater than that in the static Bardeen spacetime case.
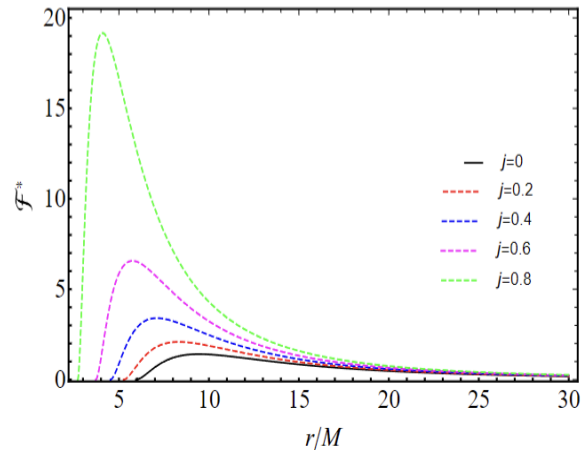
Figure 13 – Radiative flux F^* multiplied by 10^5
of the accretion disk versus normalized radial distance
r/M for rotating Bardeen BHs with $r_0^* = 0.2$
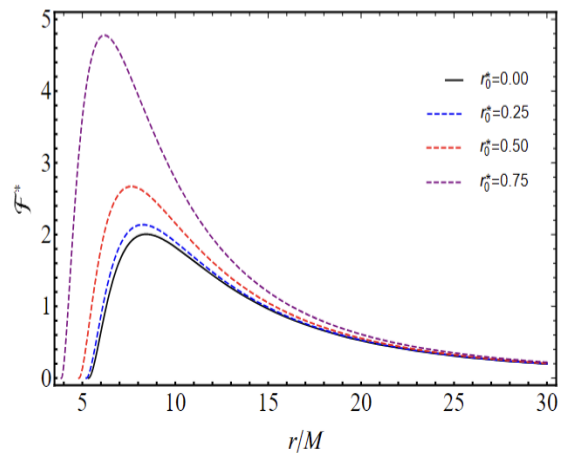
Figure 14 – Radiative flux F^* multiplied by 10^5
of the accretion disk versus normalized radial distance
r/M for rotating Bardeen BHs with $j = 0.2$

It is worth mentioning that we normalized the flow by dividing it by the total BH mass M in order to maintain the dimensionless argument of the exponential term. Furthermore, a new quantity $\mathcal{F}^*(r)$, is determined as: $\mathcal{F}^*(r) = M^2 \mathcal{F}(r)$. This normalization ensures that the flux is represented consistently in the computations that follow.

Figs. 13, 14 show the $\mathcal{F}(r)$ for the rotating Bardeen BHs. We left j arbitrary and set $r_0^* = 0.2$ (Fig. 13) and we fixed $j = 0.2$ and let r_0^* to vary (Fig. 14). The flux for the spinning Bardeen BHs with $j = 0.2$ and $r_0^* > 0$ is larger than in the Kerr metric case. The Fig. 13 illustrates how the flux grows in accordance with the chosen values of j. The $\mathcal{F}(r)$ for the

The dimensionless temperature T^* of accretion disks for spinning Bardeen BHs spacetime with $j = [0, 0.2, 0.4, 0.6, 0.8]$ at fixed $r_0^* = 0.2$ and $r_0^* = [0, 0.25, 0.5, 0.75]$ at fixed $j = 0.2$ is presented in Figs. 15 and 16, respectively. The temperature T^* for the rotating Bardeen spacetime is always larger than in the static Bardeen spacetime (Fig. 15). Fig. 16 illustrates that the temperature is permanently greater than in the Kerr spacetime for values of $r_0^* = [0.25, 0.5, 0.75]$.
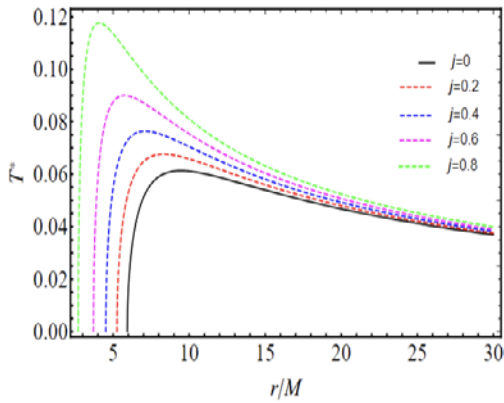
Figure 15 – The accretion disks' temperature T^* around the rotating Bardeen BHs with $r_0^* = 0.2$

Fig. 20, is smaller the whole ranges around the Kerr BHs with respect to the rotating Bardeen BHs.
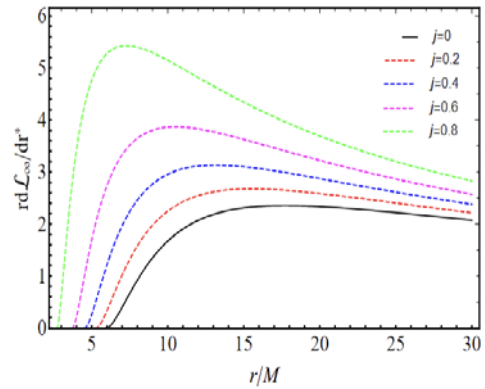
Figure 17 – The accretion disks' differential luminosity multiplied by 10^2 versus of r/M for rotating Bardeen BHs with $r_0^* = 0.2$

Figure 16 – The accretion disks' temperature T^* around the rotating Bardeen BHs with $j = 0.2$
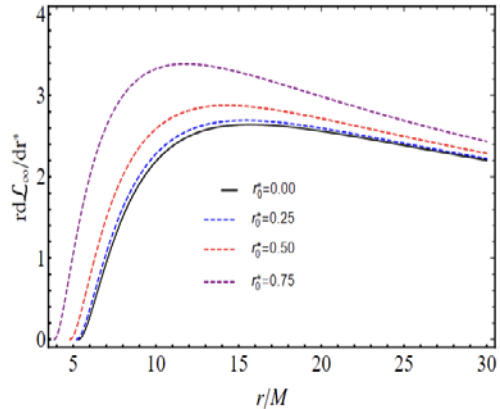
Figure 18 – The accretion disks' differential luminosity multiplied by 10^2 versus of r/M for rotating Bardeen BHs with $j = 0.2$

Differential luminosity versus the r/M for the rotating Bardeen BH with $j \geq 0$ at fixed $r_0^* = 0.2$ and $r_0^* \geq 0$ at fixed $j = 0.2$ is shown in Figs. 17 and 18, respectively. The behavior of the differential luminosity is similar to the radiative flux displayed in Figs. 13 and 14. It has to do with the fact that Eq. (13) relates both quantities.

The spectral luminosity $\mathcal{L}_{\nu,\infty}$, as determined by Eq. (14), is illustrated in Figs. 19 and 20 versus $h\nu/kT^*$ (as in previous cases, the fixed $r_0^* = 0.2$ (Fig.19), and fixed $j = 0.2$ (Fig. 20)). The effect of angular momentum is that the spectral luminosity at higher values of j is superior. A similar trend is observed in the case when the values of r_0^* increase for a fixed j. For both considered variations, the influence of rotation and length parameter is more evident with the growth of frequency at which the light is emitted. The spectral luminosity, as seen in

Figure 19 – Spectral luminosity versus the accretion disk's black-body emission frequency for rotating Bardeen BHs with $r_0^* = 0.2$
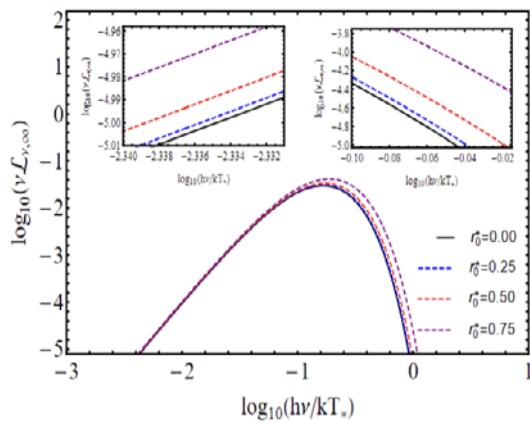
Figure 20 – Spectral luminosity versus the accretion disk's black-body emission frequency for rotating Bardeen BHs with $j = 0.2$

Final outlooks and perspectives

We used accretion disk luminosity to distinguish different types of spacetime that model BH or BH mimickers. Here, we investigated what kinds of effects are anticipated from rotating RBH solutions in the absence of a cosmological constant. We thus emphasized the capability of distinguishing rotating Bardeen BH from Kerr spacetime. For example, by analyzing the structure of horizons and values of r_{ISCO}, it is possible to show that the Kerr BHs are conceptually different from the Bardeen BHs.

The neutral test particle behaviors in the circular geodesics were calculated. Here we have explored the Novikov-Thorne-Page model of the thin accretion disk. Regarding this, we assessed the radius of ISCO, radiative flux, differential and spectral luminosities. Particularly, our results demonstrate that the luminosity for rotating Bardeen BHs is greater than for Kerr spacetime with fixed spin parameter $j = 0.2$. This peculiarity can serve as a means to differentiate between the two spacetimes.

The observed higher luminosity in the case of rotating Bardeen BHs suggests that these systems possess inherent characteristics that promote more efficient energy release and radiation emission compared to their Kerr counterparts at fixed $j = 0.2$. One plausible explanation for this phenomenon lies in the distinct nature of the spacetime geometry described by the Bardeen metric. Unlike Kerr spacetime, which is governed solely by the mass and spin of the black hole, the Bardeen metric incorporates additional parameter that can influence the gravitational dynamics near the BH.

Furthermore, the discrepancy in luminosity between Bardeen and Kerr BHs highlights the importance of considering alternative BH models beyond the traditional Kerr paradigm. It suggests that the specific geometric properties and underlying physics encoded in alternative BH metrics can significantly impact the observational signatures of accretion disks.

Lastly, we showed that there is the degeneracy in r_{ISCO} between the Bardeen and Kerr BHs. We explicitly demonstrated that the Bardeen metric can mimic the effects in the Kerr metric related to the r_{ISCO} up to the values of $j = 0.35$. Hence, this argument can also be used to distinguish the two spacetime.

It would be interesting to study radiative characteristics of other spacetimes in alternative, extended and modified theories of gravity. It is planned to consider this issue in future works.

Acknowledgments

References

1. The Event Horizon Telescope Collaboration "First M87 Event Horizon Telescope Results. I. The Shadow of the Supermassive Black Hole." *The Astrophysical Journal Letters* 875, No. 1 (2019): 1–17.
2. Akiyama K. et al. (Event Horizon Telescope) "First Sagittarius A* Event Horizon Telescope Results. I. The Shadow of the Supermassive Black Hole in the Center of the Milky Way." *The Astrophysical Journal Letters* 930, No. 2 (2022): 1–21.
3. Abbott B.P. et al. "Observation of gravitational waves from a binary black hole merger." *Physical Review Letters* 116, No. 6 (2016): 1–7.
4. Abbott B.P. et al. "GW151226: Observation of Gravitational Waves from a 22-Solar-Mass Binary Black Hole Coalescence." *Physical Review Letters* 116, No. 24. (2016): 1–14.
5. Dymnikova I. "Vacuum Nonsingular Black Hole." *General Relativity and Gravitation* 24, No. 3 (1992): 235–242.
6. Bronnikov K.A. "Regular magnetic black holes and monopoles from nonlinear electrodynamics." *Physical Review D* 63, No. 4 (2001): 1–6.

7.   Melgarejo G., Contreras E. and Bargueno P. "Regular black holes with exotic topologies." *Physics of the Dark Universe* 30, No. (2020): 1–7.

8.   Bambi C. "Regular Black Holes: Towards a New Paradigm of Gravitational Collapse" doi:10.48550/arXiv.2307.13249, 2307.13249.

9.   Lan C., Yang H., Guo Y. and Miao Y.-G. "Regular black holes: A short topic review." *International Journal of Theoretical Physics* 62, No. 9 (2023): 202–247.

10.   Sebastiani L. and Zerbini S. "Some remarks on non-singular spherically symmetric space-times." *Astronomy* 1, No. 2 (2022): 99–125.

11.   Bardeen J.M. "Non-singular general relativistic gravitational collapse." in *Proceedings of the International Conference GR5* 174, No. 1 (1968): 174.

12.   Bogojevic A. and Stojkovic D. "A Non-Singular Black Hole." *Physical Review D* 61, No. 8 (2000): 1–11.

13.   Toshmatov B., Ahmedov B., Abdujabbarov A. and Stuchlık, Z. "Rotating regular black hole solution." *Physical Review D* 89, No. 10 (2014): 1–8.

14.   Ghosh S.G., Maharaj S.D. "Radiating Kerr-like regular black hole" *European Physical Journal C* 75, No. 7 (2015): 1-7.

15.   Azreg-Aınou M. "Generating rotating regular black hole solutions without complexification." *Physical Review D* 90, No. 6 (2014): 1–13.

16.   Hayward S.A. "Formation and evaporation of non-singular black holes." *Physical Review Letters* 96, No. 3 (2006): 1–4.

17.   Bambi C. and Modesto L. "Rotating regular black holes." *Physics Letters B* 721, No. 4-5 (2013): 329–334.

18.   Akbarieh A.R., Khoshragbaf M. and Atazadeh, M. "Accretion disk around regular black holes." 10.48550/arXiv.2302.02784, (2023): 1–12.

19.   Boshkayev K., Konysbayev T., Kurmanov Ye., Luongo O., Muccino M., Taukenova A. and Urazalina A. "Luminosity of accretion disks around rotating regular black holes." *European Physical Journal C* 84, No. 3 (2024): 1–12.

20.   Boshkayev K., Konysbayev T., Kurmanov Ye., Luongo O., Muccino M., Quevedo H. and Urazalina A. "Accretion disk in the Hartle-Thorne spacetime." *European Physical Journal Plus,* 124, No. 273, (2024): 1–17.

21.   Ayon-Beato E. and Garcia A. "Regular Black Hole in General Relativity Coupled to Nonlinear Electrodynamics." *Physical Review Letters* 80, No. 23 (1997): 5056–5059.

22.   Bronnikov K.A. "Comment on "Regular Black Hole in General Relativity Coupled to Nonlinear Electrodynamics." *Physical Review Letters* 85, No. 21 (2000): 4641.

23.   Bronnikov K.A. "Regular black holes sourced by nonlinear electrodynamics." arXiv:2211.00743, (2022): 1–30.

24.   Ansoldi S. "Spherical black holes with regular center: a review of existing models including a recent realization with Gaussian sources." arXiv:0802.0330, (2008): 1–36.

25.   Li Q.-Q., Zhang Y., Li Q. and Sun Q. "Rotating Bardeen black hole surrounded by perfect fluid dark matter as a particle accelerator." *Communications in Theoretical Physics* 75, No. 10 (2023):1–10.

26.   Ghosh S.G. and Amir M. "Horizon structure of rotating Bardeen black hole and particle acceleration." *European Physical Journal C* 75, No. 11 (2015): 1 – 12.

27.   Boshkayev K., Gasperin E., Gutierrez-Pineres A.C., Quevedo H. and Toktarbay S. "Motion of test particles in the field of a naked singularity." *Physical Review D* 93, No. 2 (2016): 1–16.

28.   Boshkayev K., Konysbayev T., Kurmanov E., Luongo O., Malafarina D. and Quevedo H. "Luminosity of accretion disks in compact objects with a quadrupole." *Physical Review D* 104, No. 8 (2021): 1–10.

29.   Novikov I.D. and Thorne K.S. "Astrophysics of black holes." Black Holes (Les Astres Occlus), 343–350.

30.   Page D.N. and Thorne K.S. "Disk-Accretion onto a Black Hole. Time-Averaged Structure of Accretion Disk." *The Astrophysical Journal* 191, No. 2 (1974): 499–506.

Information about authors:

Kurmanov Yergali – PhD, Acting Associate Professor at Al-Farabi Kazakh National University, Almaty, Kazakhstan, e-mail: ergaly_90@mail.ru

Konysbayev Talgar – PhD at Al-Farabi Kazakh National University, Almaty, Kazakhstan, e-mail: talgar_777@mail.ru

Suliyeva Gulnara (corresponding author) – 2nd year doctoral student at the Department of Theoretical and Nuclear Physics at Al-Farabi Kazakh National University, Almaty, Kazakhstan, e-mail: g_suliyeva@mail.ru

Gulfeiruz Ikhsan – Junior Research Associate at National Nanotechnology Laboratory of Open Type, Almaty, Kazakhstan, e-mail: gulfeyruz.ihsan@mail.ru

Nazym Saiyp – 1st year master student at the Department of Solid State Physics and Nonlinear Physics at at Al-Farabi Kazakh National University, Almaty, Kazakhstan, e-mail: nazymsaiyp1@gmail.com

Guldana Rabigulova – 1st year master student at the Department of Solid State Physics and Nonlinear Physics at at Al-Farabi Kazakh National University, Almaty, Kazakhstan, e-mail: guldanaberikhanovna@gmail.com

Ainur Urazalina – PhD, Senior Lecturer at Al-Farabi Kazakh National University, Almaty, Kazakhstan, e-mail: y.a.a.707@mail.ru

A.L. Kozlovskiy[1,2],* , A.S. Seitbayev[1] ,
S.G. Giniyatova[1,2] , D.B. Borgekov[1,2] ,

[1]L.N. Gumilyov Eurasian National University, Astana, Kazakhstan
[2]The Institute of Nuclear Physics, Almaty, Kazakhstan
* e-mail: kozlovskiy.a@inp.kz

Determination of variation of compositions of (1-x)ZnO-0.25Al$_2$O$_3$-0.25WO$_3$-xBi$_2$O$_3$ glass-like ceramics on protective characteristics in gamma radiation shielding

Abstract. The work is devoted to the study of the effect of variation of the ratio of oxides in the composition of (1-x)ZnO-0.25Al$_2$O$_3$-0.25WO$_3$-xBi$_2$O$_3$ glass-like ceramics on shielding characteristics when employed as materials to mitigate the adverse effects of gamma radiation with different energy. The primary incentive behind these investigations is to discover novel protective shielding materials that lack lead or its oxide forms yet possess high shielding efficiency. Additionally, the aim is to identify the most promising compositions for potential practical applications in shielding. During the studies of shielding characteristics, it was observed that partial replacement of zinc oxide with bismuth oxide leads to a pronounced increase in shielding for low-energy gamma rays, for which, according to the data obtained, an increase in the concentration of bismuth oxide leads to an increase in the linear and mass coefficient by more than $0.8 - 1.2$ times. An analysis of the influence of variations in the ratio of zinc and bismuth oxides in the composition of glass-like ceramics on the shielding characteristics revealed that the replacement of zinc oxide with bismuth oxide, leading to an elevation in density of the order of $10 - 15$ %, leads to a steep rise in the shielding efficiency for low-energy gamma rays (more than 120 %), and to a $15 - 17$ % growth in shielding efficiency in the case of gamma-quanta shielding for which the main interaction mechanisms are the Compton effect and the formation of electron – positron pairs.
Key words: shielding materials, ionizing radiation, glass-like ceramics, absorption efficiency, oxide materials, gamma radiation.

Introduction

In recent years, attention towards the advancement of new shielding materials has been directed towards research exploring technological solutions aimed at creating composite vitreous ceramics or amorphous glasses, which are based on oxide components combining heavy, rare earth and light elements [1-4]. Simultaneously, significant focus is dedicated to investigating variations in the compositions of these oxides. Altering these compositions enables the creation of numerous shielding materials with promising potential in the field of shielding [5,6]. These studies are based on the principle of obtaining the densest ceramics or glasses, comparable in shielding efficiency to traditional material in the form of lead, but at the same time possessing transparency (for medical use

in cases where direct visualization of exposure to ionizing radiation is necessary), non-toxicity, high strength parameters (hardness and crack resistance), as well as low cost [7-9]. Also, much attention in such studies is paid to the search for a simple method for producing protective materials, the creation of which eliminates the need to use high-tech processes. In most cases, the method of producing such protective materials is considered to be solid-phase chemical synthesis combined with thermal sintering, the conditions of which are selected to create an amorphous structure of ceramics or initiate glass transition processes [11-14]. Also, the use of this synthesis method makes it possible to expand the range of materials obtained by varying the molar or weight ratios of the components used for the synthesis of samples, which opens up great prospects in this area of research.

The aim of this study is to assess the efficacy of using $(1-x)ZnO-0.25Al_2O_3-0.25WO_3-xBi_2O_3$ glassy ceramics as shielding materials against gamma and electron radiation, while also investigating the impact of composition variations on shielding characteristics. The interest in this research area stems mainly from the broadening scope of protective ceramic and glassy ceramic materials utilized for ionizing radiation shielding. Moreover, there is potential for their application as transparent materials for direct visualization or observation of ionizing radiation objects. The use of aluminum and bismuth oxides is due to the possibility of enhancing the resistance of the synthesized samples to external factors, including mechanical influences. Thus, in [15], it was demonstrated that the addition of aluminum and bismuth oxides to the $ZnO–Al_2O_3–Bi_2O_3–B_2O_3$ composition leads to an increase in the Young's modulus and, therefore, the crack resistance of glasses under external influences. The use of bismuth oxide is also due to the possibility of stabilizing and compacting glasses during their thermal sintering since this oxide is one of the stabilizers for glass transition processes. Also, the replacement of zinc oxide with bismuth oxide leads to an increase in the density of the synthesized samples, due to differences in the density of the oxides (p_{ZnO} – 5.61 g/cm^3, p_{Bi2O3} – 8.9 g/cm^3).

Materials and research methods

The objects of study were $(1-x)ZnO-0.25Al_2O_3-0.25WO_3-xBi_2O_3$ glass-like ceramics obtained by solid-phase synthesis. The manufacturing method included mechanical grinding of the original ZnO, Al_2O_3, WO_3 and Bi_2O_3 oxides in a given molar ratio. The ratio of zinc oxide and bismuth oxide varied in the x range from 0.05 to 0.25 M, which allowed the production of glass-like ceramics with different element ratios. The combination of the method of mechanochemical solid-phase synthesis with thermal annealing of ground mixtures made it possible to obtain a series of samples that have different shielding characteristics. The choice of this method is based on the possibility of obtaining ceramics and glasses with a controlled ratio of elements, as well as those that are highly resistant to external mechanical influences.

The oxides ZnO, Al_2O_3, WO_3 and Bi_2O_3 purchased from Sigma Aldrich (Sigma, USA) were chosen as the starting components; the chemical purity of the powders under study was 99.95%.

Mechanical grinding was carried out in a planetary mill PULVERISETTE 6 (Fritsch, Berlin, Germany) at a grinding speed of about 400 rpm for 1 hour. The grinding time and the grinding speed were chosen to avoid the cold welding effect of grinding powders under the action of mechanical deformation caused by the action of grinding bodies. Grinding was carried out in a ratio of 1 to 3 by the mass of ground powder and grinding bodies in the form of tungsten carbide balls with a diameter of 10 mm. Grinding was carried out in a glass made of tungsten carbide, the hardness of which eliminates the effect of contamination of the grinded powders with impurities. Grinding resulted in powders that were uniform in composition and grain size, which were later used in thermal sintering. After grinding, the resulting mixtures were annealed in a Nabertherm LE 4/11/R6 muffle furnace (Nabertherm, Lilienthal, Germany) at a temperature of 1500 °C for 5 hours at a heating rate of 20 °C/min. Annealing was carried out in zirconium dioxide crucibles capable of withstanding temperatures of about 2000 °C. The samples were cooled together with the furnace for 24 hours after reaching the annealing time. The choice of cooling time is determined by the need to comply with the technical rules for operating muffle furnaces, according to which access to the atmosphere can be allowed until the heating elements have completely cooled.

The choice of these synthesis conditions made it possible to achieve the initialization of the amorphization processes of the studied samples during the glass transition process, which was confirmed by X-ray phase analysis data, according to which no significant reflections characteristic of ordered structures were recorded in the X-ray diffraction patterns.

At the same time, the variation was carried out by partially replacing zinc oxide with bismuth oxide, the choice of which is due to the possibility of plasticization during glass formation in the case of thermal melting of the initial components, as well as increasing the shielding efficiency due to the larger atomic mass, while maintaining the optical transparency due to zinc oxide. The range of substitution concentrations was from 0.05 to 0.25 M. At the same time, the substitution was carried out by varying zinc oxides (its decrease) and bismuth oxide (its increase), with a constant ratio of the molar fractions of aluminum oxide and tungsten oxide. Previously, in [16], it was shown that thermal annealing in the temperature range from 500 to 1100 °C leads to the formation of multiphase ceramics, the

formation of which occurs due to phase formation processes associated with thermodynamic reactions of the synthesis of complex oxides. Moreover, it was determined a priori, considering the data presented in the work, that thermal annealing at a temperature of 1500°C leads to the formation of amorphous glass-like ceramics with fairly high strength parameters (hardness of 1000 – 1100 HV). Figure 1 reveals the results of X-ray diffraction of the studied samples of glassy ceramics, reflecting the amorphous nature of the obtained samples after thermal annealing under specified conditions.
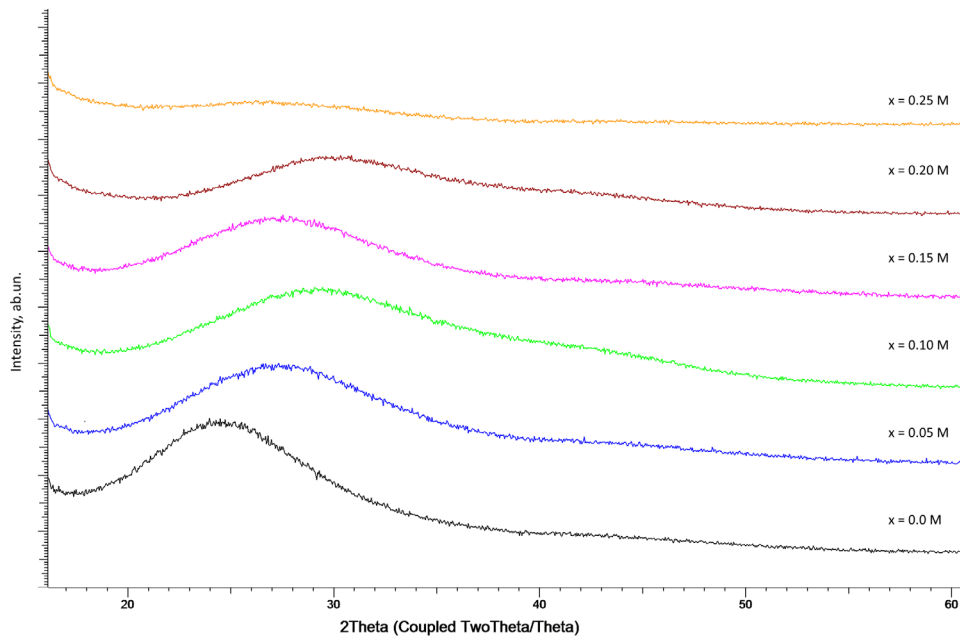
Figure 1 – X-ray diffraction results reflecting the amorphous nature
of the studied samples of $(1-x)ZnO-0.25Al_2O_3-0.25WO_3-xBi_2O_3$ glass-like ceramics

Determination of the shielding characteristics of the synthesized samples depending on variations in their composition was carried out by conducting serial experiments related to determining the intensity of gamma radiation before and after the use of a protective shield in the form of synthesized samples using three standard sources of ionizing radiation Co^{57} (130 keV), Cs^{137} (660 keV), Na^{22} (1270 keV). The determination of effectiveness was assessed by calculating the linear and mass attenuation coefficients (LAC and MAC), as well as the half-attenuation layer value (HVL), which is used to conduct a comparative analysis of the shielding effectiveness of different materials of different compositions. The shielding scheme was chosen in the form of a source placed in a lead container with a 10 mm hole, near which at a distance of 10 cm a protective shield made of synthesized glassy ceramics is placed, behind which a detector is placed to record the intensity of the transmitted ionizing radiation.

Simulation of the interaction processes of gamma radiation with composite ceramic compositions, varying in their molar composition, were simulated using the XCOM program code. A detailed description of the use of program code for modeling the processes of interaction of gamma radiation with materials is presented in works [17-19]. Figure 2 illustrates the variations in the MAC value for specific compositions, depending on the zinc and bismuth oxide ratio. The values, ranging from 0.001 to 10 MeV, encompass all three primary mechanisms of gamma radiation interaction with matter (Compton effect, photoelectric effect, and electron-positron pair formation). As evident from the provided data, altering the ratio of oxide components within the selected system does not result in discernible changes in the relationship between variations in the MAC value and gamma ray energy. The overall trend corresponds to the generally accepted theory of describing alterations

in shielding efficiency. In the case of low energies of gamma rays (about 0.01 MeV), the shielding efficiency has maximum values, while an elevation in the gamma quanta energy results in an exponential decrease in the shielding efficiency, due to the dominance of the mechanisms of formation of electron-positron pairs, as well as secondary radiation in the form of gamma quanta of lower energies during the interaction of high-energy gamma quanta with the target structure.
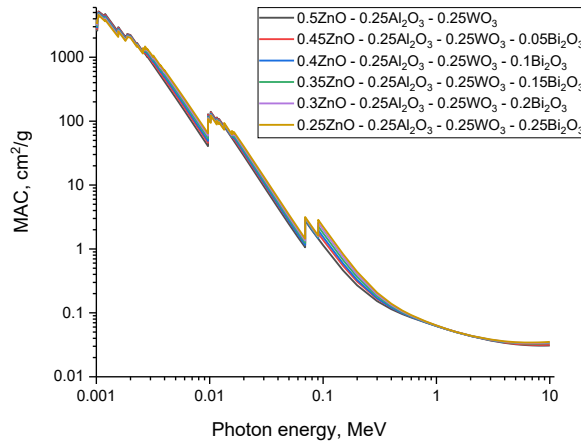
Figure 2 – Simulation results of the dependence of MAC on gamma radiation energy obtained using the XCOM code

It is worth to highlight that the partial replacement of zinc oxide with bismuth oxide causes changes in the shielding efficiency in the region of low energies of gamma rays (of the order of $0.3 - 0.6$ MeV), for which the dominant interaction processes are photoelectric mechanisms, for which the dependence on the charge number of the composite material is most clearly visible.

Results and discussion

Figure 3 presents the results of a comparative analysis of MAC values obtained by modeling in the XCOM program code (values taken for specific gamma ray energies characteristic of those emitted by sources used in shielding experiments) and experimental values, obtained by shielding of gamma quanta emitted by various sources. According to the general assessment of the comparison of theoretical and experimental MAC values, there is a good agreement between the simulation results and experimental values, and the difference in values is no more than $3 - 5$ %, which can be explained by several factors. Firstly, the higher MAC values obtained experimentally may be due to the fact that when modeling interaction processes, the objects under study were specified as a composite in the form of oxide compounds with different weight contributions. At the same time, according to the data of [16], during thermal sintering of these composites at temperatures above 900 °C, complex oxides are formed in the form of zinc tungstates ($ZnWO_4$) and bismuth (Bi_2WO_6), as well as spinel $ZnAl_2O_4$, the presence of which causes a change in density that is different from the density of composites consisting of oxides. In this case, at high annealing temperatures (1500 °C), according to X-ray diffraction data, the composition of the obtained samples is represented by amorphous structures, however, the possibility of the presence of fine grains in the form of complex tungstate compounds in the amorphous matrix cannot be excluded, since these compounds are thermally stable at fairly high temperatures. Secondly, the most pronounced differences are observed for samples in which the bismuth oxide content is on the order of $0.2 - 0.25$ M, which indicates that changes in MAC values may also be due to differences in the charge number, the change of which is due to the high bismuth content in the composition.
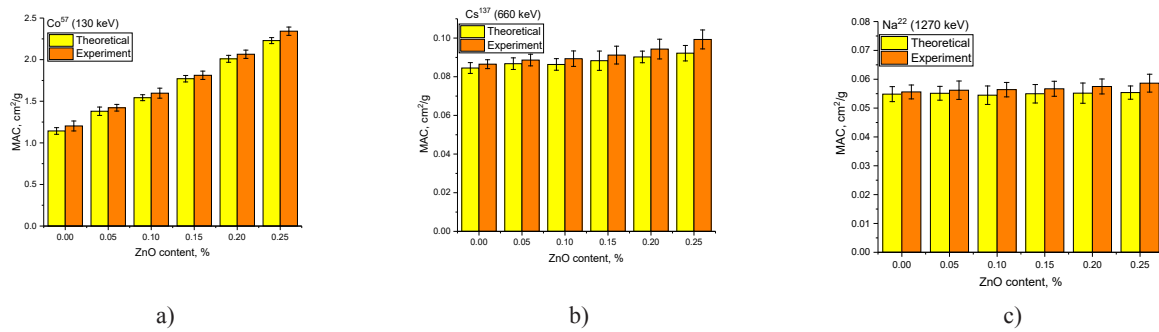
Figure 3 – Comparative analysis of MAC values calculated using
the XCOM code and experimentally obtained values during shielding experiments

The alterations in the LAC value presented in Figure 4 depending on the energy of gamma quanta reflect the influence of variations in the ratio of components on the efficiency of attenuation of gamma radiation during shielding. The most pronounced changes are observed when shielding low-energy gamma quanta emitted by the Co^{57} source (130 keV). In this case, changing the ratio of the components of zinc and bismuth oxides leads to a more than twofold increase in the shielding efficiency, expressed by an increase in LAC from 6.2 cm^{-1} for samples $0.5ZnO - 0.25Al_2O_3 - 0.25WO_3$ to 12.7 – 14.2 cm^{-1}, for samples in which the Bi_2O_3 concentration is 0.2 – 0.25 M. In this case, the shielding efficiency can be assessed at a fairly high level, taking into account the fact that the obtained values have a good correlation with the MAS data obtained using the simulation method. In the case of shielding of gamma rays with energies of 660 keV and 1270 keV, the differences in efficiency are reduced, however, the addition of bismuth oxide to the composition results in a rise in the shielding efficiency of the order of 20 – 25 % in comparison with the composition of $0.5ZnO - 0.25Al_2O_3 - 0.25WO_3$ glass-like ceramics.
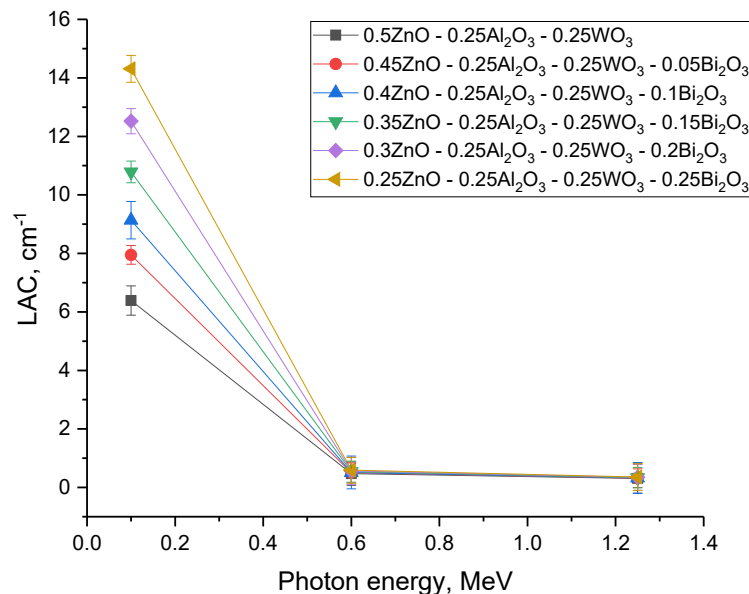
Figure 4 – Dependence of the LAC value for the studied $(1-x)ZnO-0.25Al_2O_3-0.25WO_3-xBi_2O_3$
glass-like ceramics depending on the gamma quanta energy

Figure 5 demonstrates the results of a comparative analysis of the relationship between changes in the LAC value and the density of the samples under study, which is due to variations in the ratio of oxides in the composition of glass-like ceramics. The density of the samples, due to their X-ray amorphism, was determined by the Archimedes method, according to which it was found that partial replacement of zinc oxide with bismuth oxide results in compaction of glass-like ceramics, which is due to the fact that the density of bismuth oxide is higher than that of zinc oxide (data on the densities of zinc and bismuth oxides are given in the Introduction section when describing the formulation of the problem and the relevance of the study).

As can be seen from the data presented, the greatest contribution to the change in shielding efficiency is made by the change in the density of the samples under study on the shielding of low-energy gamma quanta with an energy of 130 keV. At the same time, a change in the density of the samples by 14.5 % (at a bismuth oxide concentration of 0.25 M) shielding efficiency, according to comparison of LAC values, is about 1.2 – 1.25 times in comparison with the results obtained for samples that do not contain bismuth oxide. In the case of gamma rays with energies of 600 keV and 1270 keV, the change in shielding efficiency is less pronounced depending on the density of the samples and is about 25 and 17 %, respectively, at a bismuth oxide concentration of 0.25 M.
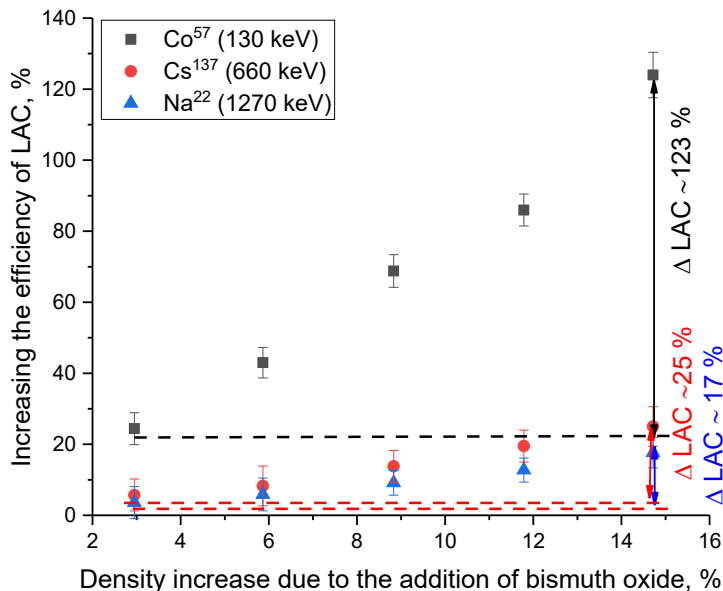
Figure 5 – Results of a comparative analysis of the dependence of LAC
for synthesized ceramics depending on changes in density
with increasing bismuth oxide content in the glass composition

A comparison of the shielding efficiency of synthesized samples with other types of samples, data on the shielding characteristics of which were taken from works [20 – 24], was carried out by comparing the HVL value obtained for gamma quanta with an energy of 660 keV. The choice of this energy of gamma quanta for comparison is due to the possibility of determining two types of processes of interaction of gamma quanta with materials (Compton effect and photoelectric effect), which are the most common interaction processes,

with the exception of the processes of formation of electron – positron pairs, characteristic of high-energy gamma quanta with energies of more than 1.0 – 1.5 MeV. For comparison, Pb_3O_4-SiO_2-ZnO-WO_3 (LAC ~ 0.728 cm^{-1} to 0.856 cm^{-1} depending on WO_3 concentration) [20], Al_2O_3-PbO-B_2O_3-WO_3 glass [21], B_2O_3–$SrCO_3$–TeO_2–ZnO glass [22], as well as two types of commercial materials considered as shielding protective materials were chosen. The choice of ferrite and telluride glasses as commercial materials is due to their prospects for use as protective

shielding materials, which are determined by their structural features, as well as several other unique properties, the combination of which allows us to consider them as one of the most promising materials for shielding. For example, in [23,24] it is shown that the combination of magnetic, structural, and antibacterial properties of ferrite nanoparticles and nanocrystals opens up great prospects for this class of materials when used as protective shields, which can also be used in the medical field, which uses sources of ionizing radiation. The results of the comparative analysis are presented in Figure 6.
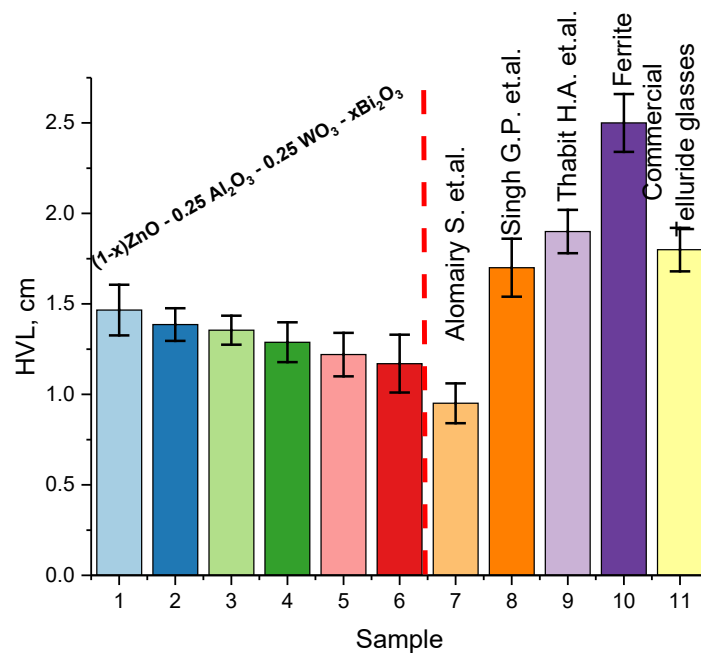
Figure 6 – Results of a comparative analysis of the HVL value of synthesized samples of (1-x)ZnO-0.25Al$_2$O$_3$-0.25WO$_3$-xBi$_2$O$_3$ glass-like ceramics and commercial samples (HVL data taken for gamma quanta energy of 660 keV)

As can be seen from the presented data on changes in the HVL value depending on changes in the ratio of the components of zinc and bismuth oxides, an increase in the bismuth oxide content leads to a decrease in the HVL value, which indicates an increase in shielding efficiency, as well as the possibility of using less thick glass-like ceramics for protection, which makes it possible to reduce weight and overall dimensions. In comparison with commercial samples of ferrite and telluride glasses, the efficiency is more than 1.5 – 2 times, which indicates that the use of the proposed compositions of glass-like ceramics is more promising in comparison with these types of samples, as well as the compositions proposed in [21,22]. In comparison with samples of Pb$_3$O$_4$-SiO$_2$-ZnO-WO$_3$ glasses, the proposed compositions of glass-like ceramics are inferior in efficiency, however, the use of lead oxide in the proposed glass compositions from [20] imposes certain restrictions associated with the toxicity of lead (part of the oxide), which narrows the scope of application of these glasses, and high efficiency indicators are due to the presence of heavy elements in the form of lead and bismuth.

Conclusion

During comparative analysis of the MAC values obtained using the XCOM program code and the experimentally obtained values during shielding, it was found that the difference between the theoretical and experimental values is no more than 3 – 5 %, which indicates good convergence, as well as the possibility of using computational codes to simulate the shielding of complex ceramic compositions. At the same time, differences in values may be due to the effects of structural features that arise during the synthesis of (1-x)ZnO-0.25Al$_2$O$_3$-0.25WO$_3$-xBi$_2$O$_3$ glass-like ceramics, leading to denser ceramics,

with the possible formation of inclusions in the form of complex oxides, observed at lower sintering temperatures of these compositions.

A comparative analysis of shielding efficiency by comparing HVL values with the results of other studies, as well as with data obtained for commercial samples, showed that the use of $(1-x)ZnO-0.25Al_2O_3-0.25WO_3-xBi_2O_3$ glass-like ceramics is quite effective in comparison with the majority of the considered shielding material compositions having similar components, as well as with commercial samples. Moreover, a rise in the concentration of bismuth oxide in the composition results in a decline in the HVL value from 1.466 cm for samples not containing bismuth oxide to 1.7 – 1.2 cm for bismuth oxide concentrations equal to 0.2 – 0.25 M. Compared to commercially available materials, ferrite and telluride glasses, the shielding efficiency is more than 1.5 – 2 times.

Acknowledgments

References

1. AbuAlRoos N. J., Amin N. A. B., Zainon R. Conventional and new lead-free radiation shielding materials for radiation protection in nuclear medicine: A review. *Radiation Physics and Chemistry*. 165 (2019) 108439.

2. More C. V., Alsayed Z., Badawi M. S., Thabet A. A., Pawar P. P. Polymeric composite materials for radiation shielding: a review. *Environmental chemistry letters*. 19 (2021) 2057-2090.

3. McCaffrey J. P., Mainegra□Hing E., Shen H. Optimizing non□Pb radiation shielding materials using bilayers. *Medical physics*. 36(12) (2009) 5586-5594.

4. Yue K., Luo W., Dong X., Wang C., Wu G., Jiang M., Zha Y. A new lead-free radiation shielding material for radiotherapy. *Radiation protection dosimetry*. 133(4) (2009) 256-260.

5. Shultis J. K., Faw R. E. Radiation shielding. *Nuclear Energy: Selected Entries from the Encyclopedia of Sustainability Science and Technology. New York, NY : Springer New York* (2012) 389-425.

6. Elsafi M., El-Nahal M. A., Sayyed M. I., Saleh I. H., Abbas M. I. Effect of bulk and nanoparticle Bi2O3 on attenuation capability of radiation shielding glass. *Ceramics International*. 47(14) (2021) 19651-19658.

7. Mhareb M. H. A., Alajerami Y. S. M., Sayyed M. I., Dwaikat N., Alqahtani M., Alshahri F., Al-Dhafar S. I. Radiation shielding, structural, physical, and optical properties for a series of borosilicate glass. *Journal of Non-Crystalline Solids*. 550 (2020) 120360.

8. Al-Harbi N., Sayyed M. I., Al-Hadeethi Y., Kumar A., Elsafi M., Mahmoud K. A., Bradley D. A. A novel CaO–K2O–Na2O–P2O5 glass systems for radiation shielding applications. *Radiation Physics and Chemistry*. *188* (2021) 109645.

9. Issa S. A., Saddeek Y. B., Sayyed M. I., Tekin H. O., Kilicoglu O. Radiation shielding features using MCNPX code and mechanical properties of the PbONa2OB2O3CaOAl2O3SiO2 glass systems. *Composites Part B: Engineering*. 167 (2019) 231-240.

10. Halimah M. K., Azuraida A., Ishak M., Hasnimulyati L. Influence of bismuth oxide on gamma radiation shielding properties of boro-tellurite glass. *Journal of non-crystalline solids*. 512 (2019) 140-147.

11. Kamislioglu M. Research on the effects of bismuth borate glass system on nuclear radiation shielding parameters. *Results in Physics*. 22 (2021) 103844.

12. Cheewasukhanont W., Limkitjaroenporn P., Kothan S., Kedkaew C., Kaewkhao J. The effect of particle size on radiation shielding properties for bismuth borosilicate glass. *Radiation Physics and Chemistry*. 172 (2020) 108791.

13. Alalawi A., Al-Buriahi M. S., Sayyed M. I., Akyildirim H., Arslan H., Zaid M. H. M., Tonguç B. T. Influence of lead and zinc oxides on the radiation shielding properties of tellurite glass systems. *Ceramics International*. 46(11) 17300-17306.

14. Al-Buriahi M. S., Bakhsh E. M., Tonguc B., Khan S. B. Mechanical and radiation shielding properties of tellurite glasses doped with ZnO and NiO. *Ceramics International*. 46(11) (2020) 19078-19083.

15. Zaid M. H. M., Matori K. A., Nazrin S. N., Azlan M. N., Hisam R., Iskandar S. M., Sayyed M. I. Synthesis, mechanical characterization and photon radiation shielding properties of ZnO–Al2O3–Bi2O3–B2O3 glass system. *Optical Materials*. *122* (2021) 111640.

16. Seitbayev A. S., Kozlovskiy A. L., Borgekov D. B., Zdorovets M. V. Study of the Phase Formation Processes and Their Influence on the Change in the Optical and Shielding Characteristics of 0.25 ZnO–0.25 Al2O3–0.25 WO3–0.25 Bi2O3 Ceramics. *Ceramics*. *6*(2) (2023) 798-817.

17. Shirmardi S. P., Shamsaei M., Naserpour M. Comparison of photon attenuation coefficients of various barite concretes and lead by MCNP code, XCOM and experimental data. *Annals of Nuclear Energy*. 55 (2013) 288-291.

18. Dong M. G., Sayyed M. I., Lakshminarayana G., Ersundu M. Ç., Ersundu A. E., Nayar P., Mahdi M. A. Investigation of gamma radiation shielding properties of lithium zinc bismuth borate glasses using XCOM program and MCNP5 code. *Journal of Non-Crystalline Solids*. 468 (2017) 12-16.

19. Sayyed M. I., Khattari Z. Y., Kumar A., Al-Jundi J., Dong M. G., & AlZaatreh M. Y. Radiation shielding parameters of BaO–Nb2O5–P2O5 glass system using MCNP5 code and XCOM software. *Materials Research Express*. 5(11) (2018) 115203.

17. Alomairy S., Alrowaili Z. A., Kebaili I., Wahab E. A., Mutuwong C., Al-Buriahi M. S., Shaaban K. S. Synthesis of Pb3O4-SiO2-ZnO-WO3 glasses and their fundamental properties for gamma shielding applications. *Silicon*. 14(10) (2022) 5661-5671.

18. Singh G. P., Singh J., Kaur P., Kaur S., Arora D., Kaur R., Singh D. P. Analysis of enhancement in gamma ray shielding proficiency by adding WO3 in Al2O3-PbO-B2O3 glasses using Phy-X/PSD. *Journal of Materials Research and Technology*. 9(6) (2020) 14425-14442.

19. Thabit H. A., Sayyed M. I., Hashim S., Abdullahi I., Elsafi M., Keshavamurthy K., Jagannath G. Optical, thermal and gamma ray attenuation characteristics of tungsten oxide modified: B2O3–SrCO3–TeO2–ZnO glass series. *Nuclear Engineering and Technology*. 56(1) (2024) 247-256.

20. Lokhande R. M., Vinayak V., Mukhamale S. V., Khirade P. P. Gamma radiation shielding characteristics of various spinel ferrite nanocrystals: a combined experimental and theoretical investigation. *RSC advances*, 11(14) (2021) 7925-7937.

21. Reddy B. C., Manjunatha H. C., Vidya Y. S., Sridhar K. N., Pasha U. M., Seenappa L., Gupta P. D. Synthesis and characterization of multi functional nickel ferrite nano-particles for X-ray/gamma radiation shielding, display and antimicrobial applications. *Journal of Physics and Chemistry of Solids*. 159 (2021) 110260.

Information about authors:

Seitbayev Aibek S. – PhD, Researcher at the Laboratory of Engineering Profile, L.N. Gumilyov Eurasian National University (Astana, Kazakhstan) e-mail: seitbayevaibek@gmail.com

Kozlovskiy Artem (corresponding author)- PhD, Head of the Laboratory of Solid State Physics, Astana Branch of the Institute of Nuclear Physics of the Ministry of Energy of the Republic of Kazakhstan (Almaty, Kazakhstan) e-mail: kozlovskiy.a@inp.kz

Borgekov Daryn B. – PhD, Researcher at the Laboratory of Engineering Profile, L.N. Gumilyov Eurasian National University (Astana, Kazakhstan) e-mail: borgekov@inp.kz

Giniyatova Sholpan G. – PhD., associate professor, teacher-researcher, L.N. Gumilyov Eurasian National University (Astana, Kazakhstan) e-mail: giniyatsholpan@gmail.com

B.A. Kyrykbay[*1] , A.R. Abdirakhmanov[2] , S.S. Ussenkhan[1] ,

A.U. Utegenov[1,2] , Y.Yerlanuly[1] , T.S. Ramazanov[2] ,

T.B. Koshtybayev[3] and S. A. Orazbayev[1,2]

[1]Institute of Applied Sciences and Information Technologies, Almaty, Kazakhstan
[2]Al-Farabi Kazakh National University, Almaty, Kazakhstan
[3]Kazakh National Women's Teacher Training University, Almaty, Kazakhstan
*e-mail: baglankyrykbaj44@gmail.com

Obtaining hydrophobic coatings from AR+HMDSO u
sing radiofrequency discharge at atmospheric pressure

Abstract. Hydrophobic coatings have attracted much attention due to their wide applications in various industries including electronics, textiles, and automotive. This study deals with the process of creating nanoscale coatings on a substrate achieved by plasma polymerization using plasma flow (jet) using radiofrequency discharge together with the precursor c6h18osi2 and the carrier gas Ar. In this work, we investigate the production of hydrophobic coatings using radiofrequency (RF) discharge at atmospheric pressure using a mixture of argon (Ar) and hexamethyldisiloxane (HMDSO). RF discharge is a versatile and efficient method of plasma generation that allows the deposition of thin films with defined properties. Here we investigate the influence of process parameters such as gas flow rate, discharge power, and substrate temperature on the morphology, chemistry, and hydrophobicity of the deposited coatings. The formation of these coatings was carefully studied under atmospheric pressure conditions, varying the number of cycles of experiments while maintaining optimal plasma parameters. The properties and elemental composition of the coatings were thoroughly studied using scanning electron microscopy (SEM) and energy dispersion spectroscopy (EDS). In addition, the obtained coatings were found to possess hydrophobic properties. The hydrophobicity of these coatings was evaluated by measuring the contact angle with a goniometer with respect to cycles of experiments and long-term durability. This study contributes to a better understanding of the synthesis, structure, and hydrophobic characteristics of nanoscale coatings, opening promising perspectives for various applications. The results show that the hydrophobicity of the coatings can be optimized by tuning the process parameters, resulting in coatings with water contact angles greater than 160 degrees. Additionally, the durability and stability of the hydrophobic coatings are evaluated under different environmental conditions, allowing an assessment of their potential for practical applications.
Key words: plasma polymerization, atmospheric pressure, superhydrophobic coatings.

Introduction

Hydrophobic coatings, which repel water due to their low surface energy, find wide applications in various industries ranging from electronics to textiles [1], automotive [2], and medical devices [3]. Among the methods for producing hydrophobic coatings, the radiofrequency (RF) discharge at atmospheric pressure offers a promising avenue [4]. This technique involves the deposition of hydrophobic coatings from a precursor gas mixture of argon (Ar) and hexamethyldisiloxane (HMDSO) under the influence of RF discharge. The use of RF discharge at atmospheric pressure presents several advantages over conventional methods such as chemical vapor deposition (CVD) [5] and plasma-enhanced chemical vapor deposition (PECVD) [6]. Firstly, operating at atmospheric pressure eliminates the need for vacuum systems, simplifying the setup and reducing production costs. Secondly, the RF discharge process allows for precise control over the deposition parameters, resulting in coatings with tailored properties [7.8].

Certain techniques, such as acquiring coatings through chemical processes and under atmospheric pressure, offer superior cost efficiency and enhanced efficacy for large-scale manufacturing. Through the utilization of chemical procedures, it is possible

to procure hydrophobic and superhydrophobic coatings characterized by exceptional stability [9]. Nonetheless, the chemical approach for obtaining superhydrophobic coatings necessitates the use of hazardous liquids and diverse solvents, presenting a notable drawback that can endanger human health and the environment. Moreover, the aforementioned techniques entail multiple stages for achieving superhydrophobic coatings, rendering the process of uniformly dispersing coatings intricate and time-intensive. Hence, the imperative of employing economical and eco-friendly methods across expansive surfaces emerges as a pressing concern.

Hydrophobic coatings obtained from Ar+HMDSO using RF discharge exhibit excellent water-repellent properties, making them suitable for applications requiring protection against moisture [10], corrosion [11], and fouling [12]. These coatings demonstrate high durability [13], thermal stability [14], and chemical resistance [15], making them ideal for outdoor and harsh environment applications [16.17].

We delve into the mechanisms underlying the formation of hydrophobic coatings through RF discharge at atmospheric pressure using Ar+HMDSO precursor gas mixture. We explore the influence of process parameters such as gas composition, discharge power, and substrate temperature on the properties of the resulting coatings. Additionally, we highlight the potential applications and future prospects of these hydrophobic coatings in various industries.

The results obtained may be of significant practical importance for the development of new materials with improved characteristics and expansion of their application area.

Experimental section

The scheme of an experimental installation aimed at studying the coating obtained using a plasma jet based on RF discharge at atmospheric pressure is shown in Figure 1. The plasma flux (jet) was generated using an RF generator between a copper wire wrapped in quartz glass and a grounded copper plate. Glass tube length: 100mm, inner diameter: 3mm and outer diameter: 10mm. Seren-R 301 with a high frequency of 13.56 MHz was used as a power source. Inert gas Ar and precursors HMDSO were used as the main gas flow. HMDSO is in liquid form at room temperature and therefore has a small volume poured into a barbotter. The flow of the prequels is controlled by the mass flow controller. The resulting coating samples settle on a glass substrate measuring

2x2 centimetre. Before starting the experiment, glass samples used as substrates are cleaned in an ultrasonic bath for 10 minutes. First, the concentration of gas mixtures Ar and HMDSO is sent to the quartz glass tube, and then, when a high-frequency voltage is applied to the electrode located outside the tube, atmospheric pressure plasma ignition occurs. As a result of coagulation of atoms in a plasma medium, the process of chemical reactions takes place, at a certain moment of time the coating grows to the nanoscale [10]. The experiment was carried out for the following parameters of the plasma: power magnitude 100-200 Watts, HMDSO/Ar fraction (Ar fraction 98%, HMDSO fraction 2%, respectively)
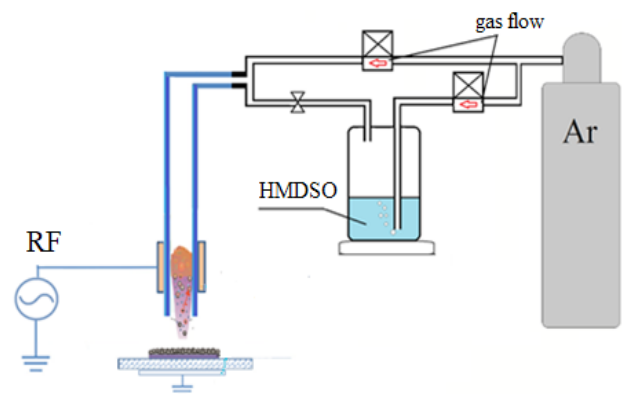
Figure 1 – Scheme of experimental setup

Main provision

In this study, a nanoscale coating was applied to the glass surface using RF discharge at atmospheric pressure. The coating exhibits hydrophobic properties. The hydrophobicity was tested under various experiment cycles while maintaining constant power, as well as assessing its durability over time.

Results and discussion

The following analyses were carried out to determine the properties of the coating formed as a result of the reaction of precursors with plasma flow on the surface of a glass sample.

- Morphological properties

The morphological properties of the synthesized samples were studied using a Quanta 3D 200i scanning electron microscope (SEM). The results of the analysis showed that the obtained particles have a variety of shapes, including spherical. The surface of the particles is heterogeneous and their sizes vary from 20 nm to 0.1 μm (Fig. 2).

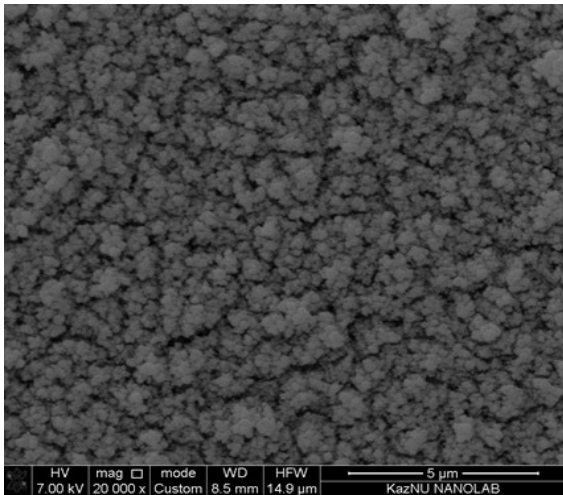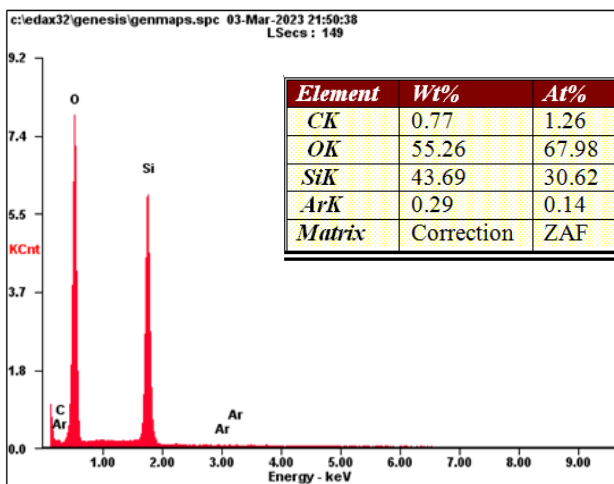**Figure 2** – SEM-micrographs of synthesized superhydrophobic particles formed on the glass surface

- Chemical composition

EDS spectroscopy (Electron Dispersive Spectroscopy) was used to determine the chemical composition of the synthesized coatings. The results of the analysis showed that the obtained coatings consist of the precursors component elements (Fig. 3)

- Hydrophobic properties

The morphological analysis of the obtained sample showed that the surface presents a water repellent property, i.e. hydrophobic character. To confirm this, the angle of contact with water was evaluated. Figure 4 shows a graph showing the relationship between the contact angle and the number of cycles of the experiment.

When analyzing the graph, it becomes evident that the contact angle undergoes minimal changes when the number of cycles is changed (Fig. 5).

Figure 3 – Chemical composition of obtained coatings
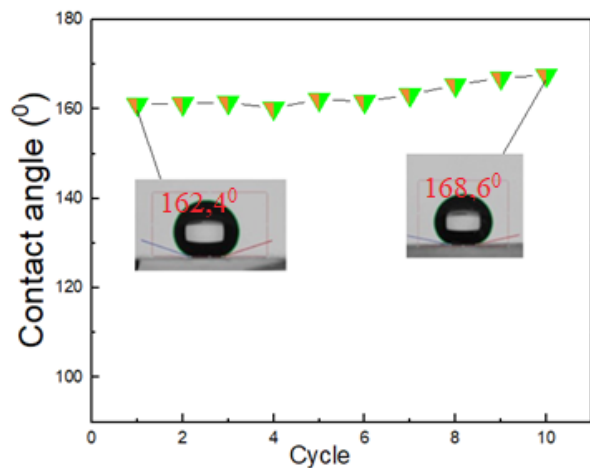
Figure 4 – Hydrophobic properties of the obtained samples proving through contact angle from the cycle of experiment
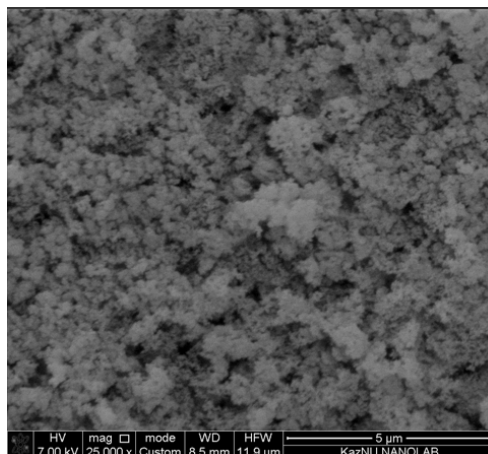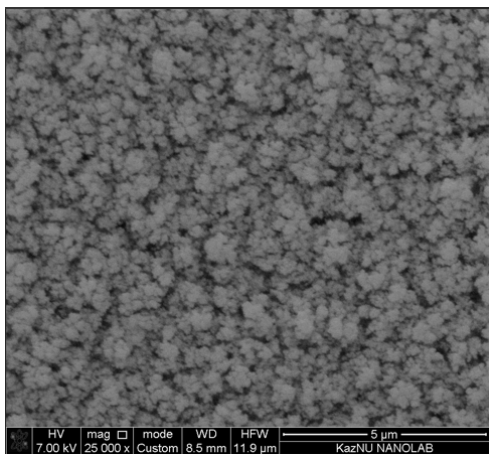
Figure 5 – Change of coating surface with increasing cycle of the experiment

This indicates that the experimental cycles have a negligible effect on the contact angle of the film because the process reached an equilibrium state relatively quickly, where further cycles have less and less effect on the surface properties. Also for further characterization, the contact angle with a long time course was measured (Figure 6). A trend is shown that the contact angle decreases over time which indicates a loss of superhydrophobicity i.e. the surface becomes less water repellent. The samples were stored under room conditions. However, when exposed to environmental factors such as UV radiation, humidity or chemical contaminants, the surface may undergo degradation. As a result of degradation, the surface structure may change, i.e., the chemical composition of the surface changes resulting in an uneven surface that will reduce its ability to effectively repel water.
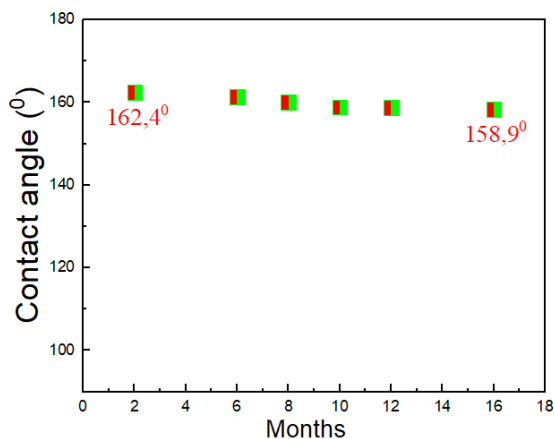
Figure 6 – Hydrophobic properties of the obtained samples proving through contact angle from the over time (0-18 months)

Conclusion

In conclusion, this study successfully demonstrated the formation and characterization of nanoscale coatings on a substrate through plasma polymerization, utilizing the precursor C6H18OSi2 and Ar carrier gas under radiofrequency discharge. The investigation focused on optimizing plasma parameters and assessing the coatings' properties under atmospheric pressure conditions, with particular attention to the number of experiment cycles. Through thorough analysis using scanning electron microscopy (SEM) and energy dispersive spectroscopy (EDS), we gained insights into the structural morphology and elemental composition of the coatings. Furthermore, the observed hydrophobicity of the coatings suggests their potential utility in applications requiring water repellency.

The results presented herein contribute to advancing our understanding of nanoscale coating synthesis and performance, with implications for various fields such as surface engineering, materials science, and functional coatings. Future research may delve deeper into optimizing coating parameters and exploring additional characterization techniques to further enhance our understanding and potential applications of these coatings.

Acknowledgements

References

1.   Wensheng Li, Zhenting Yin, Liangyuan Qi, Bin Yu, Weiyi Xing. "Scalable production of bioinspired MXene/black phosphorene nanocoatings for hydrophobic and fire-safe textiles with tunable electromagnetic interference and exceeding thermal management. ". *Chemical Engineering Journal* 460 no 15 (2023):141870– (In China). https://doi.org/10.1016/j.cej.2023.141870

2.   Xiaodi Dong, Baoquan Wan, Yang Feng, Daomin Min, Ming-Sheng Zheng, Haiping Xu, Zhi-Min Dang, George Chen, Jun-Wei Zha. "Ultra-low-permittivity, high hydrophobic, and excellent thermally stable fluoroelastomer/polyimide composite films employing dielectric reduction ". *European Polymer Journal* 181 no 5 (2022): 111667– (In China), https://doi.org/10.1016/j.eurpolymj.2022.111667

3.   Jiaojiao Du, Pengfei Wu, Haijiang Kou, Pengfei Gao, Yang Cao, Lingling Jing, Shengyu Wang, Peter Rusinov, Chao Zhang. "Self-healing superhydrophobic coating with durability based on EP + PDMS/SiO2 double-layer structure design". *Progress in Organic Coatings* 190 (2024): 108359–(In China) https://doi.org/10.1016/j.porgcoat.2024.108359

4.   Chuanlong Ma, Lei Wang, Anton Nikiforov, Yuliia Onyshchenko, Pieter Cools, Kostya (Ken) Ostrikov, Nathalie De Geyter, Rino Morent. "Atmospheric-pressure plasma assisted engineering of polymer surfaces: From high hydrophobicity to superhydrophilicity". *Applied Surface Science* 535 (2021):147032–(In Ghent, Belgium) https://doi.org/10.1016/j.apsusc.2020.147032

5.   Yawen Yuan, Yishi Wang, Shasha Liu, Xuxue Zhang, Xinzheng Liu, Changhui Sun, Dong Yuan, Yan Zhang, Xiaorong Cao. "Direct chemical vapor deposition synthesis of graphene super-hydrophobic transparent glass" *Vacuum* 202 ., (2022): 111136–(In China) https://doi.org/10.1016/j.vacuum.2022.111136

6. A. Orazbayev, M. N. Jumagulov, M. K. Dosbolayev, M. Silamiya, T. S. Ramazanov, L. Boufendi,. "Optical spectroscopic diagnostics of dusty plasma in rf discharge". *In Dusty/Complex Plasmas: Basic and Interdisciplinary Research*, Vol. 1397 (2020): pp. 379-380–(In Kazakhstan) https://doi.org/10.1063/1.3659852

7. Sagi Orazbayev, Rakhymzhan Zhumadilov, Askar Zhunisbekov, Maratbek Gabdullin, Yerassyl Yerlanuly, Almasbek Utegenov, Tlekkabul Ramazanov. "Superhydrophobic carbonous surfaces production by PECVD methods". *Applied Surface Science* 515 (2020): 146050–(In Kazakhstan). https://doi.org/10.1016/j.apsusc.2020.146050

8. S.A. Orazbayev, A.U. Utegenov, A.T. Zhunisbekov, M. Slamyiya, M.K. Dosbolayev, T.S. Ramazanov, "Synthesis of carbon and copper nanoparticles in radio frequency plasma with additional electrostatic field " *Contrib. Plasma Phys.* 58 (10) (2018): 961–966–(In Kazakhstan). https://doi.org/10.1002/ctpp.201700146

9. S.A. Orazbayev, M.M. Muratov, T.S. Ramazanov, M.K. Dosbolayev, M. Silamiya, M.N. Jumagulov, and L. Boufendi. "The Diagnostics of Dusty Plasma in RF Discharge by Two Different Methods" *Contrib. Plasma Phys.* 53 (2013): 436–(In Kazakhstan). https://doi.org/10.1002/ctpp.201200123

10. Zheng, S., Li, C., Fu, Q., Li, M., Hu, W., Wang, Q., Chen, Z. "Fabrication of self-cleaning superhydrophobic surface on aluminum alloys with excellent corrosion resistance". *Surf. Coat. Technol.* 276 (2015): 341–348–(In China) . https://doi.org/10.1016/j.surfcoat.2015.07.002

11. Genzer, J., and Efimenko, K. "Recent developments in superhydrophobic surfaces and their relevance to marine fouling: a review". *Biofouling* 22 (5-6) (2006): 339-360–(In China). https://doi.org/10.1080/08927010600980223

12. Zixiao Hong, Yuxin Xu, Daiqi Ye, Yun Hu. "One-step fabrication of a robust and transparent superhydrophobic self-cleaning coating using a hydrophobic binder at room temperature: A combined experimental and molecular dynamics simulation study". *Surface and Coatings Technology* 472 (2023): 129943–(In China) https://doi.org/10.1016/j.surfcoat.2023.129943

13. Jiaojiao Du, Pengfei Wu, Haijiang Kou, Pengfei Gao, Yang Cao, Lingling Jing, Shengyu Wang, Peter Rusinov, Chao Zhang. "Self-healing superhydrophobic coating with durability based on EP + PDMS/SiO2 double-layer structure design". *Progress in Organic Coatings* 190 (2024): 108359–(In China) https://doi.org/10.1016/j.porgcoat.2024.108359

14. Shih-Hsien Yang, Chi-Hung Liu, Chun-Hsien Su, Hui Chen. "Atmospheric-pressure plasma deposition of SiOx films for super-hydrophobic application". *Thin Solid Films*, Pages 517 no (17) (2009): 5284-5287–(In Taiwan ROC) https://doi.org/10.1016/j.tsf.2009.03.083

15. Jizhou Sun , Jian Wang, Weichen Xu, Binbin Zhang. "A mechanically robust superhydrophobic corrosion resistant coating with self-healing capability". *Materials & Design* 240 (2024): 112881–(In China) https://doi.org/10.1016/j.matdes.2024.112881

16. K.B. Golovin, J.W. Gose, M. Perlin, S.L. Ceccio, A. Tuteja. "Bioinspired surfaces for turbulent drag reduction". *Phil. Trans. Math. Phys. Eng. Sci.* 374 (2016): 20160189–(In China) https://doi.org/10.1098/rsta.2016.0189.

17. S. Brown, J. Lengaigne, N. Sharifi, M. Pugh, C. Moreau, A. Dolatabadi, L. Martinu, J.E. "Klemberg-Sapieha, Durability of superhydrophobic duplex coating systems for aerospace applications*". Surface and Coatings Technology* 401 (2020): 126249–(In Canada) https://doi.org/10.1016/j.surfcoat.2020.126249.

18. K. Gotoh, E. Shohbuke, G. Ryu. "Application of atmospheric pressure plasma polymerization for soil guard finishing of textiles" *Textil. Res. J.* 88 (2018): 1278–1289, https://doi.org/10.1177/0040517517698988.

19. Asadollahi, S., Profili, J., Farzaneh, M., & Stafford, L. "Multi-pass deposition of organosilicon-based superhydrophobic coatings in atmospheric pressure plasma jets". *Thin Solid Films* 714 (2020): 138369–(In Canada) https://doi:10.1016/j.tsf.2020.138369

20. L. Wang, S. Guo and S. Dong. "Facile Electrochemical Route to Directly Fabricate Hierarchical Spherical Cupreous Microstructures: Toward Superhydrophobic Surface". *Electrochemistry Communications*, Vol. 10 no 4 (2008), , pp. 655-658–(In China) . https://doi.org/10.1016/j.elecom.2008.01.034

21. Sultan S. Ussenkhan, Baglan A. Kyrykbay, Yerassyl Yerlanuly, Askar T. Zhunisbekov, Maratbek T. Gabdullin, Tlekkabul S. Ramazanov, Sagi A. Orazbayev, Almasbek U. Utegenov, "Fabricating durable and stable superhydrophobic coatings by the atmospheric pressure plasma polymerisation of hexamethyldisiloxane". *Heliyon*,Volume 10, Issue 1, (2024): e23844–(In Kazakhstan) . https://doi.org/10.1016/j.heliyon.2023.e23844

22. Orazbayev S., Gabdullin M., Ramazanov T., Askar, Z., Rakhymzhan Z. "Obtaining hydrophobic surfaces in atmospheric pressure plasma". *Mater. Today Proc.* 20 (2020):335–341–(In Kazakhstan).. https://doi.org/10.1016/j.matpr.2019.10.071

Information about authors:

Baglan A. Kyrykbay (corresponding author) – Institute of Applied Sciences and Information Technologies of the Republic of Kazakhstan (Almaty, Republic of Kazakstan) e-mail: baglankyrykbaj44@gmail.com

Assan R. Abdirakhmanov – PhD at the Institute of Applied Sciences and Information Technologies of the Republic of Kazakhstan (Almaty, Republic of Kazakhstan) e-mail: abdirakhmanov@physics.kz

Sultan S. Ussenkhan – Institute of Applied Sciences and Information Technologies of the Republic of Kazakhstan (Almaty, Republic of Kazakstan) e-mail: sultan@physics.kz

Almasbek U. Utegenov – PhD at the Institute of Applied Sciences and Information Technologies of the Republic of Kazakhstan (Almaty, Republic of Kazakhstan) e-mail: almasbek@physics.kz

Yerlanuly Yerassyl – PhD at the Institute of Applied Sciences and Information Technologies of the Republic of Kazakhstan (Almaty, Republic of Kazakhstan) e-mail: yerlanuly@physics.kz

Tlekkabul S. Ramazanov – Doctor of Physical and Mathematical Sciences, Professor, Academician of the National Academy of Sciences of the Republic of Kazakhstan, Laureate of the State Prize of the Republic of Kazakhstan in the field of science and technology at the Institute of Applied Sciences and Information Technologies of the Republic of Kazakhstan (Almaty, Republic of Kazakhstan) e-mail: tlekkabul.ramazanov@kaznu.edu.kz

Talgat B. Koshtybayev – PhD at the Institute of Applied Sciences and Information Technologies of the Republic of Kazakhstan (Almaty, Republic of Kazakhstan) e-mail: koshtybayevt@gmail.com

Sagi A. Orazbayev – Associate Professor at the Institute of Applied Sciences and Information Technologies of the Republic of Kazakhstan (Almaty, Republic of Kazakhstan) e-mail: sagi.orazbayev@gmail.com

B Roopa Sri[1*] and Y Lakshmi Naidu[2]

[1]Department of Mathematics and Computer Science, Sri Sathya Sai Institute of Higher Learning, Andhra Pradesh, India
[2]Centre for Excellence in Mathematical Biology, Sri Sathya Sai Institute of Higher Learning, Andhra Pradesh, India
*e-mail: behararoopasri@sssihl.edu.in

On Zagreb Connection Indices
of γ Graphyne and its Zigzag Nanoribbon

Abstract. Chemical graph theory is a branch of Mathematical Chemistry that deals with chemical/molecular graphs to predict molecules' reactivity, stability, and topology through topological indices. γ graphyne is a carbon allotrope, a crystal lattice composed of one acetylene bond connecting two aromatic rings. Since there is no evidence of any economical method for its synthesis to date to study the physicochemical properties, reactivity, and stability, the in-silico methods can be of great help. In this paper, we have considered Zagreb connection indices, which haven't been explored in a wide range despite their correlation with the physicochemical properties being better than classical Zagreb Indices. Here, Zagreb connection indices of γ graphyne have been calculated using the edge partition technique and their trend in characteristics has been plotted. This might be beneficial to the fields of medicine, pharmacology, and nanotechnology in studying the reactivity and stability of this nanostructure without performing expensive experiments.

Key words: Chemical graph theory, γ graphyne, Zagreb connection indices.

Introduction

Carbon nanomaterials are nanomaterials that are built on carbon atoms. Based on their geometrical structure, they are classified as carbon allotropes (graphite and diamond) and nanostructures namely graphene single sheets, single and multiwalled nanotubes, carbon fibers, fullerenes, onions, and nanodiamonds are generated by carbon. Fullerenes are mostly produced through the vaporization of graphite electrodes using arc or plasma discharges or using laser ablation, pyrolysis of hydrocarbons and optimization of this process led to the mass production of the most widely studied fullerene C_{60} and other bigger fullerenes from C_{70} to C_{96} [1]. The arc discharge method is a well-established and broadly utilized technique for carbon nanotube synthesis. The resultant of the nanotube being single-walled or multi-walled depends on the selection of metal catalyst in the process. However, the laser ablation method gave a high yield of carbon nanotubes compared to other techniques but it is cost-consumable as it requires high energy power for vaporization of the target[2]. Various methods for Graphene synthesis are classified into top-down and bottom-up methods. For more information regarding the synthesis of carbon allotropes and nanomaterials, refer to [3] [4].

Most of these structural framework consists of either sp^2 or sp^3 hybridized carbon atoms. However, the presence of sp-hybridized carbons could affect the properties of the structures. Therefore, the great challenge for the researchers is to synthesize novel carbon isomers. One such challenge is synthesizing one of the carbon allotropes, graphyne, which consists of highly sp-hybridized carbon atoms. Mechanochemical synthesis, Sonogashira coupling, Castro–Stephens coupling, and alkyne metathesis are some of the developed methods for its synthesis but they have their advantages and limitations. This graphyne family has been proving its promising usage in the fields of medicine, photovoltaics, and the development of nanoscale devices.

Graphyne is a crystal lattice composed of acetylene bonds connecting the benzene rings. This can also be named graphyne-n depending on the number of acetylene molecules used for connecting the benzene rings. The most structurally stable families of graphyne are γ graphyne and γ graphdiyne as they contain benzene rings in their structure. In 1987, Baughman et al. [5] proposed this allotrope of carbon for the first time theoretically, and later in 2010, Li et al. [6] developed a successful methodology for graphdiyne films (benzene rings connected by diacetylene molecules) synthesis. Alkyne coupling reaction of hexaethynylbenzene (HEB) is the most

efficient method used to synthesize γ graphdiyne [7]. In 2019, Cui and co-workers proposed a technique for obtaining γ graphyne from benzene [8]. γ Graphyne is a graphyne family lattice comprising two aromatics rings connected by one acetylene molecule. But to date, there is no evidence of any economical method for the synthesis of this structure to study its molecular and topological properties. Hence, there is a need for in-silico methods. One such method is to calculate molecular descriptors for their quantitative structure-property and structure-activity relationship analysis.

A graph G is an ordered triple consisting of a set of vertices V(G) and a set of edges E(G), wherein each edge in E(G) is incident on a pair of vertices from V(G). A chemical graph or molecular graph is a simple connected graph of the chemical molecules in which atoms are taken as atoms and bonds between them as edges. The degree of the vertex, 'd(u)' is the number of edges incident on the vertex 'u'. The distance d(u,v) between two vertices 'u' and 'v' is the number of edges involved in the shortest path between 'u' and 'v'. Molecular descriptors are the quantitative representatives of molecular graphs that are used in physicochemical characteristics prediction and topological studies. These are categorized based on the dimensions of the molecular graphs. To study the properties and topology of 2-D graphs, the molecular descriptor considered is called the topological index. A topological index is a graph-invariant number obtained from a chemical graph and is formulated based on either the degree of the vertex or the distance between the vertices..

Materials and Methods

There is a branch of mathematics, known as chemical graph theory, in which the topological study of molecules takes place by considering their chemical graphs and calculating topological indices. Using these topological indices, structure-property and structure-activity analysis can be performed theoretically.

Literature Review

The first topological index, the Wiener index, is distance-based and was formulated by a Mathematician, named Wiener in the year 1947, and found that this index has a good correlation with the boiling points of paraffin [9]. To date, there are more than 3000 topological indices that are being under study by many researchers. These are being

modified and reformulated to improve their accuracy in predicting the properties of chemical compounds. One such reformulation of degree-based topological indices, Zagreb Indices, using connection number instead of degree of the vertex, led to many open problems to be solved [10]. To study more on these, one can refer to [11, 12, 13].

A. Hakeem et al. have derived the mathematical closed-form expressions of different degree-based topological indices for γ graphyne and zig-zag graphyne nanoribbon through a graph-based edge partition technique [14]. They have explored the molecular descriptors of these structures for the first time. Motivated by this, we have extended their work by choosing Zagreb connection indices as a base and formulated the closed-form expressions with the help of these connection indices. One can refer to the above paper for the chemical structure of γ Graphyne.

Zagreb connection indices or leap Zagreb indices are formulated based on the connection number of the vertices. Connection number $\tau_G(u)$ of a vertex 'u' in graph G is the total number of vertices at a distance 2 from 'u'. These leap Zagreb indices were formulated in 1972 and were restudied by Akbar Ali and Nenad Trinajstic in 2018 [15] and they have shown that these indices can be generalized as Bond incident connection-number (BIC (G)) index:

$$BIC(G) = \sum_{0 \leq a \leq b \leq n-2} y_{a,b}(G) * \phi_{a,b} \tag{1}$$

where $y_{a,b}(G)$ represents the number of edges in G incident on the vertices with connection numbers a and b and $\phi_{a,b}$ represents a non-negative real-valued function that depends on a and b.

Definition 1. For graph G, the first and the second Zagreb connection indices are defined as:

$$ZC_1(G) = \sum_{u \in V(G)} \tau_G^2(u) \tag{2}$$

$$ZC_2(G) = \sum_{uv \in E(G)} \tau_G(u) * \tau_G(v) \tag{3}$$

Definition 2. The modified first and second leap indices are given by Ali et al. [15]

$$ZC_1^*(G) = \sum_{uv \in E(G)} \tau_G(u) + \tau_G(v) \tag{4}$$

$$ZC_2^*(G) = \sum_{uv \in E(G)} d_u \tau_G(u) + d_v \tau_G(v) \tag{5}$$

Few works on these indices proved that there exists a strong correlation between the physical properties like entropy, standard enthalpy of vaporization, boiling point, and vapor infiltration of biochemical compounds and these indices compared to other indices. It has been proved that ZC_1 corresponds well with the entropy and acentric factors of octane isomers. These leap indices have also shown better results compared to the classical Zagreb indices [15]. References can be found in [15], [16], [17], and [18]. Despite their out-performance, these indices haven't been explored much in detail. Hence, in this paper, we have considered the least explored topological indices and chemical structure i.e., Zagreb connection indices of γ graphyne.

Results and Discussion

The chemical graphs of γ Graphyne, *G(m,n)* and its zig-zag nanoribbon, *G(n)* are depicted in Figures 1 and 2 by considering atoms of the structure as nodes and bonds between them as edges. Here $m \geq 1$ and $n \geq 1$ represent the number of rows and columns in the chemical graph. In this section, the mathematical closed-form expressions of above mentioned Zagreb connection indices are formulated for both structures. The trend in their characteristics can be inferred from the graphs plotted against each connection index.

γ Graphyne

In Figure 1, there are $36mn+12m+12n-6$ vertices and $24mn+12m+12n-6$ edges in each row. Using the edge partitioning method, we calculate the number of edges, |E|, incident on the vertices u and v with degrees d_u and d_v and connection numbers τ_u and τ_v respectively. From Figure 1, it is prominent that the vertices with degree 2 have the connection numbers 2, 3, or 5 and the vertices of degree 3 have 3, 5, or 6 as connection numbers.

Hence, in Table 1,

$$|E| = |\{uv \in E(G(m,n)): ((d_u, d_v), (\tau_u, \tau_v)) \}|,$$

where τ_u is the connection number of vertex 'u' with degree d_u.

Theorem 1. For the graph *G(m,n)*

$$ZC_1(G(m,n)) = 864mn$$

$$ZC_2(G(m,n)) = 1296mn - 70m - 70n + 38$$

Table 1 – Edge-partition of γ graphyne

(d_u, d_v)	(τ_u, τ_v)	|E|
(2,2)	(2,2)	3; n=1 2; n≥2
	(3,2)	6; n=1 n+6; n≥2
(2,3)	(3,5)	2n+4
(3,3)	(5,5)	5n+1

Table 2 – Edge-partition of zig-zag γ graphyne nanoribbon

(d_u, d_v)	(τ_u, τ_v)	|E|
(2,2)	(3,2)	8m+8n-4
(2,3)	(3,5)	8m+8n-4
(3,3)	(5,5)	2m+2n+2
	(5,6)	12m+12n-12
	(6,6)	36mn-18m-18n+12

Table 3 – Zagreb connection indices of γ graphyne

n	ZC_1 (G(m, n))	ZC_2 (G(m, n))	ZC_1^* (G(m, n))	ZC_2^* (G(m, n))
1	864	1194	492	1356
2	3456	4942	1868	5324
3	7776	11282	4108	11884
4	13824	20241	7212	21036
5	21600	31738	11180	32780
6	31104	45854	16012	47116
7	42336	62562	21708	64044
8	55296	81862	28268	83564
9	69984	103754	35692	105676
10	86400	128238	43980	130380

Table 4 – Zagreb connection indices of zig-zag γ graphyne nanoribbon

n	ZC_1 (G(n))	ZC_2 (G(n))	ZC_1^* (G(n))	ZC_2^* (G(n))
1	228	288	150	378
2	346	451	222	578
3	464	612	293	776
4	582	773	364	974
5	700	934	435	1175
6	818	1095	506	1370
7	936	1256	577	1568
8	1054	1417	648	1766
9	1172	1578	719	1964
10	1290	1739	790	2162

Proof. Let $G(m,n)$ be the graph of γ graphyne depicted in Figure 1. From eq.(2), we have

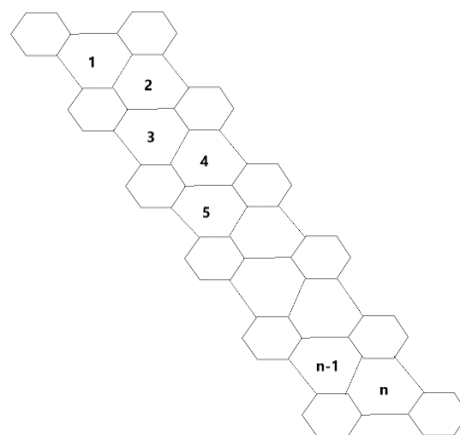$$ZC_1(G(m,n)) = \sum_{u \epsilon V(G(m,n))} \tau_G^2(u)$$

This can also be written as

$$ZC_1(G(m,n)) = \sum_{u \epsilon V(G(m,n))} c_k k^2 \quad (6)$$

where 'k' is the connection number τ_u and c_k is the number of vertices with connection number 'k' in $G(m,n)$.
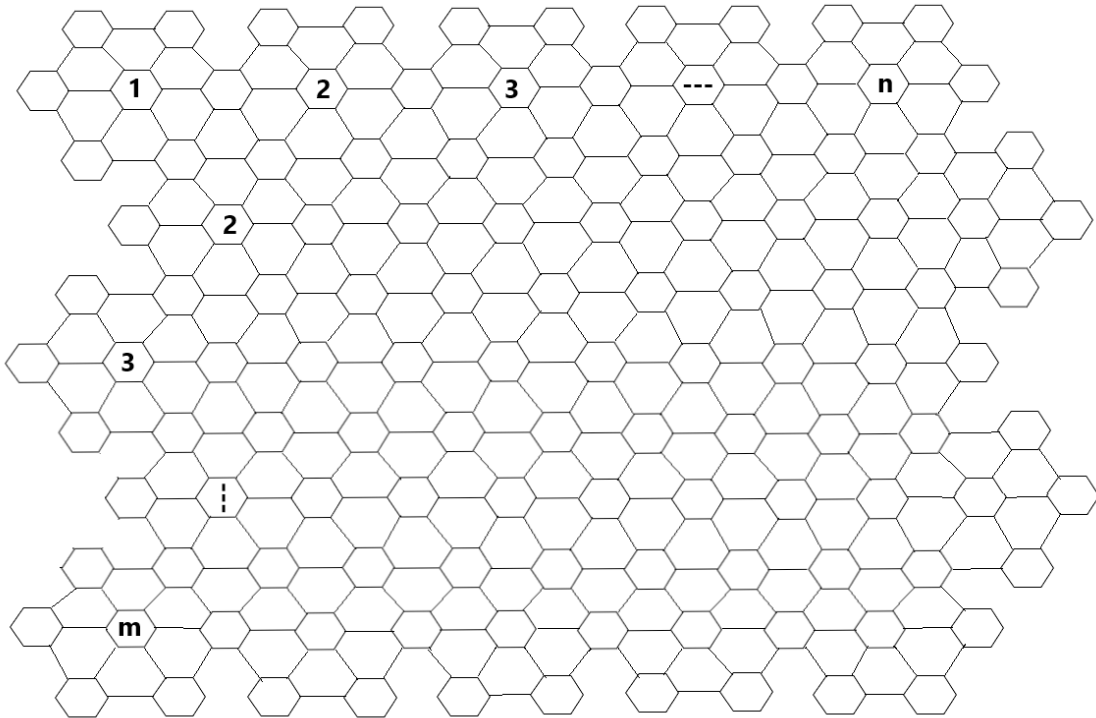
Figure 1 – Molecular graph of γ graphyne $G(m,n)$

Figure 2 – Molecular graph of Zig-zag γ graphyne nanoribbon $G(n)$
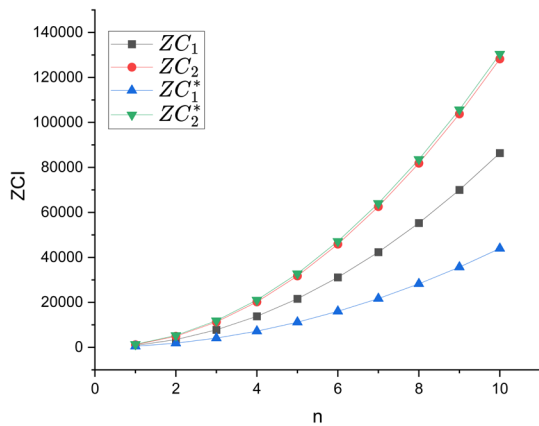
Figure 3 – Characteristics trend in
γ graphyne
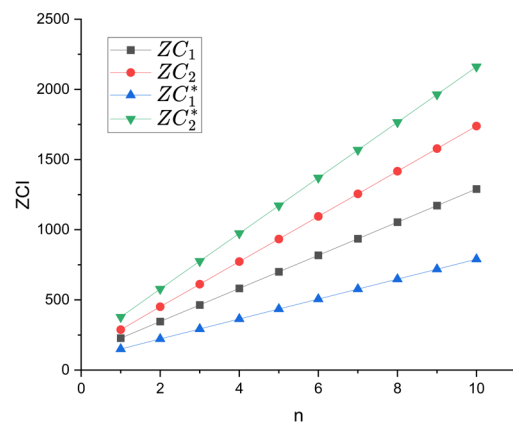
Figure 4 – Characteristics trend in zig-zag
γ graphyne nanoribbon

The connection number, τ_u, obtained for every vertex 'u' in $G(m, n)$ is either 2, 3, 5, or 6.

For k = 2, 3, 5, & 6; c_k is found to be $8n - 2, 16n - 4, 16n - 4$, and $24mn - 16n + 4$ respectively.

Hence, eq. (6) becomes

$ZC_1(G(m,n)) = (8n - 2)(4) + (16n - 4)(9) +$
$+ (16n - 4)(25) + (24mn - 16n + 4)(36) = 864mn$

Using Table 1, we have eq.(3)

$ZC_2(G(m,n)) = \displaystyle\sum_{uv \in E(G(m,n))} \tau_G(u) * \tau_G(v)$
$= (6)(8m + 8n - 4) + (15)(8m + 8n - 4) +$
$+ (25)(2m + 2n + 2) + (30)(12m + 12n - 12) +$
$+ (36)(36mn - 18m - 18n + 12)$
$= 1296mn - 70m - 70n + 38$

Theorem 2. For the graph $G(m,n)$,

$ZC_1^*(G(m,n)) = 432nm + 40m + 40n - 20$

$ZC_2^*(G(m,n)) = 1296mn + 40m + 40n - 20$

Proof. Let $G(m, n)$ be the graph of γ graphyne depicted in Figure 1. Now, eq.(4) can be written as

$ZC_1^*(G(m,n)) = \displaystyle\sum_{uv \in E(G(m,n))} \tau_G(u) + \tau_G(v)$
$= (5)(8m + 8n - 4) + (8)(8m + 8n - 4) +$
$+ (10)(2m + 2n + 2) + (11)(12m + 12n - 12) +$
$+ (12)(36mn - 18m - 18n + 12)$
$= 432mn + 40m + 40n - 20$

Similarly, eq.(5) is

$ZC_2^*(G(m,n)) = \displaystyle\sum_{uv \in E(G(m,n))} d_u\tau_G(u) + d_v\tau_G(v)$
$= (10)(8m + 8n - 4) + (19)(8m + 8n - 4) +$
$+ (30)(2m + 2n + 2) + (33)(12m + 12n - 12) +$
$+ (36)(36mn - 18m - 18n + 12)$
$= 1296mn + 40m + 40n - 20$

Zig-zag γ graphyne nanoribbon

In this graph, G(n), we shall consider a nanoribbon of zig-zag γ graphyne with n rows. Each row in Figure 2 consists of $5n + 1$ vertices and $6n$ edges. The connection number of vertices with degree 2 is 2 or 3 and those with degree 3 is 5 respectively. Different parameters in Table 2 can be inferred from Figure 2 as follows:

$|E| = |\{uv \in E(G(n)) : ((d_u, d_v),(\tau_u, \tau_v))\}|,$

where τ_u is the connection number of vertex 'u' with degree d_u.

This is done using the edge-partition technique. But, here, |E| varies for different n.

Theorem 3. For the graph

$ZC_1(G(m,n)) = 118n + 110$
$ZC_2(G(m,n)) = 288; \, n=1$
$\qquad\qquad = 161n + 129; \, n \geq 2$

Proof. Let G(n) be the graph of zig-zag γ graphyne nanoribbon depicted in Figure 2. From eq.(2), we have

$ZC_1(G(n)) = \displaystyle\sum_{u \in V(G(n))} \tau_G^2(u)$

This can also be written as

$$ZC_1(G(n)) = \sum_{u \in V(G(n))} c_k k^2 \qquad (7)$$

where 'k' is the connection number τ_u and c_k is the number of vertices with connection number 'k' in G(n)

In G(n), τ_u for every vertex 'u', is found to be either 2 or 3, or 5. For k = 2,3, & 5; c_k is found to be 6,2n + 4, & 4n + 2 respectively. Hence, eq. (7) becomes

$$ZC_1(G(n)) = (6)4 + (2n + 4)9 + (4n + 2)25$$
$$= 118n + 110$$

Using Table 2 and eq.(3), we obtain two cases as follows.

$$ZC_2(G(n)) = \sum_{uv \in E(G(n))} \tau_G(u) * \tau_G(v)$$

Case 1: For n = 1

$$ZC_2(G(n)) = 3(4) + 6(6) + 6(15) + 6(25) = 288$$

Case 2: For n ≥ 2

$$ZC_2(G(n)) = (2)4 + (n + 6)6 + (2n + 4)15 +$$
$$+ (5n + 1)25 = 161n + 129$$

Theorem 4. For the graph *G(n),*

$$ZC_1^*(G(n)) = 150 \qquad ; n = 1$$
$$= 71n + 80; n \geq 2$$
$$ZC_2^*(G(n)) = 378; n = 1$$
$$= 198n + 182; n \geq 2$$

Proof. Let G(n) be the graph of zig-zag γ graphyne nanoribbon depicted in Figure 2.
From eq.(4), we have

$$ZC_1^*(G(n)) = \sum_{uv \in E(G(n))} \tau_G(u) + \tau_G(v)$$

Case 1: For n = 1

$$ZC_1^*(G(n)) = (2)4 + (n + 6)6 + (2n + 4)15 +$$
$$+ (5n + 1)10 = (3)4 + (6)5 + (6)8 + (6)10 = 150$$

Case 2: For n ≥ 2

$$ZC_1^*(G(n)) = (2)4 + (n + 6)5 + (2n + 4)8 +$$
$$+ (5n + 1)10 = 71n + 80$$

Using Table 2 and eq.(5), the following two cases are obtained.

$$ZC_2^*(G(n)) = \sum_{uv \in E(G(n))} d^u \tau_G(u) + dv \tau_G(v)$$

Case 1: For n=1

$$ZC_2^*(G(n)) = 3(8) + 6(10) + 6(19) + 6(30) = 378$$

Case 2: For n≥2

$$ZC_2^*(G(n)) = (2)8 + (n + 6)10 + (2n + 4)19 +$$
$$+ (5n + 1)30 = 198n + 182$$

Using the closed-form mathematical expressions from the above Theorems 1, 2, 3, and 4, we calculated the four leap Zagreb indices such as the first Zagreb connection index, second Zagreb connection index, modified first Zagreb connection index, and modified second Zagreb connection index for different values of *m* and *n*. The leap Zagreb indices of γ graphyne and zig-zag γ graphyne nanoribbon were given in Tables 3 and 4 respectively. The graphical interpretation of the trend in these indices of G(m,n) and G(n) are depicted well in Figures 3 and 4.

Conclusion

We can observe from Figures 3 and 4 that the modified second Zagreb index, ZC_2^*, gave the highest values for both structures compared to other Zagreb connection indices.

According to the correlation between the Zagreb connection indices and various physicochemical properties, it can be concluded that this index can outperform other indices in predicting the physicochemical properties of these structures. The trend in the characteristics of these structures depends on the values *m* and *n*. It can also be observed that the trend in characteristics of these structures has a linear correlation with the connection indices. We could also observe that these connection indices have given better results when compared to the degree-based indices namely the Harmonic index, Randic index, sum connectivity index, Atom bond connectivity index, Geometric arithmetic index, and symmetric division degree index considered by A. Hakeem et al. in [14]. This once again proves that connection-based indices can be used in predicting various properties of molecules and molecular structures in place of other indices due to their better performance.

In the future, we will work on Zagreb connection indices of some other novel chemical structures. This might help the departments of medicine, bio-medicine, nanotechnology, and pharmaceutical sciences study the reactivity and stability of those structures without synthesizing and performing the required experiments.

Declarations

Conflict of interest: The authors have no competing interests to declare relevant to this article's content.

References

1. Murayama, Hideki., Tomonoh, Shigeki., Alford, J. Michael., & Karpuk, Michael E. "Fullerene Production in Tons and More: From Science to Industry." *Fullerenes, Nanotubes, and Carbon Nanostructures* 12, (2005): 1-9p, doi:10.1081/FST-120027125.

2. Das, Rasel., Shahnavaz, Zoreh., Ali, Md. Eaqub., Islam, Mohammed. Moinul., & Abd Hamid, Sharifah Bee. "Can We Optimize Arc Discharge and Laser Ablation for Well-Controlled Carbon Nanotube Synthesis?" *Nanoscale Res Lett.* 11, no.1 (2016): 510p, https://doi.org/10.1186/s11671-016-1730-0.

3. Speranza, G. "Carbon Nanomaterials: Synthesis, Functionalization, and Sensing Applications." *Nanomaterials (Basel)* 11, (2021): 967p, doi:10.3390/nano11040967.

4. Chen, Xiangnan., Wang, Xiaohui., & Fang, De. "A review on C1s XPS-spectra for some kinds of carbon materials." *Fullerenes, Nanotubes, and Carbon Nanostructures* 28, no.12 (2020): 1048-1058p, doi:10.1080/1536383X.2020.1794851.

5. Baughman, R. H., Eckhardt, H., & Kertesz, M. "Structure□property predictions for new planar forms of carbon: Layered phases containing sp2 and sp atoms." *The Journal of Chemical Physics* 87, no.11 (1987): 6687-6699p, doi:10.1063/1.453405.

6. Li, Guoxing., Li, Yuliang., Liu, Huibiao., Guo, Yanbing., Li, Yongjun., & Zhu, Daoben. "Architecture of graphdiyne nanoscale films." *Chem. Commun. (The Royal Society of Chemistry)* 46, no.19 (2010): 3256-3258p, doi:10.1039/B922733D.

7. Jiaqiang, Li., & Han, Yu. "Artificial Carbon Allotrope γ-Graphyne: Synthesis, Properties, and Application." *Giant.* 13, (2023): 100-140p, doi:10.1016/j.giant.2023.100140.

8. Li, Qiaodan., Yang, Chaofan., Wu, Lulu., Wang, Hui., & Xiaoli, Cui. "Converting benzene into γ-graphyne and its enhanced electrochemical oxygen evolution performance." *J. Mater. Chem. A. (The Royal Society of Chemistry)* 7, no.11 (2019): 5981-5990p, doi:10.1039/C8TA10317H.

9. Trinajstic, Nenad. *Chemical Graph Theory.* 2. CRC Press, 1992.

10. Gutman, Ivan., Naji, Ahmed M., & Soner, Nandappa D.. "On leap Zagreb indices of graphs." *Communications in Combinatorics and Optimization* (Azarbaijan Shahid Madani University) 2, no.2 (2017): 99–117p.

11. Du, Zhibin., Ali, Akbar., & Trinajstic, Nenad. "Alkanes with the first three maximal/minimal modified first Zagreb connection indices." *Molecular informatics* (Wiley Online Library) 38, no.4 (2019): 180-116p.

12. Mohammadzadeh, Ardashir., Farid, Faiz., Javaid, Muhammad., & Bonyah, Ebenezer. "Computing Connection Distance Index of Derived Graphs." *Mathematical Problems in Engineering* (Hindawi) (2022): 143-177p.

13. Ye, Ansheng., Qureshi, Muhammad Imran., Fahad, Asfand., Aslam, Adnan., Jamil, Muhammad Kamran., Zafar, Asim., & Irfan, Rida. "Zagreb Connection Number Index of Nanotubes and Regular Hexagonal Lattice." *Open Chemistry* 17, no.1 (2019): 75–80p, doi:10.1515/chem-2019-0007.

14. Hakeem, Abdul., Ullah, Asad., & Zaman, Shahid. "Computation of some important degree-based topological indices for γ- graphyne and Zigzag graphyne nanoribbon." *Molecular Physics* (Taylor & Francis) (2023), doi:10.1080/00268976.2023.2211403.

15. Ali, Akbar., & Trinajstic, Nenad. «A novel/old modification of the first Zagreb index.» *Molecular informatics* (Wiley Online Library) 37, (2018): 6-7p.

16. Fahad, Asfand., Aslam, Adnan., Qureshi, Muhammad., Jamil, Muhammad Kamran., & Jalil, Abdul. «Zagreb Connection Indices of Some Classes of Network.» *Biointerface Research in Applied Chemistry* 11, (2020), doi:10.33263/BRIAC113.1007410081.

17. Hosamani, Sunilkumar., Basavanagoud, B., & Barangi, Anand. "First neighbourhood Zagreb index of some nanostructure." *PROCEEDINGS OF IAM* 7, (2019).

18. Khalid, Sohaib., Kok, Johan., Ali, Akbar., & Bashir, Mohsin. «Zagreb connection indices of TiO2 nanotubes." *Chemistry* 27, (2018).

Information about authors:

B Roopa Sri (corresponding author) – Department of Mathematics and Computer Science, Sri Sathya Sai Institute of Higher Learning (Andhra Pradesh, India) email: behararoopasri@sssihl.edu.in

Y Lakshmi Naidu ((corresponding author) – Centre for Excellence in Mathematical Biology, Associate Professor, Department of Mathematics and Computer Science, Sri Sathya Sai Institute of Higher Learning (Andhra Pradesh, India) email: ylakshminaidu@sssihl.edu.in

N. Narasimha Rao[1,*] , P. Naresh[2] P. Raghava Rao[1] ,
B.J.R.S.N. Swamy[1] , A. Chitti Babu[3] , P.Sobhanachalam[4]

[1]Department of Physics, Krishna University Dr.MRAR College of PG Studies, AP, India
[2]Department of Physics, Velagapudi Rama Krishna Siddharth Engineering College, AP, India
[3]Department of Physics, First year Engineering department Sir C.R.Reddy College of Engineering, AP, India
[4]Department of Physics, Krishna University, AP, India
*e-mail: nnrphy@gmail.com

Vanadium oxides impact on the ZNO-SB$_2$O$_3$-B$_2$O$_3$ glasses dielectric and ac conduction mechanisms

Abstract. In the current study, we have looked into the glasses dielectric characteristics as a follow-up to our prior work on the influence of vanadium ions in spectral properties of ZnO-Sb$_2$O$_3$-B$_2$O$_3$ glasses. B$_2$O$_3$ glasses have garnered interest as dielectric materials in addition to their uses as optical functional materials. Glasses of ZnO-Sb$_2$O$_3$-B$_2$O$_3$ that ranged in V$_2$O$_5$ concentration (from 0 to 1.0 mol %) were prepared using the standard melt and quench procedure. The densities were determined based on Archimedes' principle. Using these densities, physical parameters such as molar volume (Vm), mean vanadium ion separation distance (r$_i$) and vanadium ion concentration (N$_i$), polaron radius (r$_p$), were determined and presented. It has been investigated how the samples dielectric constant (ε), dielectric loss (tan δ), and ac conductivity (σ_{ac}) change with temperature at various frequencies between 10^2 Hz and 10^6 Hz. The results were examined in relation to the number of oxidation states of the vanadium ions.
Key words: Borate glasses, Dielectric constant, ac conductivity, vanadium ions.

Introduction

In recent years, there has increased interest in the review of disordered materials hopping conductivity. The actual portion of the ac conductivity has a power law [1] frequency dependency, which is the main characteristic of hopping conduction. To explain the mechanism of conduction in those materials, they must look at the frequency-structured electric conductivity of amorphous compounds [2].This leads to flexible and complex fashions that make it possible to characterize the digital homes of various materials [3]. Knowing glasses electric conductivity is essential because it is required to act as an electrical insulator or conductor in many applications [4].The dielectric properties, which include the dielectric constant (ε), loss (tan δ) and ac conductivity (σ_{ac}) spanning a broad spectrum of frequencies and temperature, make it easier to determine how well they act as insulators.The magnificent ionic achieving glasses are extensively researched because of their use in powerful excessive power density

batteries [5, 6] and in a few electrochemical devices [7, 8].

B$_2$O$_3$ glass structural model is coupled by BO$_3$ building blocks have been suggested [9-11]. The boroxol rings split off as the transitional glass temperature approaches, resulting in a more open structure. Glasses behavior as a host material is significantly influenced by its open structure, allowing sites to accommodate host ions over a much greater range of size and coordination number. Because they can be employed in a variety of solid state devices, borate glasses have drawn a lot of attention. These glasses all share the occurrence of localized states in the mobility gap, which results from the lack of long-range order and other fundamental flaws.

Most of the literature studies [12-16] reveals that, the heavy metal oxide glasses like Sb$_2$O$_3$-B$_2$O$_3$ glasses are very important optical materials with potential applications in non-linear optics, fast reacting optical switches, optical amplifiers and strong radioactive shielding materials due to their

high transparency, high polarizability and high refractive index.

We looked into the impact of vanadium ions on the spectral characteristics of ZnO-Sb$_2$O$_3$-B$_2$O$_3$ glasses in our earlier research [17]. The findings were examined in relation to the number of oxidation states of vanadium ions in the glass materials. As a follow-up to our prior research, we have looked at how the substitution of V$_2$O$_5$ affects the dielectric and ac conduction pathways in bulk amorphous ZnO-Sb$_2$O$_3$-B$_2$O$_3$ glasses spanning the temperature range of 303-523 K and frequency range of 10^2 to 10^6 Hz.

Materials and Methods

The present glass samples were synthesized by using the particular Analytic Reagent (AR) grade chemicals of ZnO (Merck, ≥99%), Sb$_2$O$_3$ (Merck, ≥99%), H$_2$BO$_3$ (TM Media, 99.5%) and V$_2$O$_5$ (SRL, 99.5%) in melt quenching process. The detailed composition was presented in the Table.1. The adapted procedure of glass synthesis was presented as a flow chart in Figure 1[17].
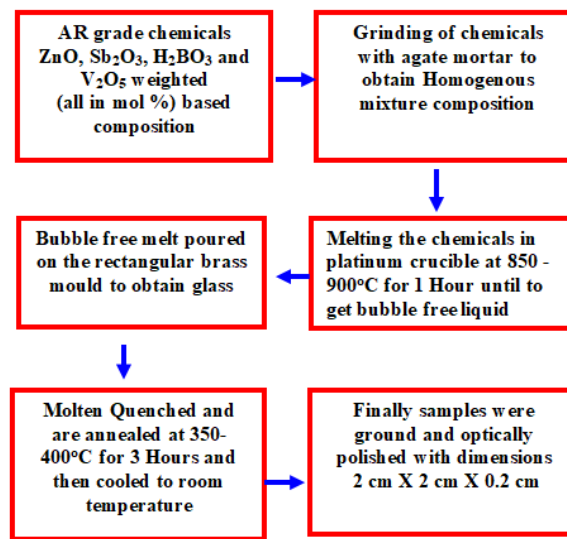
Figure 1 – Flow chart of various step involved in preparation of glass samples

Table1 – Composition of glass samples (all in mol%)

Sample Code	ZnO	Sb$_2$O$_3$	B$_2$O$_3$	V$_2$O$_5$
V$_0$	10.0	20.0	70.0	…..
V$_2$	10.0	19.8	70.0	0.2
V$_4$	10.0	19.6	70.0	0.4
V$_6$	10.0	19.4	70.0	0.6
V$_8$	10.0	19.2	70.0	0.8
V$_{10}$	10.0	19.0	70.0	1.0

The densities were determined based on Archimedes' principle, by measuring the weights of the sample in air as well as in O-xylene as a buoyant liquid [18]. Using these densities, the physical parameters viz., molar volume (V$_m$), mean vanadium ion separation distance (r$_i$) and vanadium ion concentration (N$_i$) etc., was determined using the standard relation [18].

XRD patterns were recorded with help of a SEIFERT X-pert PRO panalytical X-ray diffracto metre with CuK$_\alpha$-radiation. The dielectric parameters capacitance (c) and dissipation factor (D) were measured in between silver electrodes by using LCR Meter (model HP 4263B) by varying temperature systematically between 30-250°C and a frequency range of 10^2 to 10^5 Hz.

Results

From the measured weights of glass samples in air and buoyant liquid, densities were calculated, using these densities, the other physical parameters viz., dopant ion concentration, interionic distance, polaron radius and molar volume etc., were evaluated by using standard relation [18] and same were presented in table 2.

Figure 2 depicts the XRD spectra of ZnO-Sb_2O_3-B_2O_3: V_2O_5 glasses. The XRD pattern of sample V_2 shows no sharp peaks, which suggest that the sample clearly shows amorphous nature. A broad peak at nearly about 20-30° confirms the glassy nature of the

prepared samples [19]. All the other samples were also exhibit the similar behavior.

The variations of dielectric constant and dielectric loss of ZnO-Sb_2O_3-B_2O_3 glasses infused with different amounts of V_2O_5 with frequency at ambient temperature were presented in Figure 3 and 4.

For pure glass sample (ZnO-Sb_2O_3-B_2O_3), the value of dielectric constants was 6.47 and loss tangent was 0.005 at ambient temperature (30°C), at 100 kHz respectively. At a particular temperature, the dielectric constant and loss decreases with increasing frequency. At a particular temperature and frequency, the measured dielectric constant as well as tangent loss increases with increasing dopant concentration (inset of Figure 3 & Figure 4).

Table 2 – Physical parameters of ZnO-Sb_2O_3-B_2O_3: V_2O_5 glasses

Glass	Density d (g/cm³)	Avg.Mol. weight($\overline{M}$)	Conc.of V^{5+} ions N_i (10^{20}/cm³)	Inter ionic distance r_i (A°)	Polaron radius r_p (A°)	Molar Volume (cc/mol)
V_0	4.051	140.96	-	-	-	34.796
V_2	4.117	140.90	3.02	6.81	2.82	34.223
V_4	4.197	140.82	4.91	5.19	2.43	33.552
V_6	4.268	140.71	6.42	4.82	2.09	32.968
V_8	4.386	140.63	8.46	4.03	1.90	32.063
V_{10}	4.508	140.52	10.84	3.91	1.71	31.171
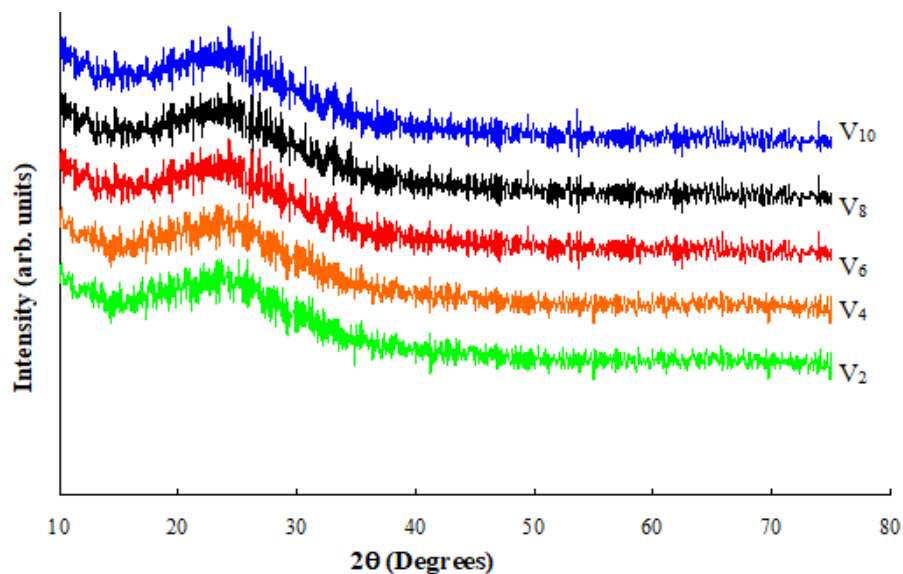
Figure 2 -XRD pattern of ZnO-Sb_2O_3-B_2O_3: V_2O_5 glasses
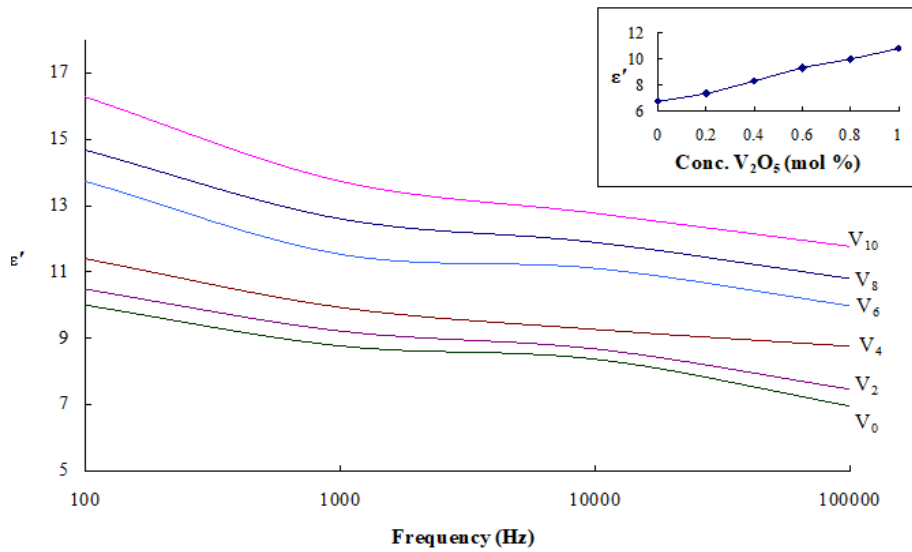
Figure 3-Variation of dielectric constant with frequency at room temperature of ZnO-Sb$_2$O$_3$-B$_2$O$_3$:V$_2$O$_5$ glasses. Inset represents the variation of ε' with the concentration of V$_2$O$_5$ at 100 kHz.
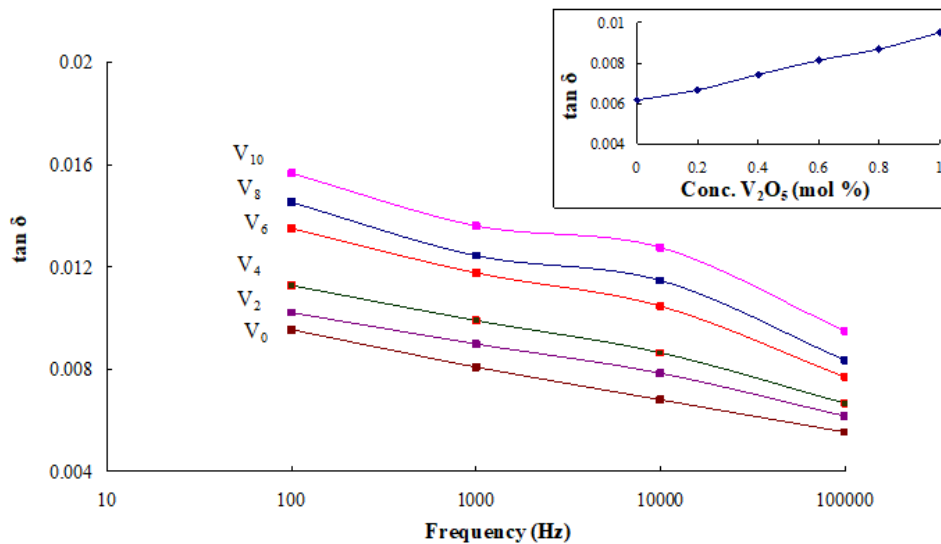
Figure 4 – Variation of dielectric loss with frequency at room temperature of ZnO-Sb$_2$O$_3$ -B$_2$O$_3$:V$_2$O$_5$ glasses. Inset represents the variation of tan δ with the concentration of V$_2$O$_5$ at 100 kHz

Figure 5 depicts the temperature sensitivity of dielectric constant at various frequencies for glass V$_{10}$. The value of dielectric constant is seen to grow along temperature, and this growth accelerates at low frequencies. The dependence of dielectric constant with temperature for other glasses also demonstrated the same trend.

A comparative plot of the temperature dependence at 1 kHz frequency for ZnO-Sb$_2$O$_3$-B$_2$O$_3$: V$_2$O$_5$ glasses were presented in Figure 6. The glass, doped with 1.0 mol% of V$_2$O$_5$ exhibits higher dielectric constant, maximum rate of growth of' dielectric constant with temperature.

Figure 7 displays a comparative plot of dielectric loss (tan δ) change with temperature for ZnO-Sb$_2$O$_3$-B$_2$O$_3$glasses infused with varying concentrations of V$_2$O$_5$ and recorded at 10 kHz.
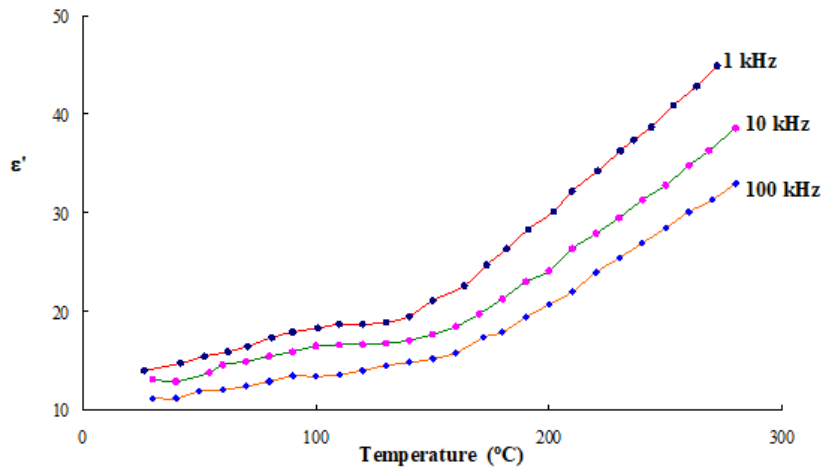
Figure 5 – Variation of dielectric constant with temperature at different frequencies of glass V_{10}
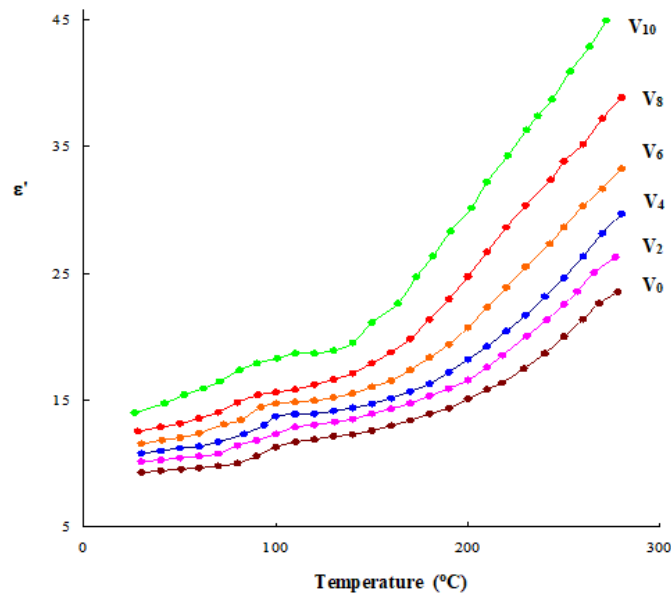
Figure 6- A comparison plot of variation of dielectric constant with temperature measured at 1 kHz for ZnO-Sb$_2$O$_3$ -B$_2$O$_3$: V$_2$O$_5$ glasses
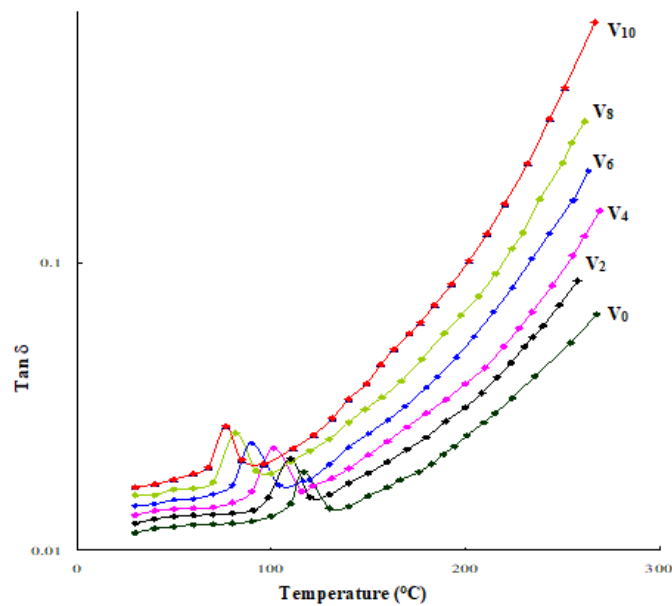
Figure 7- A comparison plot of variation of dielectric loss with temperature measured at
10 kHz for ZnO-Sb$_2$O$_3$-B$_2$O$_3$: V$_2$O$_5$ glasses

Discussion

Borate is well known glass former with possesses sp^2 planar BO$_3$ units and sp^3 tetrahedral BO$_4$ units. When Sb$_2$O$_3$, introduced in the borate glasses, Sb^{3+} ions exist as SbO$_3$ pyramids due covalent character of Sb-O bonds [20, 21]. In borate glass network, these SbO$_3$ units mainly act as a network former, through the formation of Sb-O-B bonds, BO$_3$ units are replaces the BO$_4$ units [22-25].

ZnO is, in general, a glass modifier and enters the glass network by breaking up the B-O-B, Sb-O-B linkages forms B-O-Zn [26]. However, ZnO may also acts as the glass network with ZnO$_4$ structural units [27]. Hence, ZnO-Sb$_2$O$_3$-B$_2$O$_3$:V$_2$O$_5$ glass community is an admixture of network formers, intermediate glass formers, and modifiers, however, the behavior of the ZnO and Sb$_2$O$_3$ strongly dependent on the composition of the glass samples.

With the addition of classic modifier oxide like V$_2$O$_5$ to the ZnO-Sb$_2$O$_3$-B$_2$O$_3$ glass community, the oxygens of such oxides typically, violate the local symmetry while cations occupies interstitial places by rupturing B-O-B, Sb-O-B and Zn-O-B links.

By comparing the pertained physical parameters data presented in Table 2, it has been observed that the density of glass increases from 4.051 to 4.508 g/cm^3 and molar volume decreases from 34.796 to 31.171 cc/mol.Such changes have been expected due to the replacement of heavy metal oxide Sb$_2$O$_3$ with

molecular weight 291.52 gm/mol by the V$_2$O$_5$ with molecular weight 181.88 gm/mol. The decrease in inter ionic distance; polaron radius and molar volume suggest that the ions in the samples becomes much closer with increasing the concentration of V$_2$O$_5$.

By recollecting the data of dielectric characteristics like dielectric constant and tangent loss of present studied ZnO-Sb$_2$O$_3$-B$_2$O$_3$: V$_2$O$_5$ glasses clearly point out, a slow increase of dielectric characteristics up to 1.0 mol% of V$_2$O$_5$ (Inset of figures 3 and 4). This behavior of the glasses can be understood as follows, the vanadium ions in the present glass network, are anticipated to primarily occur in V^{5+} state along with the V^{4+} state. However, there is a good chance that the following equilibrium could occur when the glasses melt at greater temperatures. These results anticipated the possibility of taking place redox equilibrium between the V^{5+} and V^{4+} state by following equation (1)

$$2\,V^{5+} + \; O^{2-} \; \rightleftharpoons 2V^{4+} + \tfrac{1}{2}O_2 \uparrow --- \qquad (1)$$
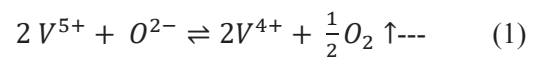
The V^{4+} ions create VO^{2+} complexes, which may function as modifiers and distort the network of glass, whereas the V^{5+} ions form locations with VO$_5$ trigonal bipyramidal structural units. Vanadium ions typically reside in the V^{4+} state and occupy modifying sites with rise of V$_2$O$_5$ up to 1.0 mol%. Such an increase ostensibly indicates a serious degree of disarray in the glass V$_{10}$ network, in another words,

[28, 29] the vanadium ions are becoming more prevalent and actively taking the part of modifications of network with V_2O_5.

It is well known that, the polarizability in an insulating material is due to the contribution of four types of polarizations viz., electronic, ionic, dipolar, and space charge polarisation. Among these first one is due to electric stain and rapid process, second one is due to displacements of ions from their equilibrium positons, slower than the first one, third one is due to alignment of dipoles towards the external electric field, takes more time than the first two, whereas last one is due to migration of ions towards the opposite polarity electrodes, slowest process among four. From Figure 3 and 4, the frequency dependency of dielectric constant and dielectric loss at a room temperature shows that higher value of ε' and tanδ at lower frequency strongly confirms the contribution of space charge polarization in the glass samples.

In ZnO-Sb$_2$O$_3$-B$_2$O$_3$ glass (base sample), the dielectric loss (Tanδ) varies with temperature at any frequency exhibits a distinct peak at about 100°c suggesting dipolar relaxation of dielectric loss in the samples. With the introduction of V_2O_5 in the glass matric, the intensity and half width of these relaxation peaks increases and shift towards lower temperature. Similar results observed with increasing the concentration of V_2O_5 in glass matrix. Traditionally, the dielectric relaxations are described at a stable temperature using a variable frequency. V^{4+} ions are responsible for the relaxation effects seen in the current glass samples.Vanadium ions may predominately present in V^{4+} sate get involved with glass altering positions as evidenced by expansion of breadth and depth of relaxation peaks and the lowering of activation energy in the samples from V_2 to V_{10}. Regarding different concentrations of V_2O_5, Using these graphs, the effective activation energy (W_d) for the dipoles is computed using relation (2)

$$f = f_0 e^{\left(-W_d/KT\right)} \text{ ---} \qquad (2)$$

Activation energy (W_d) for the dipoles is reported in Table 3 along with other significant information on dielectric loss. Glass V_{10} is reported to posses lowest activation energy, which supports the V^{4+} due to the VO^{2+} behaves as modifier in the glass network.

Table 3 – Data on dielectric loss and Activation energy of ZnO-Sb$_2$O$_3$ -B$_2$O$_3$: V_2O_5 glasses

Glass	Temp (ºC)	Dielectric loss			A.E for dipoles(eV)
		1kHz	10kHz	100kHz	
V_0	30	0.008	0.007	0.005	
	100	0.009	0.008	0.006	2.8
	250	0.045	0.030	0.027	
V_2	30	0.009	0.007	0.006	
	100	0.011	0.010	0.007	2.65
	250	0.050	0.035	0.030	
V_4	30	0.011	0.010	0.007	
	100	0.014	0.011	0.009	2.54
	250	0.080	0.045	0.040	
V_6	30	0.013	0.014	0.009	
	100	0.016	0.013	0.011	2.31
	250	0.095	0.080	0.069	
V_8	30	0.014	0.010	0.009	
	100	0.018	0.015	0.012	2.20
	250	0.139	0.124	0.110	
V_{10}	30	0.015	0.012	0.011	
	100	0.020	0.018	0.015	2.08
	250	0.247	0.228	0.210	

The ac conductivity σac is calculated at different temperature by using relation (3).

$$\sigma_{ac} = \omega\varepsilon_o\varepsilon tan\delta ---\qquad(3)$$

Where, ε_o is the vacuum dielectric constant at 100 kHz frequency. Figure 8 shows the variation of log σ$_{ac}$ against 1/T for glasses containing different concentration of V$_2$O$_5$ (measured at 100 kHz). The activation energy for conduction evaluates in the region of high temperatures (where it was possible to observe a nearly linear dependency of log σ$_{ac}$ with 1/T) based on these graphs and presented in Table 4; the activation energy is decrease linearly with conductivity; it is shown the lowest possible for the glass V$_{10}$ (inset (a) of Figure. 8).
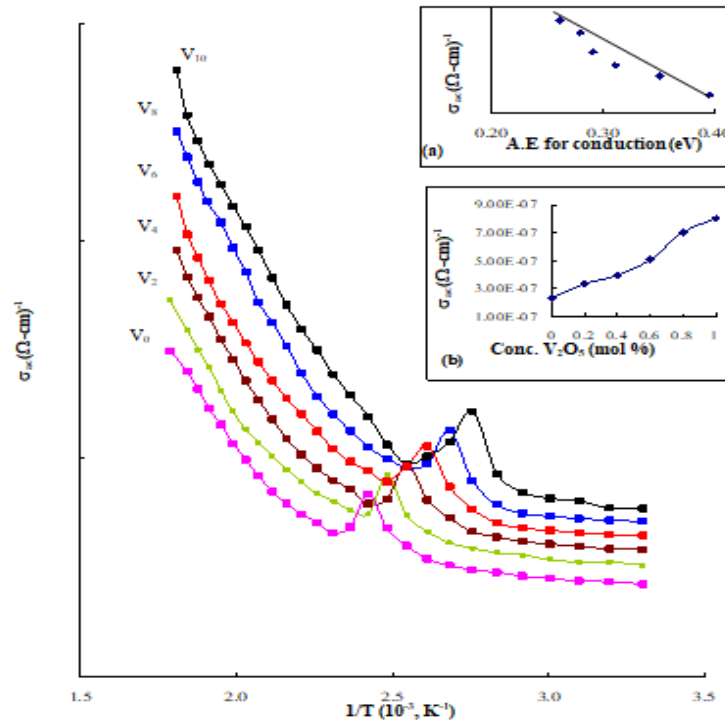
Figure 8 –Variation of ac conductivity with 1/T measured at 100 kHz for ZnO-Sb$_2$O$_3$-B$_2$O$_3$ glasses doped with different concentrations of V$_2$O$_5$. Inset a) represents variation of ac conductivity with activation energy, b) represents variation of ac conductivity with concentration of V$_2$O$_5$.

Table 4 – Summary of data on ac conductivity of ZnO-Sb$_2$O$_3$-B$_2$O$_3$: V$_2$O$_5$ glasses

Glass	N(E$_f$) in 10^{21} eV^{-1}/cm^3			AE for conduction (eV)
	Austin Butcher Pollack			
V$_0$	0.848	0.410	1.007	0.395
V$_2$	1.259	0.525	1.278	0.351
V$_4$	1.310	0.609	1.370	0.324
V$_6$	1.561	0.641	1.484	0.286
V$_8$	1.718	0.716	1.745	0.269
V$_{10}$	1.907	0.813	1.891	0.240

A connection that is almost linear is seen when log σ_{ac} is depicted on a graph as a function of the activation energy for conduction (Figure 8). This finding demonstrates increased conductivity is directly owing to charge carriers thermally enhanced mobility in the high temperature zone [30]. At x = 1.0 mol%, the conductivity curve with respect to V_2O_5 concentration reaches its maximum (Figure 8). The energy of activation for conduction showed a minimum at x = 1.0 mol% (inset of Fig. 8). These data point to a change in \

conductivity (from 0 to 1.0 mol% of V_2O_5) from largely electronic to primarily ionic [31].The ionic conductions active centers, the non-bridging oxygen molecules, the ion modifier contents, and the ionic transport all gradually increase. The low temperature component of conductivity, which is taking part in the progression of switching from $V^{5+} \Leftrightarrow V^{4+}$, can be interpreted using a quantum mechanical model [32]. It is discovered that the value of N (E_F) calculated by using standard equation (4)[33],

$$\sigma(\omega) = \lambda e^2 K_B T [N(E_F)]^2 (\alpha')^{-5} \omega \left(ln \left({v_{ph}}/{\omega} \right) \right)^4 \text{ --- (4)}$$

Where $\lambda = \pi/3$ for Austin, $\lambda = 3.66$ ($\pi^2/6$) for Butcher and $\lambda = \pi^4/96$ for Pollack, whereas the symbols N (E_F), σ, ω, e, K_B, v_{ph} ($\sim 0.5 \text{Å}^{-1}$), T having standard meanings. The value of N (E_F) rises with rising V_2O_5 concentration up to 1.0 mol%, such changes are in line with past claims that vanadium ions predominately occur in the V^{4+} state and serve as modifiers in the samples.

Conclusions

In conclusion, ZnO-Sb_2O_3-B_2O_3:V_2O_5 glasses were prepared by systematic replacement of Sb_2O_3 with V_2O_5 0.1 to 1.0 mol%. In relation to V_2O_5 concentration, various electric and dielectric properties were measured

and presented systematically. The perceived rise in dielectric constant (ε) and dielectric loss (tan δ) according to frequency and temperature, were explained contribution of space charge polarization in the glass sample and confirms the existence of equilibrium between $V^{5+} \Leftrightarrow V^{4+}$ ions in glass matrix. V^{4+} ions acts as a modifier in the glass samples. Among the studied glass samples, the glass with 1.0 mol% of V_2O_5 possess maximum ac conductivity, minimum activation energy for conductivity. Hence, V_{10} glass is better suited to accomplishing the desired electric conductivity in those glasses and these glasses have been used as electrode glass, optical amplifiers. This has been further confirmed with help of other studies like spectroscopic and non-linear optics.

References

1. Mott, Nevill Francis, and Edward A. Davis. *Electronic processes in non-crystalline materials*. Oxford university press, 2012.

2. Giuntini, J. C., D. Jullien, J. V. Zanchetta, F. Carmona, and P. Delhaes. "Electrical conductivity of low-temperature carbons as a function of frequency." *Journal of Non-Crystalline Solids* 30, no. 1 (1978): 87-98.

3. Elliott, S. R. "Defect pairing and the effect on AC conductivity in chalocogenide glasses." *Journal of Non-Crystalline Solids* 35 (1980): 855-858.

4. Doremus, R.H. Glass Science. NewYork: John Wiley & sons inc., 1994.

5. Kawamura, J., and M. Shimoji. "The AC conductivity of superionic conducting glasses $(AgI)_x-(Ag_4P_2O_7)_{1-x}$ (x= 0.8, 0.75, 0.7): Experiment and analysis based on the generalized Langevin equation." *Journal of non-crystalline solids* 79, no. 3 (1986): 367-381.

6. Dyre, Jeppe C. "A simple model of ac hopping conductivity in disordered solids." *Physics Letters A* 108, no. 9 (1985): 457-461.

7. Abelard, Pierre, and Jean François Baumard. "Dielectric relaxation in alkali silicate glasses: A new intepretation." *Solid state ionics* 14, no. 1 (1984): 61-65.

8. Ishii, Tadao. "Theory of classical hopping conduction: some general properties." *Progress of theoretical physics* 73, no. 5 (1985): 1084-1097.

9. Youngman, R. E., S. T. Haubrich, J. W. Zwanziger, M. T. Janicke, and B. F. Chmelka. "Short-and intermediate-range structural ordering in glassy boron oxide." *Science* 269, no. 5229 (1995): 1416-1420.

10. Youngman, R. E., and J. W. Zwanziger. "Multiple boron sites in borate glass detected with dynamic angle spinning nuclear magnetic resonance." *Journal of non-crystalline solids* 168, no. 3 (1994): 293-297.

11. Konijnendijk, Wo L., and J_M_ Stevels. "The structure of borate glasses studied by Raman scattering." *Journal of Non-Crystalline Solids* 18, no. 3 (1975): 307-331.

12. Marzouk, Samir Y., and Fatma H. Elbatal. "Infrared and UV–visible spectroscopic studies of gamma-irradiated Sb2O3–B2O3 glasses." *Journal of Molecular Structure* 1063 (2014): 328-335.

13. Holland, D., A. C. Hannon, M. E. Smith, C. E. Johnson, M. F. Thomas, and A. M. Beesley. «The role of Sb5+ in the structure of Sb2O3–B2O3 binary glasses—an NMR and Mössbauer spectroscopy study.» *Solid State Nuclear Magnetic Resonance* 26, no. 3-4 (2004): 172-179.

14. Imaoka, M., H. Hasegawa, and S. Shindo. "Properties and Structure of Glasses of B$_2$O$_3$–B$_2$O$_3$ System." *J. Ceram. Soc. Jpn.* 77, no. 8 (1969): 263-271.

15. Wood, Justin G., S. Prabakar, Karl T. Mueller, and Carlo G. Pantano. "The effects of antimony oxide on the structure of alkaline-earth alumino borosilicate glasses." *Journal of non-crystalline solids* 349 (2004): 276-284.

16. Soraya, M. M., Fatma BM Ahmed, and M. M. Mahasen. "Enhancing the physical, optical and shielding properties for ternary Sb$_2$O$_3$–B$_2$O$_3$–K$_2$O glasses." *Journal of Materials Science: Materials in Electronics* 33, no. 28 (2022): 22077-22091.

17. Narasimha Rao,N., Raghava Rao,P., Swamy, B.J.R.S.N., Chitti Babu, A., Sambasiva rao,T., Ramesh Babu, N.Ch.»The Influence of Vanadium Ions in Spectral Properties of ZnO–Sb$_2$O$_3$–B$_2$O$_3$ glasses."*International Journal for Modern Trends in Science and Technology.* 6 **(**2020): 201-207.

18. Naresh, P., SK Fakruddin Babavali, A. Chitti Babu, P. Raghava Rao, and N. Narasimha Rao. "Optical studies of chromium doped zinc oxy fluoro borate glasses–A possible disordered material for tunable LASERS." *Materials Today: Proceedings* 46 (2021): 806-810.

19. Rao, L. Srinivasa, V. Ravi Kumar, P. Naresh, P. Venkateswara Rao, and N. Veeraiah. «Optical absorption and photoluminescence properties of anadium ions in 'lithium-tungsten-borate'oxide glasses.» *Materials Today: Proceedings* 5, no. 13 (2018): 26290-26297.

20. Mochida, N., and K. Takahashi. «Properties and structure of glasses in the systems MO3/2. BO3/2 (M: As, Sb, Bi)." *J. Ceram. Soc. Jpn.* 84 (1976): 413-420.

21. Marzouk, Samir Y., and Fatma H, Elbatal. «Infrared and UV–visible spectroscopic studies of gamma-irradiated Sb$_2$O$_3$–B$_2$O$_3$ glasses." *Journal of Molecular Structure* 1063 (2014): 328-335.

22. Dubois, B., J. J. Videau, M. Couzi, and J. Portier. «Structural approach of the (xPbC$_{12}$–(1− x) Sb$_2$O$_3$) glass system." *Journal of non-crystalline solids* 88, no. 2-3 (1986): 355-365.

23. Miller, Philip J., and Charles A. Cody. «Infrared and Raman investigation of vitreous antimony trioxide.» *Spectrochimica Acta Part A: Molecular Spectroscopy* 38, no. 5 (1982): 555-559.

24. Raghavaiah, B. V., and N. Veeraiah. «The improved glass☐forming ability and some physical properties of PbO–Sb$_2$O$_3$: Cr$_2$O3 glasses with As$_2$O$_3$ as additive." *physica status solidi (a)* 199, no. 3 (2003): 389-402.

25. Raghavaiah, B. V., C. Laxmi Kanth, D. Krishna Rao, J. Lakshman Rao, and N. Veeraiah. "Optical and magnetic properties of PbO–Sb$_2$O$_3$–As$_2$O$_3$ glasses containing vanadium ions." *Materials Letters* 59, no. 5 (2005): 539-545.

26. Azooz, M. A., and H. A. ElBatal. «Preparation and characterization of invert ZnO–B$_2$O$_3$ glasses and its shielding behavior towards gamma irradiation." *Materials Chemistry and Physics.* 240 (2020): 122129.

27. Colak, S., Cetinkaya, I., Akyuz, and F. E. R. H. U. N. D. E. Atay. «On the dual role of ZnO in zinc-borate glasses.» *Journal of Non-Crystalline Solids.* 432 (2016): 406-412.

28. Abdelouhab, R. M., R. Braunstein, and K. Baerner. «Identification of tungstate complexes in lithium-tungstate-borate glasses by Raman spectroscopy.» *Journal of non-crystalline solids* 108, no. 1 (1989): 109-114.

29. Rao, L. Srinivasa, M. Srinivasa Reddy, D. Krishna Rao, and N. Veeraiah. «Influence of redox behavior of copper ions on dielectric and spectroscopic properties of Li2O–MoO3–B2O3: CuO glass system.» *Solid State Sciences* 11, no. 2 (2009): 578-587.

30. El-Damrawi, G. «PbCl$_2$ conducting glasses with mixed glass formers." *Journal of Physics: Condensed Matter* 7, no. 8 (1995): 1557.

31. Montani, R.A., Frechero, M.A." The conductive behavior of silver vanadium–molybdenum tellurite glasses."*Solid State Ionics.* 158(2003):327-332.

32. Austin, I. G., and N. Fr Mott. «Polarons in crystalline and non-crystalline materials.» *Advances in physics* 18, no. 71 (1969): 41-102.

33. Naresh, P., N. Narasimha Rao, P. Raghava Rao, B. J. R. S. N. Swamy, A. Chitti Babu, and B. Suresh. «Dielectric features of ZnO− CaF$_2$− R$_2$O (R= Li, Na & K)− B$_2$O$_3$: CuO glasses." *Materials Today: Proceedings* 92 (2023): 1563-1567.

Information about authors:

N. Narasimha Rao, Doctor of Philosophy in Physical Science, Assistant Professor in Physics, Krishna University Dr. MRAR College of PG Studies, Nuzvid-521 201, Andhra Pradesh, India.e-mail: nnrphy@gmail.com

P. Naresh, Doctor of Philosophy in Physical Science, Assistant Professor in Physics, Velagapudi Ramakrishna Siddhartha Engineering College, Vijayawada-520 007, Andhra Pradesh, India.e-mail: nareshp6@rediffmail.com

P. Raghava Rao, Doctor of Philosophy in Physical Science, Assistant Professor in Physics, Krishna University Dr. MRAR College of PG Studies, Nuzvid-521 201, Andhra Pradesh, India.e-mail: paritalaraghava@gmail.com

B.J.R.S.N. Swamy, Doctor of Philosophy in Physical Science, Assistant Professor in Physics, Krishna University Dr. MRAR College of PG Studies, Nuzvid-521 201, Andhra Pradesh, India.e-mail: jayram.bhogi@gmail.com

A. Chitti Babu, Doctor of Philosophy in Physical Science, Assistant Professor in Physics, Sir C. R. Reddy College of Engineering, Eluru – 534 007, Andhra Pradesh, India.e-mail: chittiphy@gmail.com

P. Sobhanachalam, Doctor of Philosophy in Physical Science, Assistant Professor in Physics, Krishna University, Machilipatnam-521 003, Andhra Pradesh, India.e-mail: sobhan.pamarthi@gmail.com

Contents